Calcium Imaging and Field Potential Analysis of Autocrine Neuromodulation in the Locus Coeruleus of Newborn Rat Brain Slices

by

Quinn Waselenchuk

A thesis submitted in partial fulfillment of the requirements for the degree of

Master of Science

Department of Physiology
University of Alberta

Abstract

The locus coeruleus (LC) is a small brainstem nucleus that controls diverse behaviours and brain functions via release of noradrenaline (NA) in the neonatal time period. There is increasing evidence of complexity in this neuron-astrocyte 'neural' network that remains mostly unexplored in neonates. Our group has established that in acutely isolated horizontal slices from newborn rat brains, the LC produces a local field potential (LFP) that can be recorded using suction electrodes, and that activity in individual neurons and astrocytes can be indirectly measured using cytosolic Ca^{2+} (Ca_i) imaging. The overall aim of this thesis was to perform experiments in vitro that exemplify the complexity of this network thus establishing a basis for future studies, particularly involving neuron-astrocyte interactions.

First, immunohistochemistry on chemically fixed slices found a unique distribution of LC neurons and astrocytes such that density of astrocyte somata was lower within the LC neuron soma area, whereas it was higher in the surroundings. A similar anatomical result was then found in acutely isolated living slices bulk loaded with the Ca^{2+} sensitive fluorescent dye Fluo-4. Next, combined Ca_i imaging and LFP recording during bath application of NA to mimic autocrine activity consolidated that NA depressed activity in neurons while it evoked an excitatory concentric Ca_i wave in astrocytes. Comparison with the effects of two other modulators, adenosine triphosphate (ATP) and trans-1-amino-1,3-dicarboxycyclopentane (t-ACPD), determined that ATP also evoked concentric astrocyte waves while t-ACPD did not. Additionally, different subpopulations of neurons and astrocytes responded to one of or a combination of these three modulators.

Together, this is the first study to show that astrocytes in any brain region propagate waves that travel in a concentric fashion and contributes to evidence of modular organization in the neonatal LC. This establishes that the neonatal LC neural network has a complex organization and highlights the possible role of neuron-astrocyte interactions, providing a foundation for future studies on neuronal and glial activity in this nucleus.

Preface

All procedures for experiments from our group were approved by the University of Alberta Animal Care and Use Committee (AUP-00000221) and in compliance with the guidelines of the Canadian Council for Animal Care and in accordance with the Society for Neuroscience's 'Policies on the Use of Animals and Humans in Neuroscience Research'.

Sections 1.1–1.3 and 1.5 of Chapter 1 have been published as: Waselenchuk Q, Ballanyi K (2022) Autocrine Neuromodulation and Network Activity Patterns in the Locus Coeruleus of Newborn Rat Slices. Brain Sci. 12:437.

Author contributions: conceptualization, Q.W. and K.B.; data analysis, Q.W.; writing, review, and editing, Q.W. and K.B. All authors have read and agreed to the published version of the manuscript.

Acknowledgements

Firstly, I would like to thank my supervisor Dr. Klaus Ballanyi. He introduced me to neuroscience research and provided invaluable guidance and encouragement during completion of this thesis. I would also like to give my express gratitude to Drs. Vladimir Rancic and Araya Ruangkittisakul for the countless hours they spent training me, answering my questions, and providing reassurance when I was certain I had broken a piece of equipment. I am also grateful to past members of our lab Dr. Bijal Rawal, whose previous experiments created the foundation for this project, and Tyson Keddie.

I am equally thankful for the support and direction offered to me by committee members, Drs. Jesse Jackson and Simon Gosgnach, and to Dr. Declan Ali for acting as my external examiner and taking the time to review this thesis.

To my friends and family, especially my parents, thank you for making this possible.

Table of Contents

List of Figures

Chapter 1:

Chapter 3:

List of Abbreviations

4^{th} V	4^{th} ventricle
5-HT	5-hydroxytryptamine (serotonin)
5-HTR	5-HT receptor
α_1R	α_1 adrenergic receptor
α_2R	α_2 adrenergic receptor
AMPA	α-amino-3-hydroxy-5-methyl-4-isoxazolepropionic acid
AMPAR	AMPA receptor
APV	Amino-5-phosphonopentanoic acid
ATP	Adenosine triphosphate
βR	β adrenergic receptor
Bic	Bicuculline
Ca_i	Free cytosolic Ca^{2+}
CNS	Central nervous system
CNQX	6-cyano-7-nitroquinoxaline-2,3-dione
DAMGO	[D-Ala2, N-Me-Phe4, Gly5-ol] Enkephalin
EC	Entorhinal cortex
EPSP	Excitatory post synaptic potential
FI	Fluorescence intensity
GABA	γ-aminobutyric acid
$GABA_AR$	A-type GABA receptor
GFAP	Glial fibrillary acid protein

GIRK	G protein-coupled inward-rectifying K^+ channels
GlyR	Glycine receptor
GPCR	G protein-coupled receptor
Hypocr	Hypocretin
iGluR	Ionotropic glutamate receptor
IP_3	Inositol triphosphate
IPSP	Inhibitory postsynaptic potential
KA	Kainate
KAR	KA receptor
LC	Locus coeruleus
LFP	Local field potential
μR	μ opioid receptor
Mus	Muscimol
NA	Noradrenaline
NMDA	N-methyl-D-aspartic acid
NMDAR	NMDA receptor
Orx	Orexin
OX1R	Orexin-1 receptor
P	Postnatal day
Phr	Phrenic nerve
PSP	Postsynaptic potential
ROI	Region of interest
STO	Subthreshold oscillation

Strych	Strychnine
t-ACPD	Trans-1-amino-1,3-dicarboxycyclopentane
TARP	Transmembrane AMPAR regulatory protein
TH	Tyrosine hydroxylase
Theo	Theophylline
t_{onset}	Time of response onset
TTX	Tetrodotoxin
V_m	Membrane potential

CHAPTER 1

General Introduction

1.1. Overview

The locus coeruleus (LC) in the dorsal pons is the source for actions of its main neurotransmitter noradrenaline (NA) on most structures in the central nervous system (CNS). Consequently, the LC controls multiple behaviors such as arousal, sleep–wake cycle, breathing, memory, pain sensation, anxiety, and opioid (withdrawal) effects via activity-related NA release (Foote et al., 1983; Berridge and Waterhouse, 2003; Schwarz and Luo, 2015; Magalhães et al., 2018; Poe et al., 2020).

1.1.1. Connectivity of the Adult LC

The complex connectivity in the adult LC as described in this section is summarized in **Fig. 1-1**. Regarding afferent inputs, e.g., the nucleus paragigantocellularis as well as the orbitofrontal and anterior cingulate cortices release glutamate onto LC neurons to activate all ionotropic glutamate receptor (iGluR) subtypes, i.e., receptors for α-amino-3-hydroxy-5- methyl-4-isoxazole propionic-acid (AMPAR), kainate (KAR), and N-methyl-D-aspartate (NMDAR). LC neurons also express postsynaptic receptors for neuropeptide transmitters, such as corticotropin-releasing factor or hypocretin/orexin, that are activated by inputs from the paraventricular nucleus and the posterior lateral hypothalamus, respectively. Moreover, serotonin receptors (5-HTR) are activated on LC neurons by inputs from the Raphe nuclei whereas they are inhibited by ventrolateral preoptic area neurons that release γ-aminobutyric acid (GABA) to act on $GABA_A$ receptors ($GABA_AR$). Importantly, interneurons within the LC can also release GABA to activate $GABA_AR$ on neighboring cells and local release of opioids or NA (from proximal LC neuron collaterals) has further modulating effects on LC activity (Nakamura and Sakaguchi, 1990; Benarroch, 2009; Delaville et al., 2011). While opioid actions are presumably inhibitory, NA can either activate typically inhibitory α_2 (auto)receptors (α_2R) or excitatory α_1 (auto)receptors (α_1R) on LC neurons

and, the latter, also on neighboring astrocytes. LC astrocytes likely also express other neurotransmitter and neuromodulator receptors which mediate neuron-glia ('neural') network interactions that support behaviors such as sleep, attention, or breathing (Halassa and Haydon, 2010; Teschemacher and Kasparov, 2017). The latter examples indicate that the LC neural network is under extensive autocrine neuromodulatory control.

In response to the concerted activities from afferent structures, LC neurons discharge Na^+ action potential 'spikes' that promote release of NA at axon varicosities in the target areas plus presumably a co-transmitter such as the neuropeptides galanin and neuropeptide-Y (Schwarz and Luo, 2015). This LC activity modulates the patterns of often spontaneous activities in the target circuits like different cortical areas, the thalamus, or the cerebellum. Moreover, activities in these circuits can change during various brain states such as sleep or wakefulness, pain sensation, or attention, already without input from the LC. Altogether this means that the LC serves as an interface. On the one hand, it receives complex patterns of synaptic inputs from various sources to cause release of different types of neurotransmitters acting on several receptor subtypes. On the other hand, this evokes LC neuron discharge and/or alters their spontaneous spiking to subsequently modulate the activity in target circuits as well as within the LC for autocrine neuromodulation.

1.1.2. Modular Organization of Adult LC

It is not known how the small and compact LC, consisting in each of its bilaterally-organized aspects of only ~1600 neurons in rats **(Fig. 1-2)** and ~20,000 in humans (Loughlin et al., 1986; Christie, 1997; Schwarz and Luo, 2015), can control many different brain activities and behaviors.

A recent review of this topic (Totah et al., 2019) stated that it was thought until recently that the evolutionarily ancient LC sends a rhythmic and global NA pulse to the neuraxis, similar to rhythmic systemic blood distribution by the heart. Accordingly, LC neurons and heart myocytes would share electrophysiological membrane properties like gap junction-mediated electrical coupling or intrinsic 'pacemaker'-like ion conductances mediating spontaneous spiking to generate coordinated activity for pulsed NA release and blood supply, respectively. The authors then point out that in the past decade evidence has steadily increased that the LC contains anatomically and functionally distinct modules. As examples from various studies (Schwarz and Luo, 2015; Jin et al., 2016; Li et al., 2016; Uematsu et al., 2017; Totah et al., 2018; Chandler et al., 2019; Poe et al., 2020), LC neurons show a topographical organization regarding: (*i*) morphology that shows a preferentially 'multipolar' shape of the soma and primary dendrites in the ventral LC aspect contrary to location of simpler 'fusiform' shaped neurons in the dorsal part, (*ii*) release of a distinct co-neurotransmitter such as neuropeptide-Y or galanin in addition to NA, (*iii*) expression of neurotransmitter receptors such as α_1R or α_2R, (*iv*) axonal projection areas as neurons innervating the hippocampus are preferentially located in the anterodorsal LC region and those projecting to the cerebellum in the ventral aspect, (*v*) electrophysiological properties as neurons innervating distinct cortical areas differ in their firing rate and spike after-hyperpolarization amplitude. There is also evidence for a pontospinal projecting module that is comprised of ventrally located LC neurons with a shorter spike and smaller spike after-hyperpolarization compared to the LC core whereas faster spiking with enhanced adaptation is seen in dorsomedially-located small GABAergic neurons. In addition to such modular organization of the LC, its network activity is complex rather than occurring mainly in pulsed fashion. Specifically, there is evidence for an 'ensemble code' in the LC and spiking does not

occur as a synchronous population event. Instead, LC neurons are capable of producing different outputs with varying extent of synchrony between them which may be correlated to behavioral states such as vigilance. Altogether, these considerations point out that the adult LC is a complex network with a modular organization needed for its diverse control functions.

1.1.3. Current Knowledge of Neonatal LC Network Properties

In rats, axons of LC neurons project to diverse target areas already at 12–14 days of gestation (Olson and Seiger, 1972; Lauder and Bloom, 1974). This implies that the neonatal LC is functional and plays an important role in controlling development of other brain networks in the perinatal time period (Kimura and Nakamura, 1985; Nakamura and Sakaguchi, 1990; Marshall et al., 1991; Oyamada et al., 1998; Patel and Joshi, 2015). Due to its small size there is very sparse information on electrophysiological and pharmacological LC properties in intact newborn animals (Nakamura et al., 1987; Sakaguchi and Nakamura, 1987; Nakamura and Sakaguchi, 1990). Consequently, such knowledge is primarily based on findings from in vitro models. Studies on newborn rat brain slices have established that, at this age, the LC comprises a 'simple' spontaneously active neural network that serves as a model for spike synchronization (Christie, 1997; Patel and Joshi, 2015). Specifically, neonatal LC neurons are electrically coupled via gap junctions and generate, via an endogenous pacemaker mechanism, synchronized Ca^{2+}-dependent subthreshold oscillations (STOs) of their membrane potential (V_m) at a rate of ~1 Hz that lead to discharge of typically a single Na^+ spike at their peak (Williams et al., 1984; Williams and Marshall, 1987; Christie et al., 1989; Marshall et al., 1991; Christi and Jelinek, 1993) **(Fig. 1-3)**. During the first 2–3 postnatal weeks, the rate of such tonic spiking increases slightly (to ~3 Hz) and the extent of synchronization appears to weaken progressively (Marshall et al., 1991; Alvarez et al., 2002; Patel and Joshi, 2015).

The latter studies proposed that decreased spike synchronization is the consequence of diminished gap junction expression.

While the aforementioned findings were obtained using neonatal rat slices, many other LC neuron properties were analyzed in slices from either juvenile or adult rodents. For example, to study afferent inputs, V_m recording from a single neuron was combined with electrical stimulation of neighboring slice areas (Williams et al., 1991). This showed that LC neurons express different types of ion channels mediating a postsynaptic potential (PSP), specifically (*i*) iGluR cation channels causing an excitatory postsynaptic potential (EPSP), (*ii*) anion channels associated with a $GABA_AR$ or glycine receptor (GlyR) mediating an inhibitory postsynaptic potential (IPSP), and also (*iii*) slow (post-activation) IPSPs caused by G protein receptor-coupled K^+ ('GIRK') channels associated with α_2(auto)R that are activated by local release of NA from neighboring LC neurons for autocrine modulation.

In brain slices, it is not clear from which areas in the neuraxis stimulated axons originate. In contrast, using a newborn rat brainstem-spinal cord model it was shown that the LC receives rhythmic inputs from brainstem respiratory networks (Oyamada et al., 1998) **(Fig. 1-2)**. Specifically, >50% of recorded tonically active LC neurons show an inspiratory-related burst of iGluR-mediated EPSPs which accelerates their spiking. This excitation is followed by an α_2R-mediated hyperpolarization during which spiking is blocked. This report also showed that these LC neurons are chemosensitive as their spike rate increases in solution with a lower pH. It is possible that this chemosensitivity is fed back synaptically into the inspiratory network to adapt its activity to a change in pH in the brainstem (Magalhães et al., 2018). Finally, they identified in

that study 'type-1' and 'type-2' LC neurons that differ in STO regularity and amplitude **(Fig. 1-2)**. In summary, this work indicated that the neonatal LC is already a complex network with functionally different neuron types. Note that an interaction of the LC and respiratory neural circuits is also seen in adults as shown in an article of this Special Issue (Melnychuk et al., 2021).

1.1.4. Aim of Present Study

In this 'Perspective' article, we present further evidence for a complex (possibly even modular) organization of the neonatal LC based on our recent findings in acutely isolated horizontal slices from newborn rats. Specifically, our experiments were done on horizontal brain slices from 0–7 day-old CD-001 (Sprague-Dawley) rats of either sex (Charles River Laboratory Inc., Wilmington, MA, USA). Slices were generated using the procedures described previously (Kantor et al., 2012; Rancic et al., 2018; Rawal et al., 2019). The success rate of generating a slice that could be used for recording was >95%. In almost all cases one finding was obtained from one recording in one slice per rat.

Contrary to more challenging in vivo studies, cells in such slices can be visualized while combining extracellular and intracellular electrophysiological recording and live cell imaging, e.g., of changes in their free cytosolic Ca^{2+} concentration (Ca_i), during quantitative pharmacological analyses. In this regard, we were the first to demonstrate that the LC generates a local field potential (LFP) in these slices (Kantor et al., 2012) **(Fig. 1-2)** (note that this LFP can principally also be termed 'multi-unit activity' (Poil et al., 2011; Buzsáki et al., 2012)). In this report, we show that the same slices also contain networks in the entorhinal cortex and hippocampus which generate rhythmic LFPs different from that in the LC regarding both their rates and mechanisms (see also Garaschuk

et al., 2000) **(Fig. 1-2)**. In a more recent study (Rancic et al., 2018), we combined LFP recording of LC neuron population activity with single neuron recording to show that their spiking is not synchronous and is, instead, 'phase-locked' to the LFP. In a third study (Rawal et al., 2019), we used LFP plus whole-cell patch-clamp V_m recording as well as multiphoton Ca_i imaging in populations of LC neurons and neighboring astrocytes during LFP acceleration evoked by activation of AMPARs forming a complex with supplementary proteins. Here, we put these results in context with our current findings based on consistent effects in at least five experiments. In summary, our study indicates that the neonatal LC shares various cellular and pharmacological properties and has a similarly complex (possibly modular) organization, as in adults. In the discussion, we show perspectives for future directions of research on autocrine neuromodulation in the neonatal and adult LC.

1.2. Preliminary Results

We firstly deal with intrinsic properties of the LC network and then state a lack of necessity of iGluR-mediated excitation and receptor-coupled anion channel-mediated inhibition for generation of LFP rhythm. We then show that iGluR agonists accelerate neuronal spiking and transform the LFP pattern. Next, we demonstrate that high doses of the μ opioid receptor (μR) agonists morphine and [D-Ala^2, *N*-MePhe^4, Gly-ol]-enkephalin (DAMGO) and the α_2R agonist clonidine abolish rhythm, whereas low doses of these agents slow it with occurrence of an often crescendo-like multipeak LFP pattern. This is followed by pointing out different NA effects on LC neurons and astrocytes as revealed by population Ca_i imaging. It is also noted under which conditions rhythmic activities and different types of LC neurons can be detected with population Ca_i imaging. Finally, we refer to a neuron–astrocyte interaction involving lactate as a gliotransmitter.

1.2.1 Anatomical and Intrinsic LC Properties

Neonatal rat LC neurons have a rather uniform round to fusiform shape with a soma diameter of 20–30 µm from which 2–5 processes originate in a confocal plane **(Fig. 1-3)**. These neurons are intermingled with fewer astrocytes with a soma diameter of ~10 µm whereas similarly sized astrocytes surrounding the LC form a more dense network **(Fig. 1-3)**. The largest diameter of the spindle-shaped neonatal rat LC in the horizontal plane is ~300 µm and it extends in the dorsoventral plane by ~1000 µm (Ishimatsu and Williams, 1996; Ballantyne et al., 2004; Kantor et al., 2012; Rawal et al., 2019). We found in 400 µm thick acutely isolated horizontal slices that positioning of a suction electrode with an outer tip diameter of 40–60 µm at slice surface within the LC reveals a rhythmic LFP at a rate of ~1 Hz that is due to summation of mostly single spikes in 3–10 neurons located close to the electrode (Rancic et al., 2018). The LFP has a similar shape and amplitude when the electrode is positioned either in the center or more peripheral LC areas indicating that it is quite uniform within the nucleus. At a distance greater than ~50 µm outside the LC neuron somata area, no robust LFP is detectable. Moreover, the LFPs of the ipsilateral and contralateral LC aspects do not show a temporal correlation. The LFP signal generally has a very good signal-to-noise ratio and is stable for up to 24 h, therefore making it well suited for complex functional and pharmacological analyses of neonatal LC network properties. The duration of a single, mostly bell-shaped, burst (lasting ~0.3 s) is particularly evident in the 'integrated' form of the signal. This duration already indicates that the LFP does not represent the summation of synchronous Na^+ spikes that span 1–3 ms in (neonatal) LC neurons (Williams and Marshall, 1987; Sanchez-Padilla et al., 2014; Matschke et al., 2015, 2018) **(Figs. 1-3,1-4)**. By combining LFP recording with patch electrode recording of single neuron spiking, we showed that each cell discharges (with a jitter of 20–100 ms) preferentially at a particular time point of the population

burst (Rancic et al., 2018) **(Fig. 1-3)**. We concluded in that study that neonatal LC neuron discharge is not synchronous, but rather 'phase-locked' to the network response.

Regarding other intrinsic LC network properties, we demonstrated that the LFP is reversibly abolished by the voltage-gated Na^+ channel blocker tetrodotoxin (TTX), indicating that it reflects neuronal spiking rather than STOs (Rancic et al., 2018). However, we found that TTX also abolishes STOs in most LC neurons (Rawal et al., 2019). The presence of the 'persistent' subtype of Na^+ channels (mediating neuronal bursting) in the newborn rat LC is indicated by our finding in slices that the blocker riluzole abolishes the LFP (Kantor et al., 2012) **(Fig. 1-3)**.

With respect to the connectivity of neonatal LC neurons, it has been proposed that STOs and associated spiking are synchronous due to their electrical coupling by gap junctions comprising connexin-26, -32, and -43 subunits (Ishimatsu and Williams, 1996; Christie, 1997; Alvarez-Maubecin et al., 2000) **(Fig. 1-3)**. Another study instead proposed that neuronal coupling occurs only via connexin-36 (Rash et al., 2007). Accordingly, 100 µM of the gap junction inhibitor carbenoxolone abolished STOs and associated rhythmic hyperpolarizations in LC astrocytes (Alvarez-Maubecin et al., 2000; Alvarez et al., 2002) while we found that the connexin-32 blocker mefloquine also blocks LFP rhythm (Rancic et al., 2018) **(Fig. 1-3)**. In our hands, carbenoxolone application for ≥5 min only transiently perturbs LFP rhythm at 100 µM or more while mefloquine also depresses neuronal properties. It thus appears that more selective gap junction blockers are needed to identify the specific functional role of gap junctions in the neonatal LC.

We also found that LC neurons differ regarding other intrinsic conductances not involving neurotransmitter actions (Waselenchuk et al., 2022). Specifically, three distinct spike patterns are seen in response to changing their 'holding' V_m via injection of constant current through the patch electrode from their 'resting' V_m ranging from −35 to −55 mV (Williams and Marshall, 1987; Oyamada et al., 1998; Rawal et al., 2019) **(Figs. 1-2,1-4–1-7)**. As exemplified in **Fig. 1-4**, 52% of 29 recorded neurons respond to such depolarization with a steady increase of the rate of their very regular spiking. Another 28% of LC neurons discharge spike trains ('bursts') in response to depolarizing their V_m, and with increasing sustained depolarization by up to 25 mV, these trains consist of 2 to 15 spikes/s that are interrupted by progressively shorter silent periods of ~1 to 0.1 s. The remaining 21% of cells respond to depolarization with modestly accelerated spiking which is quite irregular, a feature also seen often at resting V_m.

As will be partly dealt with in more detail below, LFP rhythm is not substantially depressed in slices with robust rhythm by blockers of neurochemical synaptic processes involving AMPAR, KAR, NMDAR, $GABA_AR$, GlyR, μR, (auto) α_1R, α_2R, or β NA receptors (βR). It can be concluded that these receptors are not required for generating this network rhythm.

1.2.2. Role of iGluR in Neonatal LC Rhythm

Various neural network rhythms in newborn and adult mammals depend on iGluR (for references, see **1.3**). For example, it was mentioned above that horizontal newborn rat brain slices contain spontaneously active networks in the hippocampus and entorhinal cortex in addition to that in the LC **(Fig. 1-2)**. The 'classical' AMPAR antagonist 6-cyano-7-nitroquinoxaline-2,3-dione (CNQX) (Traynelis et al., 2010) is sufficient to abolish the 'early network oscillations' in the entorhinal

cortex (Garaschuk et al., 2000) whereas combined blockade of both AMPAR and NMDAR is needed to abolish the hippocampal oscillations (Sipilä and Kaila, 2008). In the LC of such slices, we found firstly that the unselective non-competitive iGluR blocker kynurenic acid has no effect on LFP rhythm (Rawal et al., 2019). However, in the same study 25 µM CNQX accelerated LFP bursting in association with a <10 mV neuronal depolarization and a modest rise in neuronal Ca_i (see below). All effects were reversed by 25 µM of the non-competitive AMPAR blocker GYKI-53655. We concluded from these findings that in neonatal LC neurons AMPAR form a functional complex with transmembrane AMPAR regulatory proteins (TARP) on which CNQX acts as a partial agonist (Traynelis et al., 2010; Jackson and Nicoll, 2011; Greger et al., 2017; Maher et al., 2017). The latter findings and the effects of iGluR agonists described in the following are summarized in **Fig. 1-5**.

While generation of LC network rhythm does not depend on iGluR, AMPAR, KAR and NMDAR, agonists at these receptors have pronounced effects on LFP pattern (Rawal and Ballanyi, 2022; Rawal et al., 2022). Specifically, moderate doses of these iGluR agonists accelerate LFP rhythm from ~1 Hz to ~5 Hz. The faster LFP oscillations during AMPA and KA occur frequently without recovery of the (integrated) signal to baseline while showing a spindle-shaped waxing and waning of amplitude. At concentrations of 0.25–0.5 µM AMPA and 2.5 µM KA, these oscillations are very stable and similar to each other. During the LFP oscillations, V_m depolarizes by ~5 mV and spike rate increases by the same rate as LFP rhythm. While kynurenic acid blocks both types of LFP oscillations, GYKI-53655 selectively blocks the responses to AMPA whereas KA-evoked oscillations are selectively abolished by 25 µM UBP-302. NMDA evokes similar fast LFP oscillations at 25–50 µM that are selectively blocked by (2R)-amino-5-phosphonovaleric acid

(APV). The oscillations are interrupted during sustained NMDA application after 1–5 min by a 1–2 s-lasting blockade of rhythm resulting in 'oscillation trains'. In single LC neurons, the time courses of crescendo-shaped rhythmic sustained V_m depolarizations, intermittent hyperpolarizations, and spiking are closely related to the oscillation train LFP pattern **(Fig. 1-5)**.

The acceleration of rhythm by CNQX and all iGluR agonists is accompanied by a shortening of single burst duration, e.g., for CNQX by 26% (Rawal et al., 2019). This shortening indicates that the extent of spike synchronization is increased by the agonists. In the case of CNQX, though, cross-correlation analysis of the LFP peak with spiking in single neurons did not verify this assumption while we did find that the regularity of rhythm increased (Rawal et al., 2019). In contrast, NMDA increases the extent of synchronization while AMPA and KA show a trend in that respect. Regardless, all agonists increase the regularity of rhythm.

1.2.3. Role of Inhibition on Neonatal LC Rhythm

Ongoing synaptic inhibition via $GABA_AR$ or GlyR is needed for several types of brain rhythms in adults and newborns (for references, see **1.3.**). In contrast, neonatal LC network rhythm is not affected by blockade of $GABA_AR$ or GlyR as exemplified in **Fig. 1-6**, which also demonstrates that LFP rhythm is abolished by activation of these receptors with muscimol and Gly, respectively (Panaitescu and Ballanyi, 2022). Additionally, this figure shows for muscimol that these receptors mediate a pronounced hyperpolarization and conductance increase. The V_m recording also demonstrates that low millimolar theophylline blocks the $GABA_AR$ (Ruangkittisakul and Ballanyi, 2010) in the presence of muscimol, leading to both reversal of the hyperpolarization plus conductance increase and recovery of rhythm (Panaitescu and Ballanyi, 2022).

Moreover, we reported that opioids depress network rhythm (Rancic et al., 2018). Specifically, the μR agonist DAMGO abolishes the LFP and longer-lasting crescendo-like multipeak events occur early during recovery **(Fig. 1-7)** similar to recovery from α_2R-mediated inhibition **(Fig. 1-8)**. We studied the latter effects in more detail as dealt with in the next sections.

1.2.4. μR- and α_2(Auto)R-Mediated LFP Pattern Transformations

Our finding that the LFP burst pattern transforms early during recovery from micromolar DAMGO (Rancic et al., 2018) **(Fig. 1-7)** indicates that such activity is due to an effect of a time period of lower doses occurring in the LC during washout. Indeed, 50–150 nM of either DAMGO or the natural μR agonist morphine typically slow LFP rhythm and evoke the often crescendo-like multipeak LFP burst pattern throughout application periods of several minutes (Panaitescu and Ballanyi, 2022) **(Fig. 1-7)**. As one explanation, μR activation may increase the delay between the phase-locked discharge of single spikes. In line with this possibility, LFP amplitude is mostly reduced by DAMGO. As a different or additional mechanism, burster neurons **(Fig. 1-4)** might discharge spike bursts during this phase. Bursting can principally occur during recovery of the neonatal LC from opioids as exemplified in **Fig. 1-7**. Here, DAMGO-evoked hyperpolarization was reversed by theophylline, which also antagonizes the response to $GABA_AR$ or GlyR activation (Panaitescu and Ballanyi, 2022) **(Fig. 1-6)**. For muscimol or glycine, recovery of rhythm during washout (or reactivation by theophylline) does not show a phase of multipeak bursting, in contrast to the effect of opioids, despite similar hyperpolarizations. Systemic administration of the μR agonist remifentanil for anesthesia can evoke similarly slow persistent bursting in the LC of rats in vivo (Ballanyi and Eschenko, 2022). Moreover, intracerebroventricular morphine injection in adult rats evokes even slower neuronal bursts that are reversed by kynurenic acid injection into the

LC, which indicates that iGluRs are necessary for this phenomenon (Zhu and Zhou, 2005) **(Fig. 1-8)**. α_2R activation can also induce spike bursts, an effect observed when interstitial NA levels in the LC of juvenile/adult rat slices were increased by blocking its reuptake with cocaine after spontaneous release. Consequently, cocaine slowed and augmented the amplitude of STOs and transformed single spike discharge into slower discharge of multiple spikes **(Fig. 1-8)** and these effects were reversed by α_2R blockade (Williams and Marshall, 1987). In agreement, our findings show that LFP bursts are slowed and prolonged during application of 100–250 nM clonidine. Higher clonidine doses block LFP rhythm and (crescendo-like) multipeak bursts occur transiently again during washout **(Fig. 1-8)**. Accordingly, the effects of μR and α_2R activation on LC rhythm are very similar in the isolated neonatal rat LC.

1.2.5. Ca_i Changes in LC Neurons and Astrocytes

Our results above are based on LFP recording combined with monitoring of either cell-attached single neuron spiking or V_m. The following findings additionally involved population Ca_i imaging of LC neurons and astrocytes. For this, cells are stained with the membrane-permeant chemical Ca^{2+} dye Fluo-4 via pressure injection from a broken patch electrode into the LC center at a depth of ~50 μm into the slice (Ruangkittisakul et al., 2009; Carrillo-Reid et al., 2017; Pires et al., 2021).

In our study on the functional TARP-AMPAR complex (Rawal et al., 2019), the partial agonist CNQX evokes a modest and uniform Ca_i rise in neurons with no effect on astrocytes. However, spontaneous Ca_i rises occur randomly in a subpopulation of ~20% of astrocytes. This is shown in **Fig. 1-9** which also exemplifies that the CNQX-evoked neuronal Ca_i rise persists in TTX which lowers Ca_i baseline. In contrast, we found that 25 μM NA causes a steady decrease of neuronal Ca_i

baseline which recovers within <3 min upon start of washout. An opposing effect is seen in astrocytes during NA where Ca_i increases in a novel type of 'concentric' Ca^{2+} wave. Essentially, Ca_i increases firstly in astrocytes located >100 µm distant to the LC, then in astrocytes located closer to the LC soma area, and finally in astrocytes within the nucleus (Waselenchuk et al., 2022) **(Fig. 1-9, video)**. The NA-evoked concentric Ca^{2+} wave is blocked by the specific α_1R antagonist prazosin whereas the neuronal fall of Ca_i is blocked by the specific α_2R antagonist yohimbine. Both neurons and astrocytes seem to possess metabotropic glutamate receptors and purinergic receptors because the respective agonists trans 1-Amino-1,3-dicarboxycyclopentane (t-ACPD) and adenosine triphosphate (ATP) cause a notable Ca_i rise in astrocytes (mostly also in a concentric wave for ATP, but not t-ACPD) whereas neuronal responses are smaller (Waselenchuk et al., 2022) **(Fig. 1-9)**. The neuronal Ca_i changes are apparently modest as application of 0.5 or 1 mM glutamate at the end of an experiment causes a >5-fold larger increase in Fluo-4 fluorescence. As a further observation, the number of astrocytes seems to be smaller within the nucleus compared to surrounding slice areas (Rawal et al., 2019) **(Fig. 1-3)**.

With population imaging, covering the LC and portions of surrounding tissue, we did not detect LFP-related neuronal Ca_i increases in control, contrary to spike-related (dendritic) Ca_i rises seen in adult mouse slices using fast line-scanning imaging (Sanchez-Padilla et al., 2014) **(Fig. 1-10)**. However, we detect rhythmic Ca_i rises in solution with 7 or 9 mM K^+ when the LFP transforms to slower pronounced multipeak bursts as we have reported previously (Rancic et al., 2018) **(Fig. 1-10)**.

For our above findings, we used a bath-application approach to apply neuromodulator agonists and antagonists. While this partly mimics global autocrine modulation of the LC network, it is not clear how cells respond to activation of afferent inputs. It was mentioned above that single electrical stimuli of areas surrounding the LC evoke an EPSP-IPSP sequence (Williams et al., 1991). We were unable to detect changes in neuronal Ca_i in response to a single stimulus, contrary to occurrence of robust signals in response to repetitive stimulation involving >10 single pulses at a rate of 20–100 Hz (Waselenchuk et al., 2022). Such 'tetanic' stimulation causes only a rise of Ca_i in ~60% of neurons whereas in the remaining cells the initial Ca_i increase is followed by an 'undershoot' below its baseline **(Fig. 1-10)**. A major portion of the stimulus-evoked Ca_i rise is attenuated by CNQX and the remaining by prazosin (Waselenchuk et al., 2022) **(Fig. 1-10)**.

The last aspect of the present study deals with a novel neuron-astrocyte interaction that has been detected in cultured LC slices from newborn rats (Tang et al., 2014). Using a combined optogenetic/Ca_i imaging and electrophysiological approach, the authors demonstrated a new role of the metabolite L-lactate in neuron-glia communication. Specifically, depolarization of LC astrocytes causes them to release L-lactate, which then diffuses to neighboring neurons to evoke a depolarization that initiates their spiking via a yet unknown receptor **(Fig. 1-1)**. We also find that in acutely isolated newborn rat slices, L-lactate acts excitatory to accelerate LFP rhythm likely in response to α_1R-activated vesicular Ca_i rise in astrocytes.

1.3. Discussion

By combining electrophysiological recording with population Ca_i imaging, we present here evidence for novel neonatal LC properties. We demonstrate that the newborn rat LC forms a neural

network that is capable of generating a LFP. In the following sections we summarize the properties of this LFP and refer them, on the one hand, to those detected in single neurons based mainly on in vitro studies in newborn, young, and adult rodents. On the other hand, we compare neonatal LC network properties to those in the adult mammalian LC showing a modular organization.

1.3.1. Intrinsic Neonatal LC Properties

LFP recording in vivo and in brain slices was, and still is, instrumental for unraveling neural network properties in a variety of brain regions, with the largest number of studies on the cortex, including hippocampus (Jefferys, 1994; Bartos et al., 2007; Poil et al., 2011; Buzsáki et al., 2012; Gonzalez et al., 2012; Einevoll et al., 2013; Pires et al., 2021; Avramiea et al., 2022). For the LC, no LFP has been reported in slices until our first study did so (Kantor et al., 2012). In that study and our follow-up work (Rancic et al., 2018), we showed that recording the LFP depends on using ~50 µm large suction electrodes instead of often used fine-tipped (patch) or metal electrodes. Suction electrodes are typically applied for in vitro nerve root recording, mostly in models of the neonatal rodent locomotor or respiratory networks (Funk et al., 1993; Bracci et al., 1996; Ballanyi and Ruangkittisakul, 2009). The group of Ramirez also possibly found out that they can be used to monitor the LFP generated by rhythmogenic inspiratory center neurons from the surface of the corresponding ventrolateral area in 'breathing slices' (Lieske et al., 2000; Ballanyi and Ruangkittisakul, 2009).

LFP shape and amplitude do not appear to differ between recording sites within the neonatal LC. This indicates that there are no local neuron modules that may discharge under control conditions in a fashion basically different from that of the main LC network ensemble as seen in the inferior

olive of slices from young and adult rats (Devor and Yarom, 2002) and LC (Chandler et al., 2014; Li et al., 2016). Our finding of a blocking effect of TTX on both the LFP and STOs is similar to observations in the en bloc model (Oyamada et al., 1998) and adult mouse slices (Sanchez-Padilla et al., 2014), whereas TTX had mostly no effect on STOs in other LC slice studies (Williams and Marshall, 1987; Christie et al., 1989; Alvarez et al., 2002).

The LC-LFP comprises spike discharge of 3–10 LC neurons with no synaptic component, contrary to that in the hippocampus (Jefferys, 1994; Poil et al., 2011; Ruangkittisakul et al., 2015). The ~300 ms-lasting bell-shaped signal that the LFP represents is due to the fact that typically single spike discharge in each neuron shows a jitter and is phase-locked to a particular time period within the LFP **(Fig. 1-3)**. Both phenomena are perhaps at least partly due to the consequence of a different 'resting' V_m in individual neurons in combination with random occurrence of spontaneous subthreshold PSPs delaying or shortening the time point when V_m reaches spike threshold **(Fig. 1-3)**, as we have hypothesized previously (Rancic et al., 2018). Our findings show that spiking in the LC neuron network is not synchronous. This prompted us to conclude that electrical coupling via gap junctions is not strong enough to cause full synchrony of the network as has been discussed previously (Christie, 1997; Alvarez-Maubecin et al., 2000; Alvarez et al., 2002; Rash et al., 2007; Patel and Joshi, 2015). It seems that the extent of synchrony can be increased or decreased further by neuromodulators as discussed below.

While the rate of phase-locked single spike discharge in newborn rat slices is similar in a given slice with an average of ~1 Hz, intrinsic neuronal membrane properties differ. In newborn rat brainstem–spinal cord preparations, type-1 and type-2 LC neurons differ in STO amplitude and

regularity (Oyamada et al., 1998) while we found that pacemaker, intrinsic burster, and irregular LC neurons can be discriminated by current-evoked depolarization **(Fig. 1-4)**. According to our knowledge, adult LC neurons show exclusively pacemaker discharge in control. It is important to note that morphine application changes spiking from tonic to bursting in adult rat LC neurons in vivo (Zhu and Zhou, 2005) **(Fig. 1-8)**, but it is not clear whether this spike pattern transformation is caused by depolarization-related intrinsic bursting. It can also be due to changed synaptic input as kynurenic acid reverses this spike pattern transformation (Zhu and Zhou, 2005). In that regard, during opioid withdrawal, complex interactions occur between μR, orexin receptor 1 (OX1R), and iGluR within the orexinergic-opioidergic system, particularly for connections between the nucleus paragigantocellularis and the LC (Ahmadi-Soleimani et al., 2014, 2015, 2017; Kaeidi et al., 2015) **(Fig. 1-1)**. Intrinsic bursting in neonatal rat LC neurons is less pronounced than in other neuron types, such as in the inspiratory center (Ballanyi and Ruangkittisakul, 2009) or cortex (van Drongelen et al., 2006). This might partly be due to dialysis of cellular constituents such as cAMP during whole-cell recording, as shown for LC neurons in the newborn rat en bloc model (Oyamada et al., 1998) and in adult rat slices (Alreja and Aghajanian, 1991).

Ion conductances that can be involved in this endogenous bursting are often persistent voltage-gated Na^+ channels, which seem to be functional in the neonatal LC (Kantor et al., 2012) **(Fig. 1-3)**, different types of voltage-gated Ca^{2+} channels, and Ca^{2+}-activated K^+ channels. In adult rat slices, spontaneous (single) spikes or stimulus-evoked spike trains cause activation of voltage-gated Ca^{2+} channels followed by an after-hyperpolarization mainly mediated by Ca^{2+}-activated K^+ channels (Andrade and Aghajanian, 1984). In adult mouse slices, the role of voltage-gated Ca^{2+} channel and Ca^{2+}-activated K^+ channel (subtypes) in LC neuron pacemaker behavior has been

studied in detail (Matschke et al., 2015, 2018). It is not clear yet whether the different neonatal neuron types are located in a particular 'module' area with the neonatal LC and/or project to a specific (group of) target brain areas like in the adult LC (Chandler et al., 2014; Schwarz and Luo, 2015; Li et al., 2016; Poe et al., 2020).

1.3.2. Independence of LC Network Rhythm on Anion Channel-Mediated Inhibition and iGluR

Regarding 'classical' inhibition, blockade of $GABA_AR$ or GlyR causes a rhythm change to seizure-like bursting in the adult and newborn cortex and hippocampus (Jefferys, 1994; Ruangkittisakul et al., 2015; Pires et al., 2021). Similarly, alternating spinal locomotor activity changes to seizure-like synchronous bursting during blockade of these receptors (Bracci et al., 1996; Taccola et al., 2012). In contrast, the primary process of inspiratory rhythm generation in the brainstem does not depend on such inhibition (Feldman and Smith, 1989; Shao and Feldman, 1997; Brockhaus and Ballanyi, 1998; Janczewski et al., 2013). Regarding glutamatergic synaptic transmission, blockade of iGluRs abolishes rhythm in the inspiratory center (Funk et al., 1993; Ballanyi and Ruangkittisakul, 2009), locomotor central pattern generator (Rancic and Gosgnach, 2021), and other brain circuits (Garaschuk et al., 2000; Devor and Yarom, 2002; Bartos et al., 2007; Sipilä and Kaila, 2008; Pires et al., 2021).

Previous in vitro studies using adult rat slices have established that single neuron spiking in the LC persists during blockade of inhibition via $GABA_AR$ and GlyR (Olpe et al., 1988) and of excitation via iGluR (Olpe et al., 1989; Zamalloa et al., 2009). These and related studies also showed that $GABA_AR$ and GlyR activation abolishes single LC neuron spiking whereas iGluR

agonists increase their spike rate (Olpe et al., 1989; Singewald and Philippu, 1998; Zamalloa et al., 2009). Our LFP and V_m recordings revealed that neonatal rat LC neurons already possess functional $GABA_AR$, GlyR, and iGluR, while blocking these receptors does not affect network rhythm.

It can be concluded that neither GABAergic interneurons nor potential tonic release of GABA or glycine from afferent axon terminals within the isolated newborn rat LC are necessary for rhythm. The same can be concluded for eventual spontaneous release of glutamate within the LC in such slices.

1.3.3. iGluR-Mediated LFP Pattern Transformation

We found that the competitive AMPAR and KAR blocker CNQX accelerates the rhythm whereas the specific competitive AMPAR blocker GYKI or the non-specific, non-competitive iGluR blocker kynurenic acid have no effect (Rawal et al., 2019). The CNQX effect is due to the agent acting as a partial agonist on LC neuron AMPARs that are coupled to TARP. As many spontaneously active neural networks depend on active AMPAR-containing synapses, it follows that the yet inhibitory CNQX effect on transmission in these networks abolishes the rhythm despite a potential stimulatory agonistic action on V_m of individual neurons (Feldman and Smith, 1989; Funk et al., 1993; Garaschuk et al., 2000; Devor and Yarom, 2002; Bartos et al., 2007; Sipilä and Kaila, 2008; Ballanyi and Ruangkittisakul, 2009; Rancic and Gosgnach, 2021). As the neonatal LC rhythm does not depend on iGluR, we showed for the first time that activation of the TARP–AMPAR complex has a stimulatory effect on a spontaneously active neural network.

In some slices from our study on the TARP–AMPAR complex (Rawal et al., 2019) we noticed that the amplitude of LFP rhythm fluctuates during CNQX-mediated stimulation. Similarly, α-amino-3-hydroxy-5-methyl-4-isoxazolepropionic acid (AMPA), kainate (KA), and N-methyl-D-aspartic acid (NMDA) merge separate bursts into faster sinusoidally-shaped oscillations showing spindle-like amplitude variations. As one possible explanation, this transformed LFP pattern might represent summation of enhanced STOs in LC neurons that are strongly electrotonically coupled in newborn rats (Christie et al., 1989; Marshall et al., 1991; Ishimatsu and Williams, 1996; Alvarez et al., 2002). As examples for this mechanism in neonatal rats, KA or the cholinergic agonist carbachol induce STOs that summate to spindle-shaped γ-type LFP oscillations in the CA_3 hippocampal area. These oscillations are, however, notably faster than those in the LC (Bartos et al., 2007; Poil et al., 2011; Tsintsadze et al., 2015). Similarly, STOs are involved in sleep-related γ spindles in the adult brain (Lüthi, 2014; Sullivan et al., 2014). Moreover, most inferior olive neurons, which share various properties with the neonatal LC, such as strong coupling via gap junction, show rhythmic variations in frequency and amplitude of STOs (Devor and Yarom, 2002). As STO variations were blocked by CNQX in that juvenile rat brain slice study, the authors concluded that tonic depolarizing glutamatergic input is involved in this phenomenon. Indeed, we found that during AMPA or KA LC neurons show a modest depolarization and 'tonic' increase in spike rate with no rhythmic amplitude changes of either spikes or underlying STOs. Possibly, the spindle-shaped amplitude LFP fluctuations are due to a rhythmic change in the extent of phase-lock of individual neuron discharge regarding the network output (Bartos et al., 2007) and this increase in phase-lock towards higher synchrony can be due to an enhanced coupling of gap junctions (Posłuszny, 2014). In that regard, NMDA stabilizes synchronized LFP oscillations in gap junction-coupled inferior olive neurons of rat slices. This process involves Ca^{2+}/calmodulin-

dependent protein-kinase-I activation which enhances weak coupling of non-neighboring neurons (Turecek et al., 2014). In contrast, in the adult rat LC, neuromodulators (including glutamate) presumably do not directly counteract the postnatal decrease of gap junction coupling and, instead, neuromodulator-evoked spike slowing itself reverses this decrease (Alvarez et al., 2002). We found that NMDA-evoked acceleration of rhythm is accompanied by increased synchrony which we could not yet confirm for the network oscillations due to AMPA and KA. In each case, though, all three agents increased the regularity of LFP rhythm.

In neonatal LC neurons, NMDA causes crescendo-shaped rhythmic sustained depolarizations and concomitant spike discharge followed by hyperpolarizations that are closely related timewise to the oscillation train LFP pattern **(Fig. 1-5)**. Detailed pharmacological analysis is required to analyze cellular mechanisms underlying NMDA-evoked bursting that can include modulation of Ca^{2+}-dependent STOs and a variety of other processes (Neuman et al., 1989; Zhu et al., 2004; Sharifullina et al., 2008; Mrejeru et al., 2011). While many questions remain regarding the iGluR agonist-evoked LFP pattern transformations, our findings support the hypothesis based on in vivo findings of morphine-evoked bursting in the LC of adult rats that iGluR within the LC is needed for the spike pattern transformation of its neurons by opioids (Zhu and Zhou, 2005) **(Fig. 1-8)**.

1.3.4. LFP Pattern Transformations by μ-Opioid and α_2 Receptors

The very similar complex inhibitory effects of μR and α_2R activation on the newborn rat LFP (Rancic et al., 2018) **(Figs. 1-7,1-8)** are not surprising as they act on the same $G_{i/o}$-mediated cellular signaling pathway coupled to GIRKs (North and Williams, 1985; Aghajanian and Wang, 1987). For slice studies on the LC, mostly high doses were used that result in blockade of neuronal spike

discharge due to pronounced GIRK channel-mediated hyperpolarization. We found that low morphine, DAMGO, or clonidine doses slow LFP rhythm and evoke a (crescendo-like) multipeak burst pattern. As one explanation, low doses of these μR and α_2R agonists may have a modest hyperpolarizing action on LC neurons. Due to the differences in resting V_m and subthreshold EPSPs and IPSPs, this might increase the differences in time points at which each neuron reaches spike threshold. Additionally, the possibility of presynaptic effects cannot be excluded. However, as noted above, LFP rhythm does not depend on classical synaptic processes and may rather rely on intrinsic STOs and gap junction coupling. While the observed LFP pattern transformation occurred only in a narrow nanomolar dose range of about one order of magnitude, it is not clear which concentrations are reached in the LC of adult rats in vivo when μR agonists are applied (systemically) to cause slow LC neuron bursting (Ruangkittisakul et al., 2015; Ballanyi and Eschenko, 2022). Additionally, in the latter studies it is not clear whether the agonists act directly on the LC or rather on afferent circuits which then induce synaptically-mediated bursting (see above). It is also unknown in which way iGluRs act to support such bursting (Zhu and Zhou, 2005) **(Fig. 1-8)**. These considerations also raise the question of which opioid and clonidine doses occur in the LC during their recreational and therapeutic effects. In that regard, under very similar in vitro conditions, ~100 nM DAMGO or fentanyl block rhythm in the isolated inspiratory center (Ballanyi and Ruangkittisakul, 2009; Ruangkittisakul and Ballanyi, 2010).

1.3.5. Ca_i Responses in the Neonatal LC

Our immunohistochemistry (Rawal et al., 2019) and Ca_i imaging results in newborn rat slices (Ruangkittisakul et al., 2009) showed firstly that LC neuron somata were densely packed whereas somata of intermingled astrocytes were notably fewer and smaller **(Fig. 1-2)**. Despite a smaller

number of somata, astrocyte processes might spread throughout the LC and may contain the receptors needed for their communication with neurons. One novel type of communication is via lactate, which seems to be released upon α_1R activation from astrocytes and diffuses to neighboring neurons to excite them via a novel receptor (Tang et al., 2014; Teschemacher and Kasparov, 2017) **(Fig. 1-1)**. While the latter findings were obtained in cultured LC slices, we made similar observations regarding lactate in the acutely isolated newborn rat slices. We also found that the presumptive astrocytes respond to various neuromodulators in a fashion distinct to neurons. Specifically, NA decreased Ca_i baseline in neurons while inducing a concentric Ca_i wave starting in the dense network of astrocytes surrounding the LC **(Fig. 1-9)**. DAMGO also decreased baseline Ca_i in neurons while it did not affect astrocytes. The astrocytic Ca_i increases during NA are likely due to metabotropic Ca^{2+} release from endoplasmic reticulum stores and this has been shown to occur in several brain regions in wave-like fashion based on gap junction coupling (Ruangkittisakul et al., 2009; Halassa and Haydon, 2010). In contrast, the DAMGO- and NA-evoked neuronal Ca_i decreases are, at least to a major extent, likely due to decreased Ca^{2+} influx associated with the hyperpolarization and concomitant spike blockade, resulting in inactivation of spike-related and persistently open ('tonic') voltage-gated Ca^{2+} channels. Our observation that ATP and t-ACPD also cause a notable (wave-like) Ca_i rise in astrocytes vs. a modest response in neurons indicates that neurons do not have a major amount of Ca^{2+} stored in the endoplasmic reticulum and/or may not have purinergic or metabotropic glutamate receptors for the latter agonists, respectively.

Ca_i baseline in neonatal LC neurons also increases modestly with similar magnitude and kinetics in all analyzed neurons during CNQX-evoked acceleration of rhythm (Rawal et al., 2019). These

Ca_i rises are likely mainly due to enhanced activation of tonic voltage-gated Ca^{2+} channels, possibly in concert with a minor influx through the potentially Ca^{2+}-permeable AMPAR (Metzger et al., 2000; Traynelis et al., 2010). We proposed that most LC neurons express TARP–AMPAR complexes or that they are at least in some neurons secondary to gap junction coupling, causing a similar depolarization of neighboring cells lacking a functional TARP–AMPAR complex (Rawal et al., 2019).

The fact that no rhythmic neuronal Ca_i rises were seen during single spikes or crescendo-like multipeak bursts during recovery from high DAMGO or NA is likely caused by the limited time resolution of our scanning population imaging approach at ~1 frame/s. Accordingly, rhythmic single spike-related (dendritic) Ca_i rises were recorded in LC neurons from adult mouse slices using fast line-scan imaging (Sanchez-Padilla et al., 2014) **(Fig. 1-10)**. With our approach, rhythmic neuronal Ca_i rises were only seen during sustained LFP bursting in 7 or 9 mM K^+ solution **(Fig. 1-10)**. Moreover, robust neuronal Ca_i rises occurred in response to tetanic stimulation of the pericoerulear areas surrounding the LC soma region. While the blocking effects of CNQX and prazosin **(Fig. 1-10)** indicate that the Ca_i rises in most stimulation sites involve AMPAR/KAR and α_1R activation, respectively, it is possible that stimulation of other (more remote) sites reveals other synaptic inputs to the LC network. As an important new result, stimulation evoked either only a Ca_i rise or a rise followed by an undershoot below baseline. The undershoot likely involves α_2R activation based on findings from V_m recording in adult rat slices showing that single electrical stimuli cause an iGluR mediated EPSP followed by a prolonged α_2R-mediated afterhyperpolarization (Williams et al., 1991). The finding of two different neuronal response types

to tetanic stimulation in neonates is further indication of non-uniform neuronal properties similar to those of the adult LC.

In summary, our Ca_i imaging findings are a first important step to elucidate receptors and signaling pathways in the neonatal LC. In the next section, we refer to how our in vitro approaches can be complemented by other approaches in future studies and how the findings relate to the current understanding of the modular organization of the adult LC.

1.3.6. Conclusions and Perspective

The previous and current findings on the isolated newborn rat LC indicate clearly that this neural network is already very complex at birth and also possibly has a modular organization such as that in adults. Further novel neonatal LC properties will certainly be detected with the in vitro techniques used so far, specifically bath-application of drugs, LFP recording, cell-attached plus whole-cell spike and PSP analysis, and population Ca_i imaging. However, other approaches discussed in the following will likely lead to other novel findings. For several years, in vivo studies in the adult rodent LC have used powerful approaches including optogenetic and chemogenetic stimulation in genetically-engineered animals, sometimes combined with subsequent in vitro analyses, e.g., electrophysiological recording and pharmacology in slices or immunohistochemistry (Carter et al., 2010; Tang et al., 2014; McCall et al., 2015; Li et al., 2016; Yamaguchi et al., 2018). However, genetic engineering in newborns is only a newly emerging field as the manipulation must occur in utero (Bitzenhofer et al., 2017). Furthermore, acute approaches such as drug injection or electrophysiological recording, e.g., with multi-site electrodes

(Eschenko et al., 2012; Totah et al., 2018, 2021) are challenging in the very small neonatal LC. Accordingly, we focus here on future in vitro techniques.

Regarding pharmacology, bath-application of drugs partly mimics autocrine LC neuromodulation. This holds particularly true for NA (ant)agonists because strong excitatory afferent inputs to (a subpopulation of) LC neurons increases the spike rate not only of these cells, but likely also neighboring neurons due to gap junction coupling. The increased spiking would then cause a global NA release within the LC that then has feedback effects on both neurons (via auto α_1R and α_2R) and astrocytes (via α_1R). Modest effects of, e.g., iGluR, $GABA_A$R, or μR activation might be more localized if neonatal LC neurons have a modular organization regarding expression of such receptors. To analyze this, drugs can be focally injected into LC subareas during electrophysiological LFP and/or cellular recording. In that regard, it can be tested whether findings from drug injection into the LC soma region differs from those upon focal application to the pericoerulear region where autocrine synaptic integration is prominent (Ivanov and Aston-Jones, 1995; Ishimatsu and Williams, 1996). Regarding recording, multi-electrode arrays (Brofiga et al., 2021) would be suitable to detect, e.g., whether some LC neurons respond with bursting to focal drug application. Moreover, whole-cell recording of V_m changes (and underlying ion currents in voltage-clamp) can be combined with imaging of cellular factors such as Ca_i or cAMP under the influence of drugs. After whole-cell recording, the cytoplasm can be harvested for identifying via PCR analysis neuron type-specific ion channels or receptors (Sucher and Deitcher, 1995). Specific afferent inputs to (subpopulations of) LC neurons can be identified via electrical stimulation in LC slices sectioned at an angle that would preserve axon tracts from remote brain areas. In that regard, focal LC stimulation would possibly reveal that modules within the LC respond with LFP and

possibly also V_m pattern transformation to iGluR, μR, OX1R, or α_2R activation. One promising rat slice model in that respect retains functional connectivity from neurons of the nucleus paragigantocellularis to those in the LC (Kaeidi et al., 2015). It would also be important to use slices in which LC output tracts are preserved to identify whether particular axons propagate spike bursts during LFP pattern transformations evoked by the latter receptors. Regarding the LFP pattern transformation, data from simultaneous LFP or multi-electrode array recording combined with monitoring single neuron V_m changes can be used for modeling, e.g., of spindle-shaped AMPAR- and KAR-mediated LFP oscillations whose shape resembles γ-oscillations elicited by bath-applied KA in cortical slices which are thought to provide a temporal structure for information processing in the brain (Bartos et al., 2007). As examples for topics to be studied with such approaches, one could analyze how iGluR, μR, and OX1R eventually cooperate to transform LC neuron LFP and possibly also single neuron discharge patterns like in adult rats in vivo (Zhu and Zhou, 2005). Regarding modeling, approaches like those used in the inferior olive may be applied. Specifically, it has been shown that two principal characteristics of its neurons, i.e., STO and electrical gap junctions, make this system a powerful encoder and generator of spatiotemporal patterns with different but coordinated oscillatory rhythms (Latorre et al., 2013).

1.4. Aims and Hypotheses

As noted above **(1.1.2.)**, the adult LC has a modular organization enabling this small neural network to control multiple brain functions **(Fig. 1-1)**. Substantially less is known about functional properties and the organization of the LC in newborns (**1.3.4.**). Based mainly on in vitro studies using brain slices, it was thought for long that regular spontaneous spiking of neonatal LC neurons is synchronous due to their extensive gap junction coupling, contrary to more complex discharge

patterns in adults. But, the neonatal LC is not a simple, synchronous, spike-generating circuit as demonstrated by previous studies from our group using horizontal neonatal rat brain slices (Kantor, 2012; Panaitescu, 2012; Rancic et al., 2018; Rawal, 2019; Rawal et al., 2019; Rawal and Ballanyi, 2022; Rawal et al., 2022) **(Fig. 1-2)**. These reports showed that the newborn LC generates a LFP comprised of asynchronous and rather phase-locked spikes and that generation of this robust neural network rhythm does not depend on either iGluR-mediated excitation or $GABA_AR$/GlyR-mediated inhibition **(Figs. 1-3, 1-5, 1-6)**. Furthermore, subpopulations of LC neurons possess distinct intrinsic ion conductances that mediate either conditional burster- or pacemaker-type discharge versus irregular spiking **(Fig. 1-4)**. Moreover, findings using Ca_i imaging during tetanic electrical stimulation indicate that one subpopulation of LC neurons responds with EPSPs whereas the remaining neurons show an EPSP-IPSP sequence **(Fig. 1-10)**. Finally, the pattern of LFP rhythm transforms under the tonic influence of neuromodulators. Namely, iGluR activation with AMPA, KA or NMDA evokes fast LFP oscillations with distinct pharmacological properties (Rawal and Ballanyi, 2022; Rawal et al., 2022) **(Fig. 1-5)** whereas raising extracellular K^+ can cause slow LFP bursts **(Fig. 1-10)** and μR or α_2R activation elicits also slow, but less robust crecendo-shaped (multipeak) bursts **(Figs. 1-7, 1-8)**. Preliminary analysis of unpublished data from our group indicated that NA can also cause a slow multipeak LFP pattern while evoking a concentric Ca_i wave in astrocytes that originates in the periphery and subsequently propagates towards the LC center **(Fig. 1-9)**.

In our previous studies, drugs were administered via bath-application. This approach should optimally be combined with local drug injection or, if feasible, (opto)genetic manipulation as, for example, opioids may affect only a subpopulation of LC neurons in an intact animal. However, for

NA, bath-application can mimic autocrine activity in the neonatal LC in which interstitial NA may substantially increase throughout the nucleus during enhanced neuronal spiking that results in NA release from proximal axon collaterals (Cedarbaum and Aghajanian, 1978; Baral et al., 2022). The activity-related increase in interstitial NA then acts back on LC neurons via α_1R and α_2R (Nakamura et al., 1988; Delaville et al., 2011; Schwarz and Luo, 2015) and likely also on neighbouring astrocytes expressing α_1R (Tang et al., 2014; Teschemacher and Kasparov, 2017). Presumably, α_1R activation in LC astrocytes stimulates them to release lactate which subsequently depolarizes neighboring LC neurons via a novel receptor to increase their spike rate for evoking a further NA release (Tang et al., 2014; Teschemacher and Kasparov, 2017) (**Fig. 1-1**). This scenario indicates that LC neurons and astrocytes interact mutually as in various other brain circuits (Perea and Araque, 2005; Halassa and Haydon, 2010; Wahis and Holt, 2021).

As the overarching aim of this thesis, experiments were designed in acutely isolated slices retaining the connectivity between these brain cells similar to in vivo to establish a basis for future studies on network complexity in the neonatal LC, particularly involving NA-mediated LC neuron-glia interaction. Improved understanding of neonatal LC function/dysfunction can contribute to development of new treatments for pathologies involving (changes in) activity of this network, such as sudden infant death syndrome (Lavezzi et al., 2005).

For this, NA effects were studied at a concentration that changes the LFP-recorded network rhythm as well as the activity of populations of neurons and astrocytes monitored with Ca_i imaging. This imaging approach of cellular activity is indirect as in neurons enhanced spontaneous spiking causes a rise of Ca_i baseline that is the consequence of potentiated activation of voltage-gated Ca^{2+}

channels combined with release of Ca^{2+} from endoplasmic reticulum stores (Hille, 1984; Ballanyi and Kulik, 1998; Metzger et al., 2000). Although astrocytes also possess such voltage-gated channels, rises of Ca_i baseline in their somata are typically a result of endoplasmic reticulum store release in response to neurotransmitter-evoked G protein-coupled receptor (GPCR) activation (Carmignoto et al., 1998; Fiacco and McCarthy, 2006; Verkhratsky and Parpura, 2014; Bazargani and Attwell, 2016). Due to gap junction coupling and release of extracellular signalling molecules, such astrocyte activity can propagate in wave-like fashion in brain cultures (Cornell-Bell et al., 1990), slices (Basarsky et al., 1998), whole retinae (Newman and Zahs, 1997), and in vivo (Hirase et al., 2004).

Previous Ca_i imaging and immunohistochemistry data from our group indicated that the neonatal LC is apparently comprised of ~90% neurons with a soma diameter of >20 µm and ~10% astrocytes with a soma diameter of ~10 µm and it appeared (but was not analyzed) that astrocytes are more densely packed in peripheral tissue compared to the LC (Rawal et al., 2019) (**Fig. 1-9**). Structural astrocyte organization in the brain has long been characterized by 'tiling' whereby each cell occupies a distinct territory (Grosche et al., 2002; Oberheim et al., 2006; Halassa et al., 2007). However, there is increasing evidence that astrocyte arrangement is variable and specifically adapted to different neural circuits such as in the visual cortex (Lopez-Hidalgo et al., 2016) and hippocampus (Ogata and Kosaka, 2002). Moreover, astrocytes occupying particular brain regions might be specialized for interactions with neurons and give rise to the functions of the neuronal domains they neighbour (Tsai et al., 2012). Regarding the LC, in slices from 4–10 days-old rats functional interaction of neurons and astrocytes might be facilitated by gap junction-coupling between both brain cell types (Alvarez-Maubecin et al., 2000). However, there are currently no

studies that identified a particular array of the location or density of LC astrocytes that may support such an interaction.

One specific aim of this thesis was therefore to determine whether there is a particular distribution of astrocytes in the neonatal LC which may indicate at a novel structure-function relationship for this type of glial cell. This was studied by firstly quantifying the LC extension and the density of surrounding versus internal astrocyte somata in TH- and S100β-stained preparations from our previous study (Rawal et al., 2019) (**Fig. 1-9**). Then, immuno-histochemistry-based findings on astrocyte distribution were compared with that in Fluo-4-loaded astrocytes in a single confocal imaging plane during Ca_i imaging when 500 µM or 1 mM glutamate was applied to evoke a large fluorescence increase. For a better discrimination of neurons from astrocytes during such imaging (apart from their different soma size), responses of cells to NA were used as preliminary data from our group suggested that NA caused astrocytes to flash up while instead dimming neurons.

The other specific aim of this thesis was to characterize the LC network response to autocrine NA activity. A previous study from our group showed that CNQX acts as a partial agonist on the TARP-AMPAR complex in LC neurons of newborn rat slices to cause a 3 mV depolarization leading to a 2.3-fold increase in the rate of tonic spiking and an accompanying increase of Ca_i baseline (Rawal et al., 2019) (**Figs. 1-5,1-9**). These findings indicate that a change in Ca_i baseline can be used in neonatal LC neurons as indication of an excitatory versus inhibitory effect that can principally both be evoked during autocrine modulation of the LC by NA acting on neuronal α_1R and α_2R autoreceptors, respectively (Nakamura et al., 1988; Delaville et al., 2011; Schwarz and Luo, 2015). LFP recording was combined with Ca_i imaging firstly during bath-application of 25

μM NA as our preliminary data indicated that this dose evokes the presumably concentric astrocyte Ca_i wave while decreasing Ca_i baseline in neurons and slowing LFP rhythm (eventually with appearance of multipeak events). Neuronal and astrocytic responses were then compared to those during t-ACPD and ATP to determine whether they could also evoke astrocyte waves, and whether specific subpopulations of each cell type were responding to each modulator indicating a modular organization. Both agents can affect neuronal and astrocytic Ca_i via action at metabotropic and/or ionotropic receptors making them suitable for comparison with NA effects on neurons as well as astrocytes (Ruangkittisakul et al., 2009; Sun et al., 2013; Verkhratsky and Parpura, 2014; Bazargani and Attwell, 2016; Rajani et al., 2018).

Regarding neonatal LC astrocytes, the following hypotheses are proposed:

(i) They are less densely distributed within the center of the nucleus than at its rim and, particularly, in surrounding areas.

(ii) NA, t-ACPD and ATP differ in their capability to evoke a concentric Ca_i wave.

(iii) In line with a modular LC organization, NA, t-ACPD or ATP show regional differences in the expected Ca_i rise.

Regarding neonatal LC neurons, the following hypotheses are proposed:

(i) At a dose evoking the astrocytic Ca_i wave, NA acts inhibitory as evident from LFP slowing and a Ca_i baseline decrease.

(ii) ATP and t-ACPD will act excitatory and cause a Ca_i rise

(iii) In line with a modular LC organization, neuronal responses to NA show regional differences compared to ATP and t-ACPD

1.5. Figures and Legends

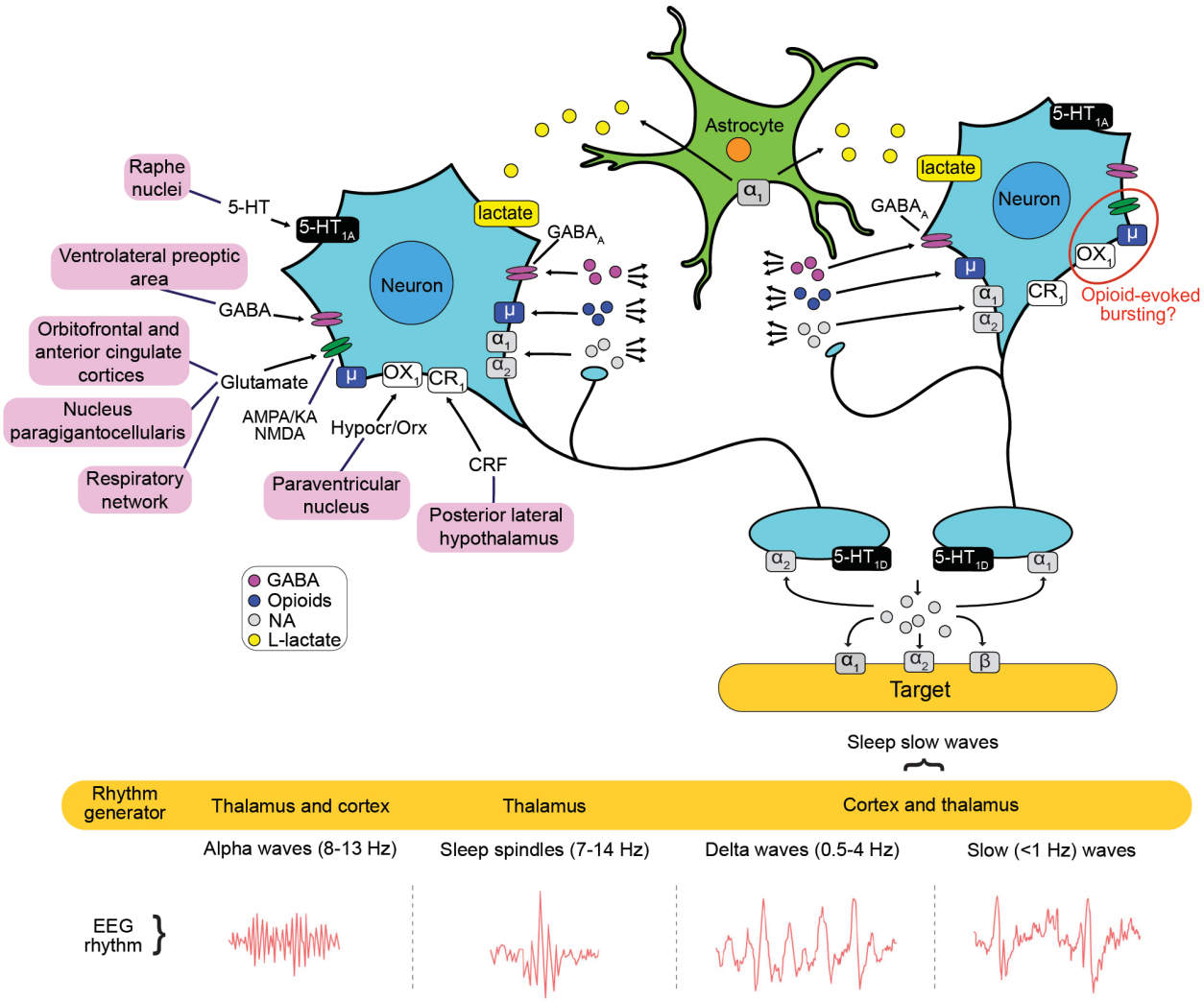

Fig. 1-1: Adult locus coeruleus (LC) connectivity. The LC in adult mammals receives synaptic input from diverse remote brain circuits exemplified in the upper left section. The input involves a variety of neurotransmitters acting on different receptor (R) subtypes, e.g., such as glutamate on ionotropic R-subtypes (iGluR) activated by either α-amino-3-hydroxy-5-methyl-4-isoxazolepropionic acid (AMPA), kainate (KA), and N-methyl-D-aspartate (NMDA), γ-aminobutyric acid (GABA) on $GABA_AR$, serotonin (5-HT) on $5\text{-}HT_{1A}R$ or $5\text{-}HT_{1D}R$, peptides such as endogenous opioids on μ-receptors (μR), hypocretin (Hypocr), orexin (Orx) acting, e.g., on OX1R and corticotropin-releasing factor (CRF). As shown in the middle right and lower section, LC neurons release in remote brain areas in most parts of the neuraxis their main neurotransmitter noradrenaline (NA) which acts on either α_1, α_2, or β R-subtypes, and possibly a LC neuron subtype-specific co-transmitter such as the peptide galanin or neuropeptide-Y. By activity-related NA and co-transmitter release, the LC controls (spontaneous) activities of brain circuits, e.g., in the thalamus or cortex, to modulate electroencephalogram (EEG) patterns or

behaviors such as sleep. At the same time, some of the neurotransmitters act in feedback fashion on presynaptic synapses on the same LC neuron. Importantly, some LC neuron collaterals terminate within the LC to release NA and their co-transmitter for acting on neighboring neurons or astrocytes shown in the upper section. Astrocytes possess, for example, α_1R whose activation might cause release of the metabolite L-lactate that then stimulates LC neurons via a novel R type. Neuron–neuron and neuron–astrocyte interactions serve for autocrine control within the LC. Note that the red circle in the LC neuron in the upper right part indicates one example for an interaction between postsynaptic Rs. Specifically, μR might interact with iGluR and OX1R during opioid actions. All these functions, and other properties described in the main text, show that the adult LC has a complex connectivity and modular organization for enabling its diverse control functions. The schema is partly based on that from (Benarroch, 2009). Schema of EEG recordings adapted with permission from (Crunelli et al., 2018).

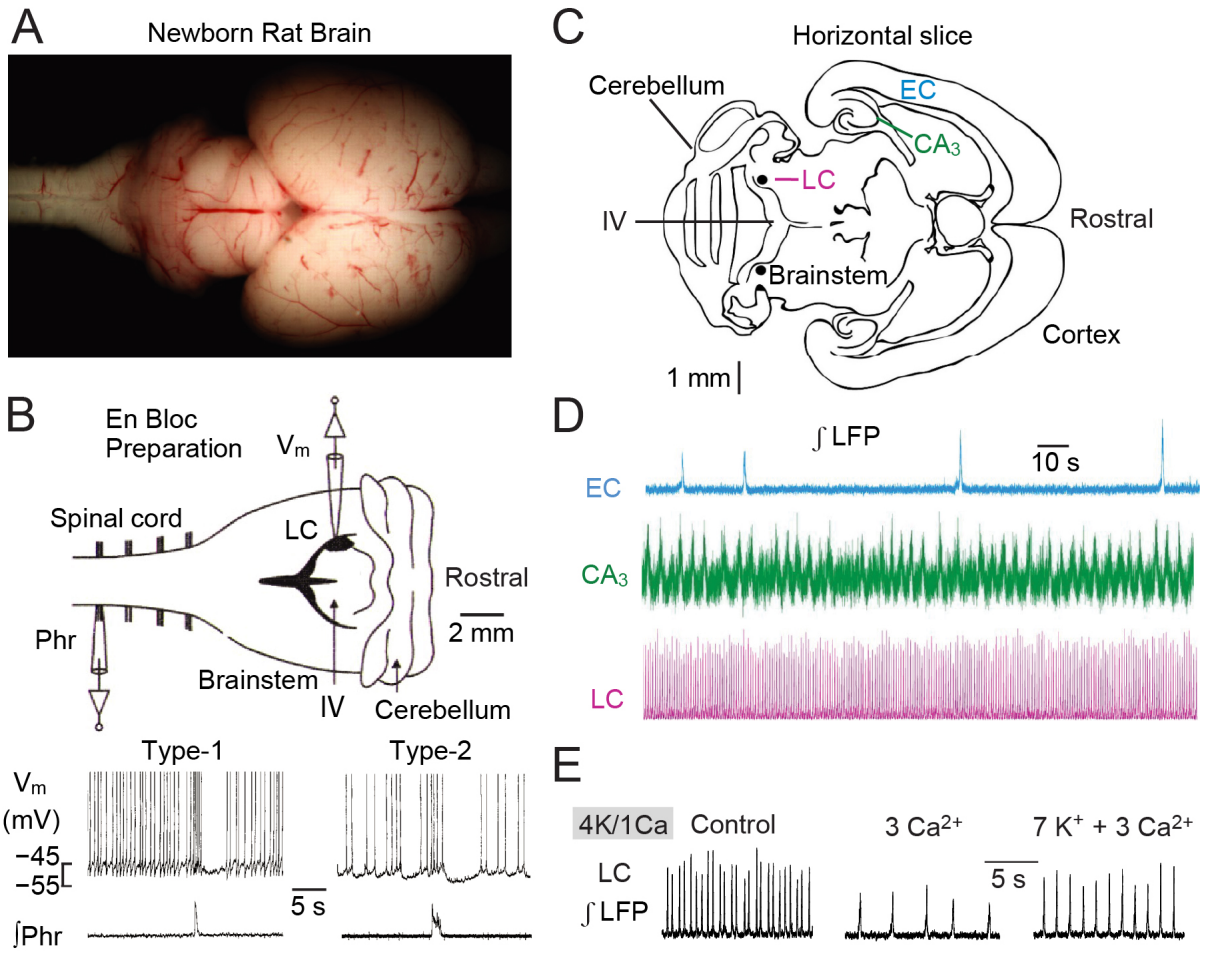

Fig. 1-2: Spontaneous rhythms in LC, cortex and hippocampus of horizontal newborn rat brain slices. A, the image in the upper left section shows a dorsal view on the isolated brain and parts of the cervical spinal cord. **B,** displays in upper part a schema for simultaneous suction electrode recording of integrated inspiratory-related phrenic nerve (Phr) activity from a ventral spinal rootlet and whole-cell membrane potential (V_m) recording from neurons in the LC indicated as a black oval located close to the 4th ventricle (IV). The lower part illustrates that spontaneous inspiratory phrenic bursts evoke in both neurons an initial acceleration of spontaneous LC neuron action potential ('spike') discharge followed by a hyperpolarization and concomitant spike blockade lasting ~5 s. In the 'type-1′ neuron on the left, subthreshold oscillations (STOs) of V_m and concomitant spike discharge are very regular, contrary to more irregular STOs and spiking in the 'type-2' neuron in the right. **C,** schema of a 400 µm thick horizontal slice at a section level that enables simultaneous recording of spontaneous local field potential (LFP) rhythms in entorhinal cortex (EC), CA_3 hippocampal area (CA_3), and LC brainstem area. **D**, simultaneous suction electrode recordings from the surface of a slice kept in superfusate containing (among other components) 4 mM K^+ and 1 mM Ca^{2+} ('4K/1Ca'). LFPs were differentially amplified (×10 k) and band-pass filtered (0.3–3 kHz) and integrated at a time constant of 20 ms using a 'moving

averager'. Note that rhythms have a rate of 1–4 bursts/min in EC, 10–40 bursts/min in CA_3 area and 0.5–3 Hz in LC. **E**, an increase of superfusate Ca^{2+} from physiological 1 to 3 mM, almost abolishes the LC LFP. Use of elevated superfusate Ca^{2+} might partly explain why LFPs have not been recorded previously in LC. Note that our group uses typically a 3K/1.2Ca superfusate. **A** from (Waselenchuk et al., 2022); **B** adapted with permission from (Oyamada et al., 1998); **C–E** adapted with permission from (Kantor, 2012).

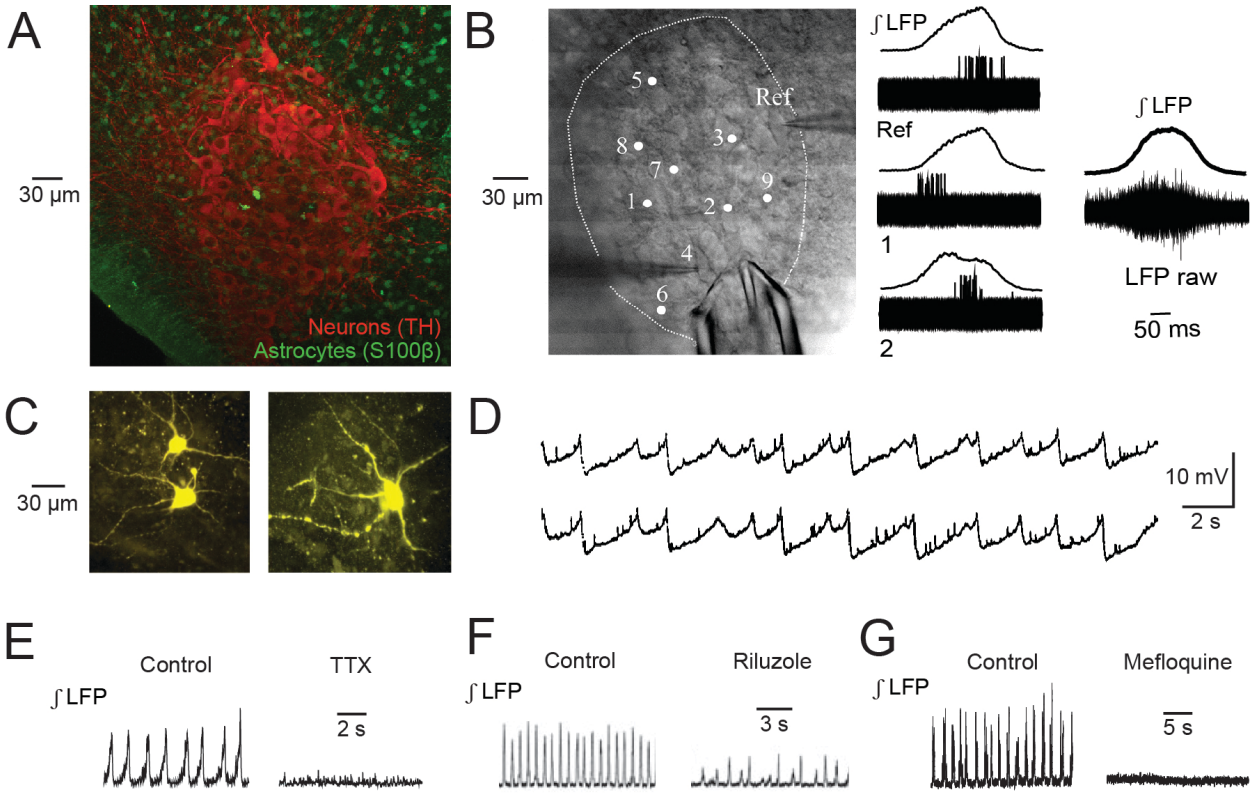

Fig. 1-3: Cell morphology, 'phase-locked' spiking and related basic neuronal properties in newborn rat LC slices. A, image shows in a chemically fixed slice with double immuno-histochemical staining that the LC is comprised of ~90% densely packed tyroxine-hydroxylase (TH)-positive neurons with a mostly >20 µm soma diameter while smaller cells are glial cells, mostly S100β-positive astrocytes. **B**, traces next to image show overlay of 20 cycles of averaged integrated suction electrode-recorded LFP traces monitored simultaneously with single neuron spiking detected with a 'cell-attached' patch electrode. Spiking in a reference neuron (Ref) was continuously monitored with consecutive recording in a further 9 neurons (cells 1 and 2 displayed here). Traces on the right show the averaged integrated LFP and overlaid raw LFP signals from all cycles. Such spike tracking revealed that LC neurons discharge (with a 'jitter') during a particular phase of the LFP comprising overlaid spiking of 3–10 neurons. **C**, the morphology of neurons filled with lucifer-yellow via the patch electrode during whole-cell V_m recording. **D**, synchronous V_m STOs in 2 simultaneously recorded LC neurons. The smaller and shorter V_m depolarizations may reflect spontaneous postsynaptic potentials (PSPS). **E**, LFP rhythm is abolished by bath-application of the voltage-gated Na^+ channel blocker tetrodotoxin (TTX, 50 nM) or the connexin-32 gap junction blocker mefloquine (100 µM). **A** adapted with permission from (Rawal et al., 2019); **B**,**E**–**G** adapted with permission from (Rancic et al., 2018); **C** from (Panaitescu and Ballanyi, 2022); **D** adapted with permission from (Christie et al., 1989); Copyright (1989) Society for Neuroscience.

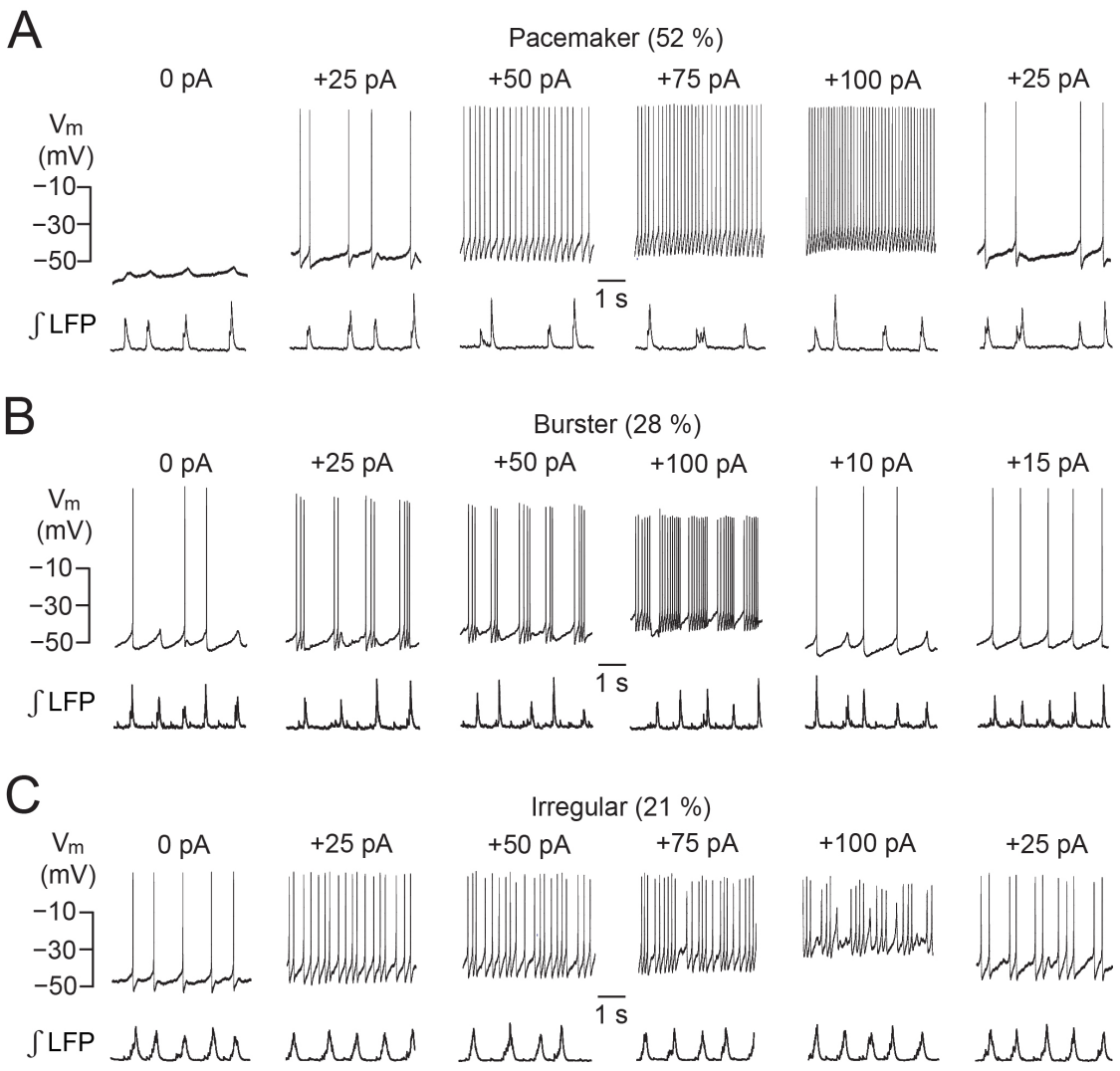

Fig. 1-4: Intrinsic spike patterns in LC neurons of newborn rat slices. A, depolarization of a whole-cell-recorded 'pacemaker'-type neuron by current injection through the patch electrode shows a gradual increase in the rate of very regular spiking between 25 and 100 pA. Note that this cell shows only STOs in control due to its quite negative resting V_m. **B**, depolarization of a 'burster'- type neuron evokes groups of spikes whose number increases with the extent of depolarization. **C**, depolarization of an 'irregular'-type neuron only modestly increases spike rate at 25 to 100 pA. Numbers indicate the percentage of occurrence of these neuron types based on 29 recordings. For our whole-cell V_m recordings (see also **Figs. 1-5A,C, 1-6C,** and **1-7C**), access resistance was compensated during a test pulse at the beginning of a recording and was also checked, and eventually adjusted, later during the measurement. Access resistance typically ranged between 10–50 MΩ and was stable in >95% of neurons even during recordings lasting > 1 h. For determining neuronal input resistance ranging from 120–370 MΩ, hyperpolarizing current pulses (50–100 pA) were injected, mostly at an interval of 10–15 s (see **Figs. 1-6C** and **1-7C**). From (Waselenchuk et al., 2022).

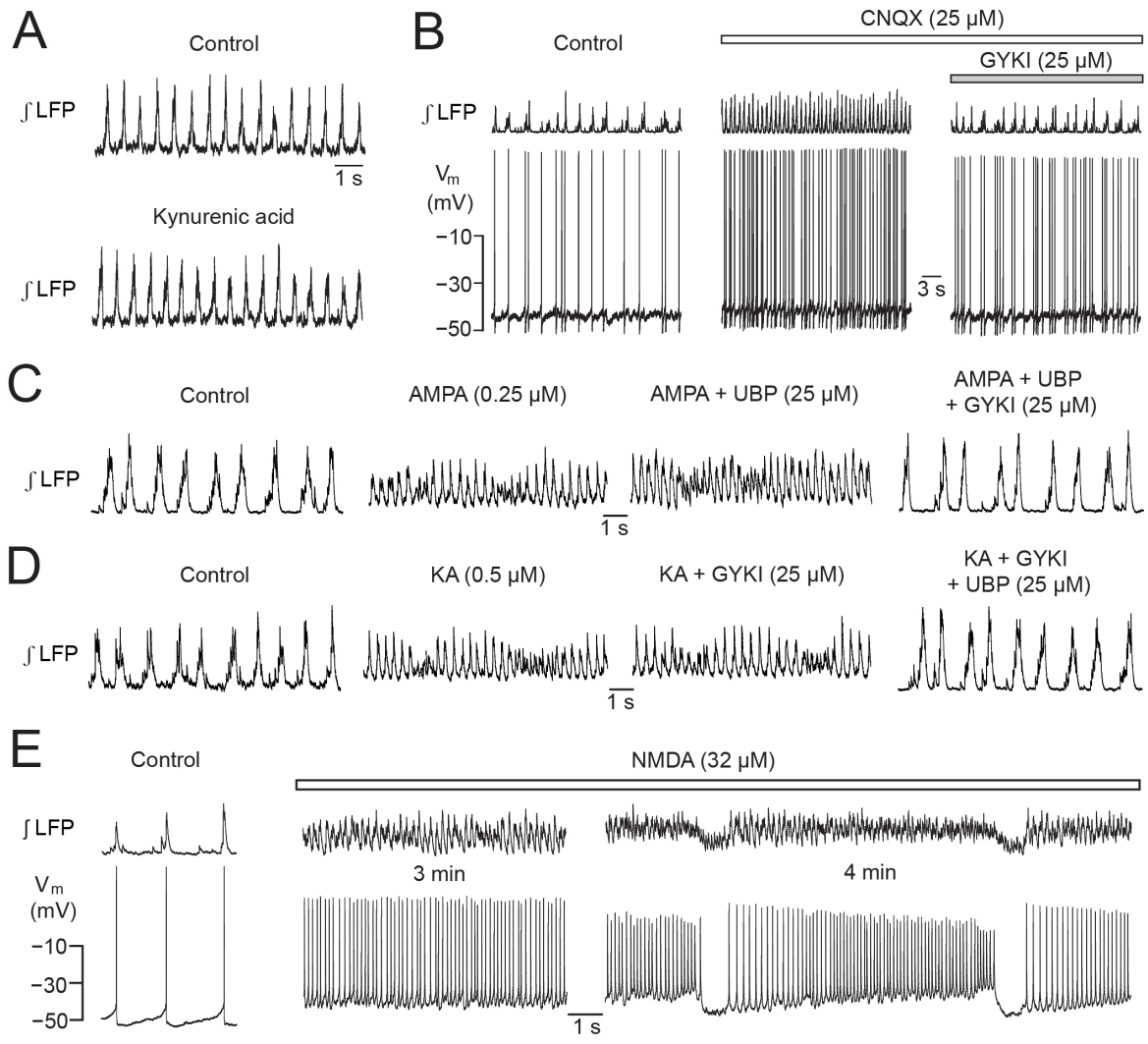

Fig. 1-5. iGluR (ant)agonist effects on LC activities in newborn rat slices. A, bath-application of 2.5 mM of the broad-spectrum competitive iGluR blocker kynurenic acid for 5 min does not affect LFP. **B**, acceleration of LFP rhythm by bath-applied 6-cyano-7-nitroquinoxaline-2,3-dione (CNQX) is accompanied by modest V_m depolarization leading to faster cellular spiking. These stimulatory CNQX effects are reversed within 2 min after start of adding 25 μM GYKI to the CNQX-containing solution. **C**, bath-applied AMPA evokes fast LFP oscillations with spindle-shaped amplitude fluctuations that persist after adding the KAR antagonist UBP-302 but are blocked by further addition of GYKI. **D**, bath-applied KA evokes very similar LFP oscillations that persist after adding GYKI but are blocked by further addition of UBP. **E**, several minutes after start of NMDA application, V_m oscillations become interrupted by ~1 s-lasting rhythmic hyperpolarizations causing spike blockade for ~1 s. The resulting LFP oscillation trains start after the inactivity phase with concomitant progressive neuronal depolarization leading to accelerated spiking (right panels). **A**,**B** adapted with permission from (Rawal et al., 2019); **C**,**D** from (Rawal and Ballanyi, 2022); **E** from (Rawal et al., 2022).

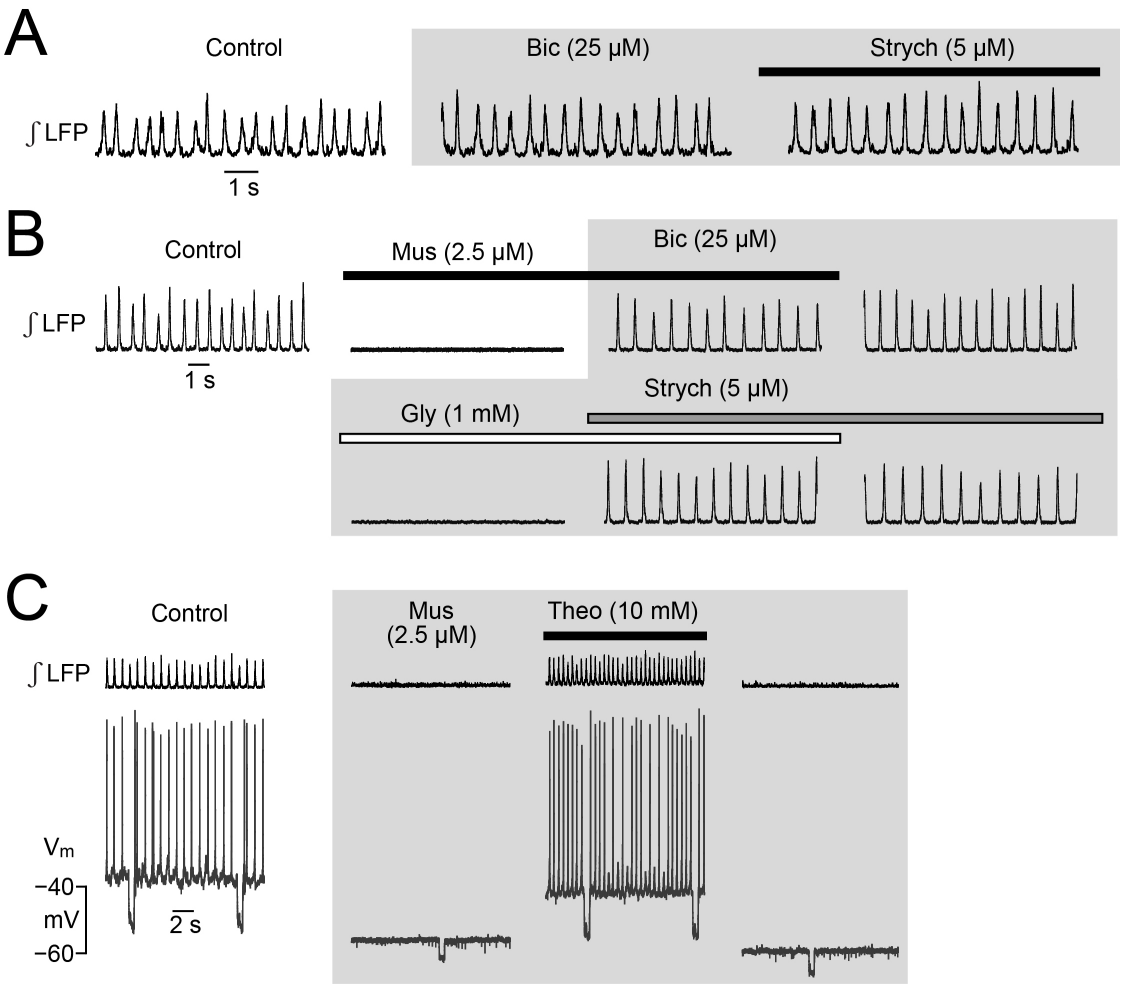

Fig. 1-6: $GABA_A$ and glycine (Gly) receptor (ant)agonist effects on LC activities in newborn rat slices. A, bath-application of the $GABA_A$ receptor blocker bicuculline (Bic) has no effect on LFP and even addition of the Gly receptor blocker strychnine (Strych) to this solution does not perturb rhythm. **B**, The neonatal rat LC has functional $GABA_A$ and Gly receptors as the $GABA_A$ receptor agonist muscimol (Mus) abolishes rhythm which is restored by adding Bic to the Mus-containing solution. Subsequent bath-application of Gly in Bic-containing solution also abolishes rhythm that is then reactivated by Strych. **C**, Blockade of LFP rhythm by bath-application of Mus is accompanied by a LC neuron hyperpolarization and a decrease of input resistance measured by repetitive injection of hyperpolarizing current pulses at 10 s interval. The effects are countered by addition of theophylline (Theo) to the Mus-containing superfusate. From (Panaitescu and Ballanyi, 2022).

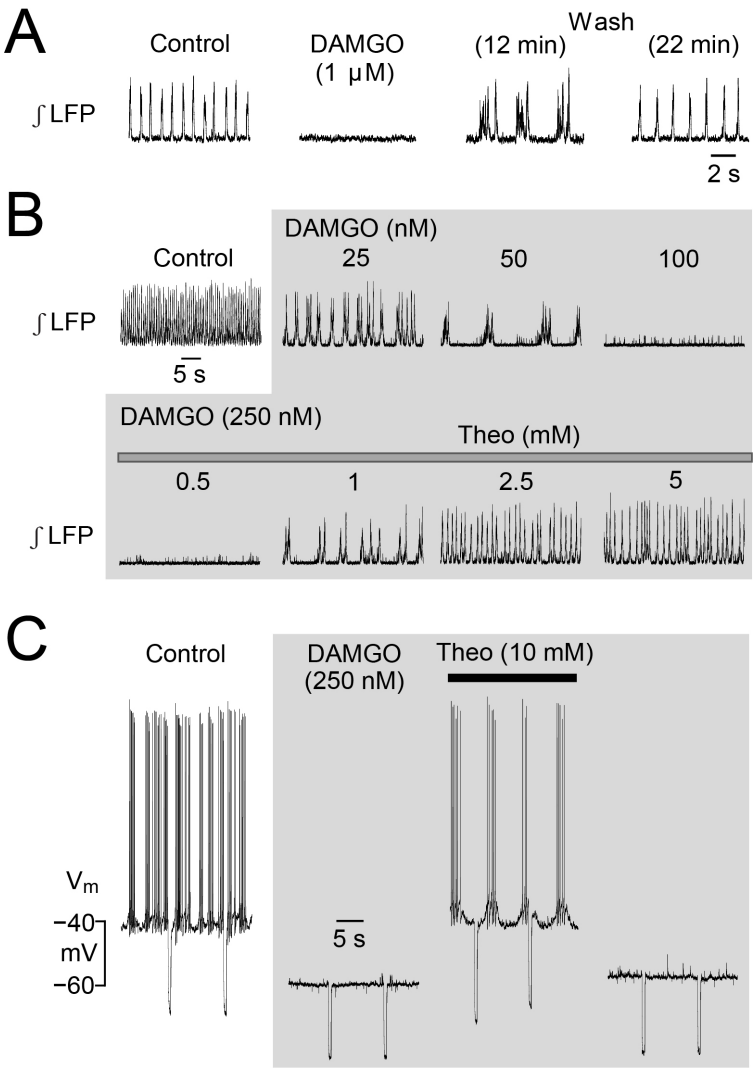

Fig. 1-7. Depressing opioid effects and stimulatory theophylline (Theo) action on LC activities in newborn rat slices. A, bath-application of 1 µM of the µR agonist [D-Ala^2,N-Me-Phe^4,Gly^5-ol]-enkephalin (DAMGO) abolishes LFP rhythm. Recovery to the normal pattern of rhythm 22 min after start of DAMGO washout is preceded by a period of occurrence of slower multipeak bursts. **B**, bath-application of increasing DAMGO doses transforms LFP pattern into multipeak bursts (at 25–50 nM) while rhythm is abolished at 250 nM. Rhythm recovers upon addition of 1 mM Theo to multipeak bursting whereas 5 mM Theo restores a normal pattern. **C**, DAMGO hyperpolarizes V_m and abolishes intracellular spiking whereas bath-application of Theo reverses the hyperpolarization and induces rhythmic bursting. Input resistance was measured by repetitive injection of hyperpolarizing current pulses at 10 s interval. **A** adapted with permission from (Rancic et al., 2018); **B**,**C** from (Panaitescu and Ballanyi, 2022).

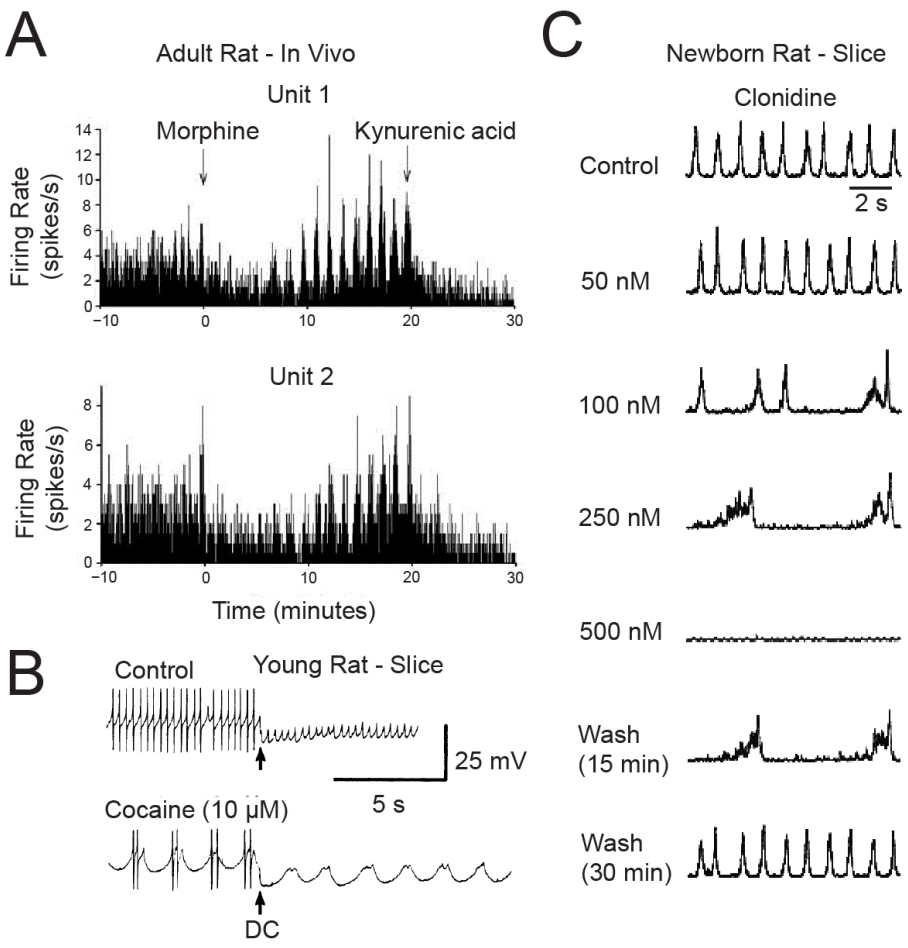

Fig. 1-8: µR- and α_2R-evoked LC discharge pattern transformations. A, in an adult rat in vivo intracerebroventricular application of the µ-opioid agonist morphine transforms asynchronous low-rate spiking of 2 extracellularly recorded LC neurons into slow, synchronous spike bursts. Subsequent kynurenic acid injection reverses this effect. **B**, in a slice from a young rat, cocaine enhances the amplitude and prolongs the duration of subthreshold oscillation leading to a change in the discharge from 1 to several spikes per event. **C,** in a newborn rat slice increases in the dose of bath-application of the a_2R agonist clonidine firstly slow LFP rhythm, then induce crescendo-like multipeak bursts followed by blockade of the LFP. Upon washout, multipeak bursts occur transiently. **A** adapted with permission from (Zhu and Zhou, 2005); **B** adapted with permission from (Williams and Marshall, 1987), copyright (1987) Society for Neuroscience; **C** from (Waselenchuk et al., 2022).

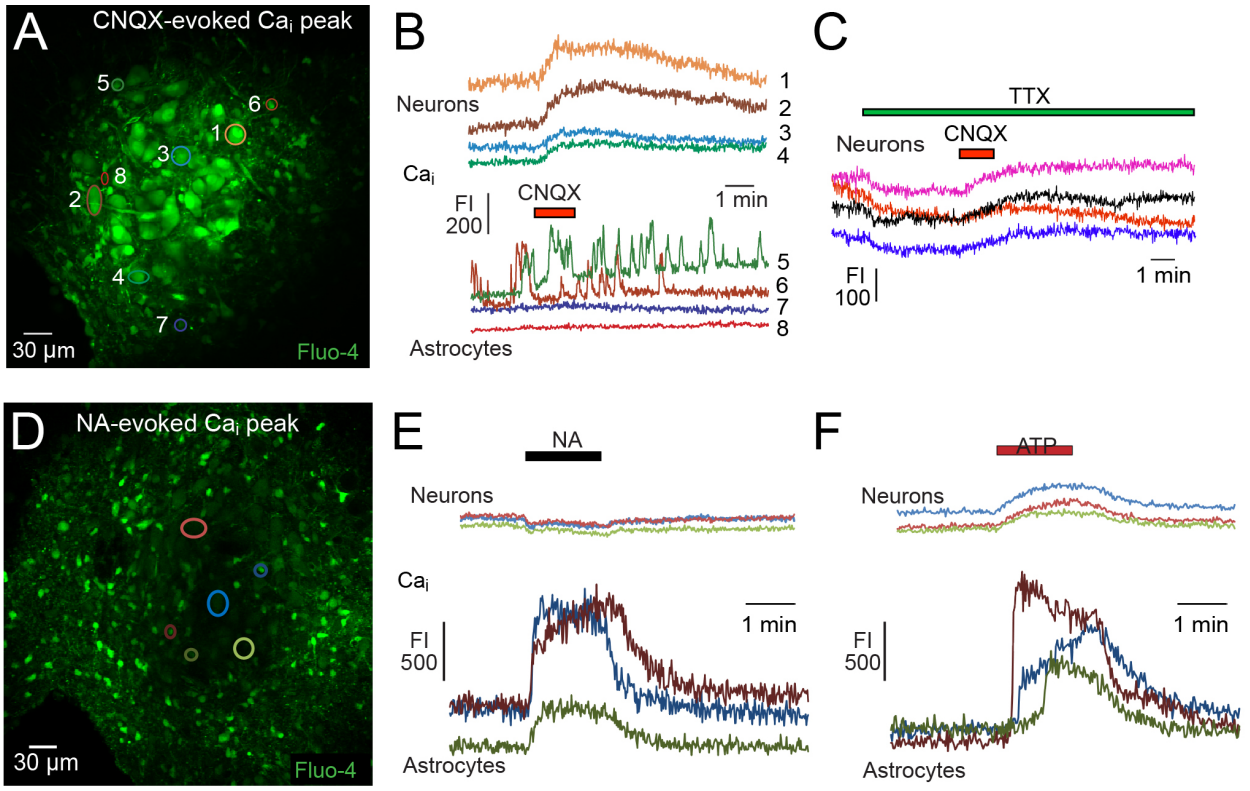

Fig. 1-9: Neuromodulator-evoked changes in the free cytosolic Ca^{2+} concentration (Ca_i) in the LC of newborn rat slices. A, fluorescence image (at the peak of the response to bath-applied CNQX) of LC cells bulk-loaded via focal pressure injection with the membrane-permeant form of the green fluorescent Ca^{2+} dye Fluo-4. The numbered colored shapes are regions of interest (ROIs) drawn offline via Fluoview software (FV10-ASW, version 03.01.01.09, Olympus, Markham, ON, Canada) around 4 neurons (#1–4) and 4 presumptive astrocytes (#5–8). **B**, CNQX-evoked Ca_i rises, indicated by an increase in Fluo-4 fluorescence intensity (FI), are similar in all 4 ROI-identified neurons whereas the 4 astrocytes labeled do not respond, however 2 cells show spontaneous Ca_i rises. **C**, in 4 neurons of a different slice, the CNQX-evoked Ca_i rise persists after preincubation in TTX which decreases Ca_i baseline. **D**, Fluo-4 image with ROIs from 3 neurons and 3 smaller astrocytes. **E**, Ca_i kinetics traces from cells in **D** plotted during bath-application of 25 µM NA. NA caused a decrease in neuronal Ca_i baseline, contrary to eliciting a concentric Ca_i wave firstly in peripheral and finally in LC astrocytes (see Video). **F**, Ca_i response of the same cells to bath-application of 100 µM adenosine-triphosphate (ATP). **A–C** Adapted with permission from (Rawal et al., 2019); **D–F** from (Waselenchuk et al., 2022).

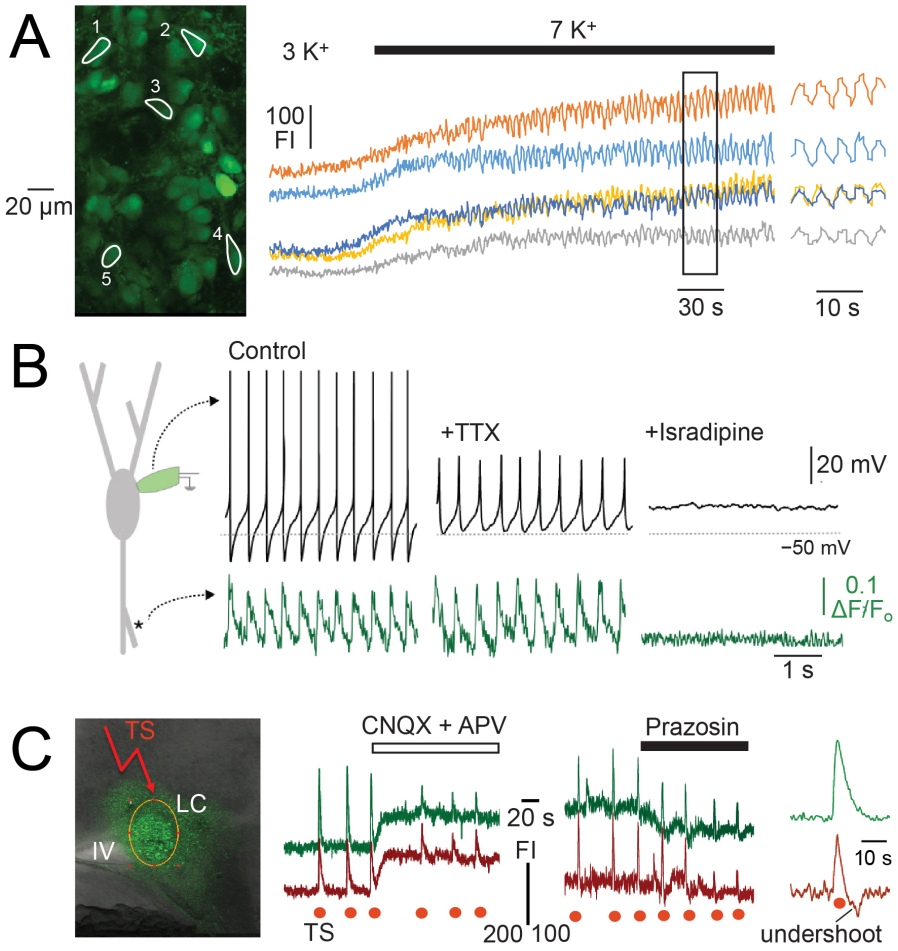

Fig. 1-10: Ca_i rises in LC neurons of newborn rat slices during single spikes, K^+-evoked LFP bursts and electrical stimulation. A, left, a fluorescence image of LC cells bulk loaded with Fluo-4 with ROI outlines drawn around 5 neurons. The middle trace shows that when superfusate K^+ is changed from physiological 3 mM K^+ to 7 mM, baseline FI increases and begins to rhythmically oscillate. These oscillations are shown at a magnified timescale on the right, revealing that they are synchronous. **B**, shows a schema of an LC neuron (**left**) during whole-cell V_m recording from the soma and synchronized dendritic Ca^{2+} line-scan imaging. Combined voltage (**upper**) and fluorescence (**lower**) traces show that under control conditions and during TTX application dendritic Ca^{2+} oscillations recorded up to 100 µm away from the soma are phase-locked to somatic spiking activity. L-type Ca^{2+} channel antagonist isradipine (1 µM) eliminated Ca^{2+} oscillations in the presence of TTX. **C**, shows the LC bulk loaded with Fluo-4 during repetitive electrical stimulation (TS) in an area next to the LC. This resulted in fluorescence increases in neurons (middle traces) that are apparently partly mediated by AMPAR/KAR and α_1R as they are partly blocked by CNQX and prazosin, respectively. The right traces exemplify that stimulation induced either an increase in FI followed by a return to baseline or FI increases followed by an undershoot below baseline. **A** adapted with permission from (Rawal et al., 2019); **B** adapted with permission from (Sanchez-Padilla et al., 2014); **C** from (Waselenchuk et al., 2022).

CHAPTER 2

Methods

All procedures for this project have previously been described in detail by our group (Kantor et al., 2012; Rancic et al., 2018; Rawal et al., 2019).

2.1. Preparations and Solutions

Experiments were performed on horizontal brain slices from postnatal day (P) 0 to 7 Sprague Dawley (CD1-001) rats of unknown sex (Charles River Laboratory Inc., Wilmington, MA, USA). All procedures for experiments were approved by the University of Alberta Animal Care and Use Committee (AUP-00000221) and in compliance with the guidelines of the Canadian Council for Animal Care and in accordance with the Society for Neuroscience's 'Policies on the Use of Animals and Humans in Neuroscience Research'.

Rats were first anesthetized with 2–3% isoflurane until disappearance of the paw withdrawal reflex. The brain was then isolated in room temperature 'standard' superfusate which contained (in mM): 120 NaCl, 3 KCl, 1.25 NaH_2PO_4, 26 $NaHCO_3$, 10 D-glucose, 1.2 $CaCl_2$, and 2 $MgSO_4$ and was gassed with carbogen (95% O_2, 5% CO_2) for tissue oxygenation and to adjust pH to 7.4. The ventral surface of the brain was then glued to a metal plate that was inserted into a vibratome (Leica VT1000S, Leica Microsystems, Richmond Hill, ON, Canada) containing continuously carbogenated room-temperature superfusate. After an initial cut to remove roughly the top third of the cortex, serial 400 µm slices were cut until the 4^{th} ventricle (4^{th} V) became visible. Depending on the size of the brain, 2–3 slices were then taken until the 4^{th} V began closing.

The latter LC-containing slices were first individually transferred to an acrylic recording chamber (Warner Instruments, Hamden, CT, USA), fixed with a platinum harp, and superfused with

standard solution kept at 28 °C via bath heater (Thermo-Haake DC10-V15/B, Sigma Aldrich, Canada). Flow rate was adjusted to 5 ml/min using a roller pump (Sci-Q 403-U/VM, Watson Marlow, Wilmington, MA, USA) and superfusate was removed distal to the slice by a vacuum-attached hypodermic needle. Slice positioning was done using a 2x objective (XLFluor-340, numerical aperture 0.14) connected to a multiphoton excitation (MPE) microscope (Olympus, Markham, ON, Canada) whereas LC cells were visualized under a 20x objective (XLUMPlanFL N, numerical aperture 1.0). After inspection under the 20x objective, the slice containing the largest LC aspect (by diameter) was selected for recording and the other ones stored for up to 3 h at room temperature on a net in a beaker filled with carbogenated superfusate.

2.2. Suction Electrode LFP Recording

Our group previously reported that the neonatal LC produces a stable LFP that can be recorded using large-tipped suction electrodes (Kantor et al., 2012; Rancic et al., 2018) contrary to microelectrodes. To obtain a suction electrode, a patch pipette was made from glass capillaries (GC-150TF-10; 1.5 mm outer Ø, 1.17 mm inner Ø, Harvard Apparatus) using a vertical puller (PC-10, Narishige International Inc., Amityville, NY, USA) and manually broken and beveled at a 45° angle with sandpaper (Ultra Fine 600 Grit, Norton-Saint Gobain, Worcester, Wa, USA) to an oval-shaped tip of 40-60 µm outer Ø. The pipette was placed in a UM-3C manipulator (Narishige International Inc., Amityville, NY, USA) for insertion into the superfusate. Gentle suction was then applied with a syringe (BD Diagnostics, Franklin Lakes, NJ, USA) to fill it. The electrode approached the slice at a ~45° angle until its opening was flat against the slice surface and ~5 mmHg suction was then applied to form a loose seal. The 'raw' LFP signal was amplified (x10k) and band-pass filtered (0.3–3 kHz) with an AM-Systems differential amplifier (Sequim,

WA, USA). In parallel, the signal was 'integrated' at a 50 ms time constant via an MA-821/RSP unit (CWE Inc., Ardmore, PA, USA) and both signals were sampled at 4 kHz using a PowerLab 8/35 data acquisition hardware device with LabChart 7 software (ADInstruments, Colorado Springs, CO, USA).

2.3. Population Ca_i Imaging

Population Ca_i imaging is used to indirectly visualize activity in neurons and/or glial cells in neural networks (Takahashi et al., 1999; Stosiek et al., 2003; Yuste et al., 2006). Our group has used this approach in neonatal brain slices to record neural network activity, e.g., in the inspiratory center (Ballanyi and Ruangkittisakul, 2009; Ruangkittisakul et al., 2009), hippocampal CA_3 area (Ruangkittisakul et al., 2015), and LC (Rawal et al., 2019). For this thesis project, LC cells were loaded with the membrane-permeant green fluorescent Ca^{2+} dye Fluo-4-AM (Invitrogen, Carlsbad, CA, USA). Specifically, 5 mM Fluo-4-AM, already dissolved in 20% DMSO + pluronic acid, was further diluted to 0.5 mM in superfusate. After backfilling with 3 µl of this dye solution, a glass patch pipette (see above) broken to a 5-10 µm tip diameter was positioned via an MP-285 micromanipulator (Sutter Instruments, Novato, CA, USA) above the LC. During visualization with an Olympus 20x objective, the pipette was inserted diagonally to a depth of 50–75 µm into the LC center after which dye was injected by applying 30–50 mmHg positive pressure. Once a circular region 400–600 µm in diameter was stained (within 10–20 min), the MPE system was used for imaging at a fixed depth 40–70 µm below the slice surface where LC cells were typically optimally filled and thus well visible. Fluorescence intensity (FI) was measured in a horizontal ('xy') image plane at 1.5x digital zoom and at an acquisition rate of 1.1 frames/s after exciting cytosolic Fluo-4 with Ti:Sa laser light pulses of 820 nm wavelength.

2.4. Immuno-histochemistry

LC neurons can be stained using the marker tyrosine hydroxylase (TH) while astrocytes can be identified by the marker S100β. TH is a well-established marker for identification of catecholamine-producing neurons, such as those comprising the LC, as it is the rate limiting enzyme in NA synthesis (Segal and Kuczenski, 1974; Nestler et al., 1990). In contrast, S100β expression is not exclusive to astrocytes and staining using this marker may also label ependymal cells, oligodendrocytes, the choroid plexus epithelium, vascular endothelial cells, lymphocytes, and some types of neurons (Steiner et al., 2007). Glial fibrillary acid protein (GFAP) is instead more selective for astrocytes (Steiner et al., 2007). In our hands, however, GFAP showed poor immunopositivity for LC astrocytes and failed to stain them. This may be due to our use of a neonatal model, as GFAP expression increases with age and is present in smaller amounts in the early postnatal period (Yoshida et al., 1996). In addition, the LC is located in the brainstem, and GFAP+ astrocytes are presumably scarce in the brainstem of both adult and neonatal brains (Taft et al., 2005). For these reasons, the present experiments used S100β despite its lower specificity.

Double staining with TH+S100β was performed on both LC aspects from one P0 and one P3 rat after isolation and chemical fixation by 24 h incubation in 4% paraformaldehyde in phosphate buffer (1:2 mixture of 0.1 M NaH_2PO_4 + 0.1 M Na_2HPO_4 in H_2O, pH 7.2). 400 µm thick horizontal slices were taken from each brain until the dorsal edge of each bilateral LC was within <1 mm after which 14–16 slices of 60 µm thickness were taken covering the entire dorsoventral LC extension. Slices were incubated overnight at 4 °C in monoclonal rabbit anti-TH (1:1000, Life Technologies, Camarillo, CA, USA) and mouse anti-S100β (1:1000, Sigma Aldrich, Oakville, ON, CA) antibodies in Tris-buffered saline (TBS) solution (0.9 % w/v NaCl plus 0.6 % w/v tris base,

sigma, pH 7.4) also containing 0.3 % Triton X-100. This was followed by 90 min incubation in secondary goat anti-rabbit Alexa 594 (1:500, Life Technologies, Camarillo, CA, USA) and goat anti-mouse Alexa 488 (1:1000, Jackson Immunoresearch Laboratories Inc, West Grove, PA, USA) also in TBS with Triton X-100. For cell identification, 4x-magnified transmitted light images at 1x optical zoom were first taken of all slices. Then, at an interval of 1 µm a z-stack of images spanning the entire depth of each of the 60 µm thin slices containing both LC aspects was taken at 1x optical zoom using the Olympus 20x objective and MPE system.

2.5. Pharmacology

The following agents (all from Sigma-Aldrich) were added to standard superfusate from stock solutions: NA (10 mM in H_2O), ATP (15 mM in H_2O), and t-ACPD (2.5 mM in H_2O). Importantly, at the end of each imaging experiment, 500 µM or 1 mM glutamate (1 M in H_2O) was bath-applied for 30 s to evoke a prominent Ca_i rise in neurons and most types of glial cells (Kim et al., 1994; Parpura et al., 1994; Zhou and Danbolt, 2014). This application served, on the one hand, to determine whether dimly fluorescent cells were not well stained or rather had a low Ca_i baseline. On the other hand, the glutamate-evoked FI rises could act as a reference point for Ca_i rises evoked by the other agents. Drugs were bath-applied by addition to superfusate and transported to the slice chamber via tubing at 5 ml/min. This produced a temporal delay of about 1 min between time of drug application and effect based on the perfusion rate and length of tubing supplying the chamber and was therefore compensated for during analysis.

2.6. Data Analysis

Ca_i imaging analysis was done using Olympus Fluoview software (FV10-ASW, version 03.01.01.09) and Microsoft Excel for Mac (version 15.38). For analysis of neuronal responses to NA, ATP, t-ACPD, and glutamate, regions of interest (ROIs) were first drawn around all neurons that responded to glutamate. The same ROIs were then applied for analysis of responses to the other agents to generate traces of FI over time and exported to Excel where traces were smoothened using 20-point averages for further quantitative analysis. Numbers of responding vs. non-responding neurons were then counted. For responding cells, percent change in FI was calculated using the formula 100 x $\Delta F/F0$ where ΔF is the difference between peak FI value during the drug effect and FI at baseline (F0, defined as FI at the time point immediately before the start of the effect). The same method for determining percent FI change in neurons was also used for astrocytes. In addition, the number of astrocytes responding to each neuromodulator was counted. For responding astrocytes, time of response onset (t_{onset}) was determined for each cell as time of maximum FI slope. To analyze distribution of responding astrocytes, their distance from the LC center was calculated using their x,y coordinates and the coordinate of a reference ROI placed at the LC center. The relationships between onset of astrocyte responses and their distance from LC centre were analyzed using coefficient of correlation to quantify the significance of the possible Ca_i wave triggered by NA and the other modulators.

LFP analysis was done using LabChart 7 software (ADInstruments). LFP rate, amplitude, baseline, and event duration were determined during 20–60 s of steady-state for control and drug effects. Specifically, LFP rate (Hz) was calculated using cycle count (i.e., number of LFP events) divided by duration (s). Amplitude was determined from averaged cyclic height, and baseline was

determined from averaged cyclic minimum (V). Cycle count, averaged cyclic height, and averaged cyclic minimum were measured using LabChart Data Pad/Cyclic Measurements function. Cycle or event detection was performed using respiration-airflow as a standard pre-set for the waveform detection setting, and minimum peak height was adjusted between 1–3 standard deviations for consistently reliable cycle detection. For fast LFP signals (e.g., during t-ACPD), the general-sine shape detection pre-set with standard deviation of 1 was used. Event duration was determined manually for detected events as the time between when the integrated signal left baseline to when it returned.

Astrocyte numbers and distribution: First, 60 μm z-stack recordings were converted to single xy-plane images by summating maximum intensity projections of each image in the stack using Fluoview software. Flattened images were then uploaded to Fiji ImageJ (version 2.1.0/1.53c) where the 'Split Channels' tool was used to generate separate greyscale images for the neuron (red) and astrocyte (green) channels. Next, the astrocyte image was modified using the 'Invert' and 'Enhance Contrast (0.5%)' functions to improve visualization of cells. Both neuron and astrocyte images were then overlaid with a 50 μm x 50 μm grid using the 'Grid' tool. All well-stained grid squares were categorized as 'LC' if they were >75% covered by neuron somata while others were categorized as 'periphery'. Grid squares touching the edge of each image were excluded from analysis. Total number of astrocyte somata present in the periphery and LC grids was counted using the 'Cell Counter' tool and this value was divided by the number of grid squares comprising that region to give a measurement of number of astrocyte somata/50 μm^2 for both the periphery and LC. Density values for the periphery and LC in each slice were then plotted against the slice depth to show trends in the dorsoventral direction. To determine the distribution of

astrocytes in a horizontal plane, one slice at the approximate depth typically used for Ca_i imaging was selected from each of 4 TH+S100β stained LC preparations. This was defined as the slice in which LC neuron somata were present as a large, approximately round, dense cluster near the lateral edge of an open 4th V. In these slices, the distance between a reference ROI placed at the centre of the LC and the x,y coordinate of every astrocyte somata was calculated using Microsoft Excel for Mac (version 15.38).

For Ca_i imaging and LFP data, n-values correspond to number of 400 μm slices where 1 slice comes from 1 animal. For immunohistochemical data, n-values correspond to number of 60 μm slices where all slices come from 4 LC aspects from a total of 2 animals. Values represent means ± SD. Significant values (non-significant (ns): $P>0.05$, *$P<0.05$, **$P<0.01$, ***$P<0.001$, ****$P<0.0001$) were assessed by paired two-tailed t tests, repeated measures one-way ANOVA with Dunnett's post-test, and two-way ANOVA with Tukey's post-test using Prism software (GraphPad Software Inc., La Jolla, CA, USA). Prism software was also used to determine statistically significant linear relationships between astrocyte distance from LC center and time of Ca_i rise onset using Pearson's correlation coefficient and associated P values. Trends in astrocyte density were determined using a quadratic nonlinear fit, also calculated with Prism software.

CHAPTER 3

Results

The results section deals with histological and functional aspects. Regarding histology, the distribution of LC neurons and astrocytes was first analysed in chemically fixed slices from our previous study that were immuno-histochemically labelled for TH and S100β, respectively (Rawal et al., 2019). The emphasis was on a section level approximately through the neuron soma area center in the dorsoventral axis close to the depth of slices aimed at for our previous electrophysiological and Ca_i imaging studies (Kantor et al., 2012; Rancic et al., 2018; Rawal et al., 2019, 2022) **(Figs. 3-1A$_1$,A$_2$)**. This serves to facilitate the understanding of the connectivity of cells at this level. The distribution of the immuno-labelled neurons and astrocytes was compared with that in acutely isolated living slices stained with the Ca^{2+}-sensitive fluorescent dye Fluo-4 in which the soma diameter of these cells was assumed to be ≥20 µm and ~10 µm, respectively (Swanson, 1976; Rawal et al., 2019). The major functional aspects of the results section handle the questions of whether neurons and astrocytes differ in their Ca_i responses to NA, ATP, t-ACPD, or glutamate, and if there are distinct responses to these agents in subpopulations of each cell type indicating a modular LC organization in newborns (Waselenchuk and Ballanyi, 2022). In addition, the LFP was recorded during application of these agents for improved understanding of the neuronal Ca_i dynamics.

3.1. Distribution of Immuno-histochemically Labelled Neurons and Astrocytes

The three-dimensional distribution of TH-labelled neurons and S100β-labelled astrocytes was analysed in sequential confocal image stacks of 60 µm thin slices from both LC aspects of one P0 and one P3 rat. As evident from the schema in **Fig. 3-1A$_1$** and the transmitted light image in **Fig. 3-1A$_2$**, the LC, defined by the distribution of neuron somata, is located close to the 4th V. In the dorsoventral axis, the LC extended by ~850 µm. Around the midpoint of this axis, the horizontal

neuron soma area had a close-to-circular shape spanning 300–400 µm from anterior to posterior and 250–300 µm in the medio-lateral direction as shown for 3 TH-labelled LCs in **Fig. 3-1A$_{3\text{-}5}$**. The similarly shaped central neuron soma area of the remaining LC is illustrated in **Fig. 3-1B$_3$**, whereas **Fig. 3-1B$_{1,2}$** and **Fig. 3-1B$_{4,5}$** exemplify its more dorsal and ventral shapes, respectively. These images indicate that the dorsal LC neuron soma area is narrower and band- or spindle-shaped with neurons apparently tightly wrapped around the border of the 4th V. In contrast, an approximately circular soma area shape is maintained toward the ventral LC pole, yet with a steady decrease in diameter and increased variability. While neuron somata are located very close to each other around the LC center, their density decreases towards both poles. As evident from the images in **Fig. 3-1A$_{3\text{-}5}$** and **Fig. 3-1B**, neuronal processes spread away from the soma area in irregular fashion at the different LC levels. Close to the LC center, these 'pericoerulear' neuronal processes are prominent in the rostromedial direction, as opposed to their lower distribution in the caudolateral direction.

The double-stained slices further revealed that, at all depths, the LC neuron soma area is surrounded by a network of S100β-positive astrocytes **(Fig. 3-1C,D)**. Moreover, astrocyte somata appear more densely distributed in the peripheral and pericoerulear regions than in the LC soma area **(Fig. 3-1C,D)**. As an unexpected finding described in more detail below, cells in an area next to the 4th V were also labelled for S100β **(Fig. 3-1C$_{1\text{-}3}$)**, and are likely ependymal cells or possibly tanycytes (Felten et al., 1981; Steiner et al., 2007; Del Bigio, 2010; Feng et al., 2011). Due to their uncertain identity, these cells will hereafter be referred to as ependymal for the purpose of consistency.

As revealed at higher magnification of the images taken around the level used for electrophysiology and Ca_i imaging of the LC, the pericoerulear region was characterized by numerous TH-positive fibers that extended preferentially rostromedially often >150 μm beyond the soma area **(Figs. 3-2A,B)**. In this region, astrocyte somata appeared to be more densely distributed than within the neuron soma area **(Fig. 3-2C)**. Additionally, many of these surrounding astrocytes extend processes that seem to meet with a thick layer of ependymal cells lining the 4^{th} V at this depth. It is also possible that the latter cells send processes towards the astrocytes, or both do so **(Fig. 3-2D$_1$)**. These ependymal cells formed several layers in the dorsal and central LC aspects **(Fig. 3-2D$_2$)**. Towards the ventral pole, the layers thinned and eventually disappeared with astrocyte somata instead being present directly next to the (closed) ventricle **(Fig. 3-2D$_3$)**.

Configuration of S100β-positive astrocyte somata also showed differences across the dorsoventral axis. Specifically, density was similar between the LC neuron soma area and surrounding regions in slices taken from the most dorsal and ventral aspects of the LC while it differed in sections closer to its centre **(Fig. 3-3A$_1$)**. Mean astrocyte density was also greater in both the neuron somata area and surrounding regions in more ventral slices compared to dorsal in all preparations **(Fig. 3-3A$_1$)**. Despite differences between dorsal and ventral aspects, though, mean astrocyte density within the LC neuron soma area was still significantly lower than the surroundings in every preparation when values were averaged across all depths (n = 4 preparations, 2 animals; $P = 0.0002$, $P < 0.0001$, $P = 0.0031$, $P = 0.0010$) **(Fig. 3-3A$_2$)**.

Individual LC-containing slices from the typical Ca_i imaging depth further showed that astrocyte somata distribution follows a gradient in the horizontal plane: few astrocyte cell bodies are present

within the centre of the LC neuron soma area while at its outer rim and in the pericoerulear region there is a steep increase which remains high in the surroundings until the outer edge of the image and the ventricle are reached where numbers decrease again **(Fig. 3-3B$_1$,C$_1$)**.

3.2. Distribution of Fluo-4 Labelled Neurons and Astrocytes

For a comparison of the findings with the immuno-histochemically labelled slices, distribution of neurons and astrocytes was analysed in 6 acutely isolated 400 µm thick horizontal slices that were sectioned with the aim of exposing the dorsoventral LC center on the upper surface for electrophysiological recording and/or Ca_i imaging. In standard superfusate, an almost circular area covering, on average, an area of 32,000 µm^2 indicated the region of dimly fluorescent LC neuron somata with a diameter of mostly ≥20 µm whereas very few cells with a soma diameter ~10 µm were seen within the LC and surrounding areas of the slice **(Fig. 3-3B$_2$,B$_3$)**. When glutamate was applied to excite both neurons and astrocytes, though, FI increased in neurons and many small cells surrounding the soma area became visible due to a notable FI increase. Still, even at the peak of the glutamate response, very few small cells were visible within the neuron soma area **(Fig. 3-3B$_3$)**.

Analysis of the distribution of astrocytes at the peak of the glutamate response in the 6 slices verified that the density of small cell somata located in the inner 50 µm of the neuron soma area center averaged 1.11 ± 0.44 somata/50 µm^2, but steadily increased toward the LC rim and middle of the pericoerulear region where density peaked at 100–125 µm distant from the LC centre **(Fig. 3-3C$_2$)**. Note that the apparent decrease in astrocyte numbers between the outer pericoerulear region and the LC periphery in the graph of **(Fig. 3-3C$_2$)** is due to the fact that, on average, less

cells were stained in response to the single focal Fluo-4-AM injection into the LC center. Still, both Fluo-4 and S100β analyses indicate that the density of astrocyte somata is notably lower in the LC neuron soma area compared to the pericoerulear region of neuronal processes and the LC periphery. As a further important observation, Fluo-4 also stained ependymal cells well in a separate subset of slices containing the corresponding area next to the 4th V (not shown).

3.3. Analysis of LC Properties with Combined LFP and Population Ca_i Imaging

As outlined in the Introduction **(1.3.5)**, Ca_i typically shows a rise in neural networks during excitatory activity of neurons (involving Ca^{2+} entry through ligand-gated cation channels and voltage-gated Ca^{2+} channels combined with endoplasmic reticulum release) and astrocytes (primarily through Ca^{2+} release from endoplasmic reticulum in response to metabotropic receptor activation). Accordingly, combined LFP recording and Ca_i population imaging can provide novel information about spatiotemporal activities in neural networks (Kerekes et al., 2014). Our group has already established use of this approach in horizontal LC slices from newborn rats (Kantor et al., 2012; Rawal et al., 2019; Waselenchuk and Ballanyi, 2022).

In most experiments for this thesis project, Ca_i imaging was done from superficial LC cells in one half of a given slice whereas the LFP was recorded from the contralateral LC aspect. Both LC aspects are not coupled and thus do not show correlated activity (Kantor et al., 2012; Rancic et al., 2018). However, occurrence of a rhythm on one side served as indication that both networks in the slice likely exhibited normal in vitro activity. Altogether, LFP recordings from 11 slices were analysed while Ca_i imaging was also performed on 6 of these 11 slices from which a total of 234 neurons and 1410 astrocytes were analysed.

At the end of each experiment, exposure of the slice to 500 μM or 1 mM bath-applied glutamate for 30 s evoked a prominent Ca_i rise in both LC neurons and astrocytes **(Figs 3-3B$_2$,B$_3$,3-4A)**. This served as a reference for the relative extent of Ca_i changes in response to other agents that were tested. As described above, FI in astrocytes that were visible in control superfusate increased notably and 200–700% more astrocyte somata became visible in which Ca_i baseline (and thus FI) was too low under resting conditions **(Figs. 3-3B$_2$,B$_3$,3-4A)**. In contrast, somata of most neurons were already seen in control solution and FI increased on average less during glutamate compared to astrocytes (138.04 ± 24.99% of control, $P < 0.0001$ vs. 201.28 ± 19.78% of control, $P < 0.0001$, respectively) **(Fig. 3-4A)**. Importantly, using our imaging protocol, Fluo-4 staining could only clearly be observed in the somata but not in most processes of both neurons and astrocytes. As a result, Ca_i imaging of neuronal activity in the pericoerulear area where most synaptic interactions occur was not possible (Aston-Jones et al., 1991; Ivanov and Aston-Jones, 1995; Ishimatsu and Williams, 1996).

In all LFP recordings (n = 11), the assumption that glutamate had a major excitatory effect on the LC during such application was confirmed. Under control conditions, a bell-shaped signal was recorded with an average frequency of 1.24 ± 0.34 Hz and duration of 324.84 ± 145.51 ms **(Fig. 3-4B)**. During 500 μM or 1 mM glutamate, rhythm was momentarily accelerated within seconds of action before a brief burst of tonic activity was evoked (also evident as an increased baseline of the integrated LFP signal) followed by a silent period lasting typically 4–5 min **(Fig. 3-4C)**. In every case, rhythm returned within <15 min of washout indicating that the network remained viable. Specific features of the glutamate-evoked LFP changes prior to rhythm blockade were not analyzed as in almost every case the period of transformed/tonic activity lasted less than 20 s.

In control superfusate, Ca_i baseline in all neurons did not show rhythmic oscillations similar to findings in our previous studies (Kantor et al., 2012; Rawal et al., 2019). This indicates that phase-locked discharge of single action potentials due to synchronous STOs occurring at a rate of ~1 Hz does not notably elevate Ca_i in neuronal somata where ROIs were positioned for the current analyses. There were also no spontaneous non-rhythmic rises in Ca_i baseline, contrary to such events in a small subpopulation of presumptive astrocytes. Specifically, random FI increases of >100% that lasted ~10 s were observed during 1 min control recordings in ~1% of astrocytes.

3.4. Response of the LC Network to Autocrine NA Elevation

The main functional aspect of this thesis deals with characterizing the response of the neonatal rat LC in an acutely isolated horizontal slice to a uniform increase in extracellular NA. This is because a sustained increase in the rate of tonic spiking in subsets of LC neurons may elevate spontaneous NA release from proximal axon collaterals located inside/surrounding the LC that can then act on nearby cells to tune network activity (Cedarbaum and Aghajanian, 1978; Baral et al., 2022). Effects of such an 'autocrine' NA rise within the LC are partly mimicked by bath-application of NA. Preliminary findings by Drs. Araya Ruangkittisakul and Bijal Rawal from our group indicated that 25 µM bath-applied NA (for 90 s) slightly depresses LFP rhythm, likely caused by a modest hyperpolarization of LC neurons as indirectly indicated by a small decrease in Ca_i baseline. In contrast, astrocytes respond with an increase in Ca_i starting in those outside the LC followed by a 'concentric' Ca_i wave that propagates towards the LC centre. Further experiments from myself showed very similar effects which were analysed here as described in the following.

Upon 90 s bath-application of 25 µM NA, in 5 of 11 slices, LFP rate was blocked within ~1 min of appearance of the agent in the recording chamber. In the remaining 6 slices, some showed a trend in which the rhythm was transformed to longer events with the occurrence of a multi-peak pattern which persisted during washout, but this effect was not significant ($P = 0.3052$) **(Fig. 3-5A)**. Specifically, in all 11 slices, LFP frequency during NA decreased from 1.24 ± 0.34 Hz to 0.37 ± 0.51 Hz ($P < 0.0001$) **(Fig. 3-5B)**. While baseline of the integrated LFP signal was not affected by NA ($P = 0.7015$), amplitude decreased to 37.30 ± 40.31% of control ($P = 0.0004$) **(Fig. 3-5B)**. In parallel with overall depression of the LFP, FI was attenuated by NA in 70.65 ± 7.33% of glutamate-responding neurons by 15.80 ± 4.33% ($P = 0.0005$) as indication of a fall of Ca_i baseline whereas remaining neurons did not show a Ca_i response **(Fig. 3-5C)**. FI traces for responding neurons in each slice revealed an initial sharp FI decline lasting <45 s followed by a sustained but more moderate decrease lasting an additional 90–120 s after which there was a gradual recovery to baseline **(Fig. 3-5C$_3$)**. Within 5 s of the NA-evoked neuronal Ca_i baseline decrease, FI increased quickly in the vast majority of astrocytes in Fluo-4-stained areas surrounding the LC followed by a concentric Ca_i wave that approached the pericoerulear region **(Fig. 3-5C, see supplementary video)**. Lastly, 0–6 astrocytes showed a Ca_i rise in the central portion of the LC neuron soma area **(Fig. 3-5C)**. Altogether, 75.91 ± 4.92% of glutamate-responding astrocytes also responded to NA with an average FI increase of 141.79 ± 23.89% ($P < 0.0001$) **(Fig. 3-5C)**. Analysis of all NA-responding astrocytes further revealed a strong correlation between t_{onset} vs. distance from the LC centre ($R^2 = 0.90$, $P < 0.0001$), confirming that a Ca_i wave begins peripheral to the nucleus and progresses towards its centre from all directions **(Fig. 3-5D)**. This effect was independent of the order in which NA was applied (i.e., if other pharmacological

treatments were applied and washed prior or NA was applied several times) and could occur even if NA was applied after several hours of recording.

3.5. Response of the LC network to ATP and t-ACPD

As above described, only 71% of neurons and 76% of astrocytes that responded to glutamate also showed a decrease or increase, respectively, of Ca_i baseline during NA application. This may indicate a non-uniform distribution of neurotransmitter receptors on both cell types. To explore the possibility of modular LC cell responses, the effects on LFP and Ca_i were also analysed during bath-application of 100 µM ATP (90 s) or 25 µM t-ACPD (90 s). These agents were chosen as they can have ionotropic and/or metabotropic effects on the excitability and Ca_i in neurons and/or astrocytes (Ruangkittisakul et al., 2009; Sun et al., 2013; Verkhratsky and Parpura, 2014; Bazargani and Attwell, 2016; Rajani et al., 2018). Furthermore, it was investigated whether they are also capable of evoking a concentric Ca_i wave in astrocytes similar to NA.

Both ATP and t-ACPD had effects on the LFP pattern in the 11 slices analysed **(Fig. 3-6A)**. ATP did not have significant effects on LFP frequency (1.80 ± 0.97 Hz vs. 1.25 ± 0.34 Hz in control, P = 0.1371), or single event duration (366.50 ± 14.00 ms vs. 324.84 ± 145.51 ms in control, P = 0.6733), while it did significantly reduce event amplitude (76.14 ± 15.68% of control, P = 0.0010) and increase baseline of the integrated signal (105.28 ± 6.04% of control, P = 0.) **(Fig. 3-6B)**. In contrast, t-ACPD significantly accelerated LFP rate (3.65 ± 0.73 Hz vs. 1.25 ± 0.34 Hz in control, P < 0.0001) and increased the baseline of the integrated signal (111.5 ± 13.23% of control, P = 0.0300) without significantly altering single event duration (215.03 ± 48.57 ms vs. 324.84 ± 145.51 ms in control, P = 0.0677), or amplitude (89.96 ± 22.33% of control, P = 0.2764) **(Fig. 3-6B)**.

Ca_i in neurons and astrocytes increased in response to both modulators, with the neuronal response being more moderate **(Figs. 3-6C,D)**. Specifically, 86.29 ± 12.27% and 84.57 ± 13.10% of neurons that responded to glutamate also increased their FI by 23.24 ± 7.35% and 23.95 ± 6.46% during ATP ($P = 0.0010$) and t-ACPD ($P = 0.0005$), respectively, and kinetics traces of FI in neurons show the rise and recovery of Ca_i in response to ATP and t-ACPD were gradual **(Figs. 3-6C,D)**. In astrocytes, the ATP response was similar to NA such that most responding cells peaked within seconds of the neuronal response, increasing FI by 132.15 ± 16.30% ($P < 0.0001$) **(Fig. 3-6C)**. The t-ACPD astrocyte response differed, with responding cells instead flashing up briefly, increasing FI by 144.65 ± 24.78% ($P < 0.0001$), at different timepoints throughout the neuronal response **(Fig. 3-6D)**. This cell type also showed a large difference in the relative amount of their population responding to ATP vs. t-ACPD: 71.10 ± 9.05% of all glutamate-responding astrocytes responded to ATP while only 38.96 ± 8.52% responded to t-ACPD. Moreover, correlation analyses of astrocyte t_{onset} vs. distance from LC centre yielded a significant value for ATP ($R^2 = 0.7033$, $P = 0.0024$), but not t-ACPD ($R^2 = 0.2535$, $P = 0.1379$) indicating that ATP evoked a concentric Ca_i wave like NA, while t-ACPD did not **(Fig. 3-6C_4,D_4, supplementary videos)**.

Further analysis of neurons and astrocyte response patterns unravelled that subpopulations of each cell type responded specifically to either NA, ATP, t-ACPD, or a combination of the three when compared to their glutamate response. In the 6 analysed slices, the majority of neurons responded to NA, ATP, and t-ACPD (68.98 ± 8.35%) **(Fig. 3-7A_1)** while most astrocytes responded to only NA and ATP (30.19 ± 1.72%) **(Fig. 3-7A_2)**. Remaining neurons could be grouped based on their responses as follows: NA only, 0%; ATP only 3.14 ± 3.98%; t-ACPD only, 1.81 ± 2.68%; NA and t-ACPD, 0.64 ± 1.57%; NA and ATP, 1.03 ± 1.64%; ATP and t-ACPD, 13.14 ± 9.51%. A total of

11.25 ± 11.69% of neurons also responded to glutamate but no other modulators. Using the same criteria, additional responding astrocytes were grouped as follows: NA only, 14.18 ± 7.84%; ATP only, 16.67 ± 5.81%; t-ACPD only, 4.94 ± 1.27%, NA and t-ACPD, 9.77 ± 4.15%; ATP and t-ACPD, 2.48 ± 1.34%; NA, ATP, and t-ACPD, 21.77 ± 8.22% **(Fig. 3-7A)**. It was also checked whether cells responding to these modulators were preferentially located anteromedially, anterolaterally, posteromedially, or posterolaterally to determine a possible topographic organization. More ATP-responding astrocytes were located in the anteromedial compared to anterolateral quadrant (P = 0.0091), but no other significant spatial response patterns occurred **(Figs. 3-7B,C)**.

3.6 Ca_i Imaging of Ependymal Cells

In 5 slices used for Ca_i imaging (1 from this project, 4 from separate experiments done by Dr. Rawal) a multilayer of ependymal cells was also well loaded with Fluo-4 and visible at the edge of the 4th V. No quantitative analysis of their responses to modulators was performed, however it was observed that FI increased in (parts of) this cell layer in 4 slices during NA, 5 slices during ATP, and 1 slice during t-ACPD. Glutamate was also tested in 3 of these 5 slices, and there was no apparent response in any case.

3.7 Figures and Legends

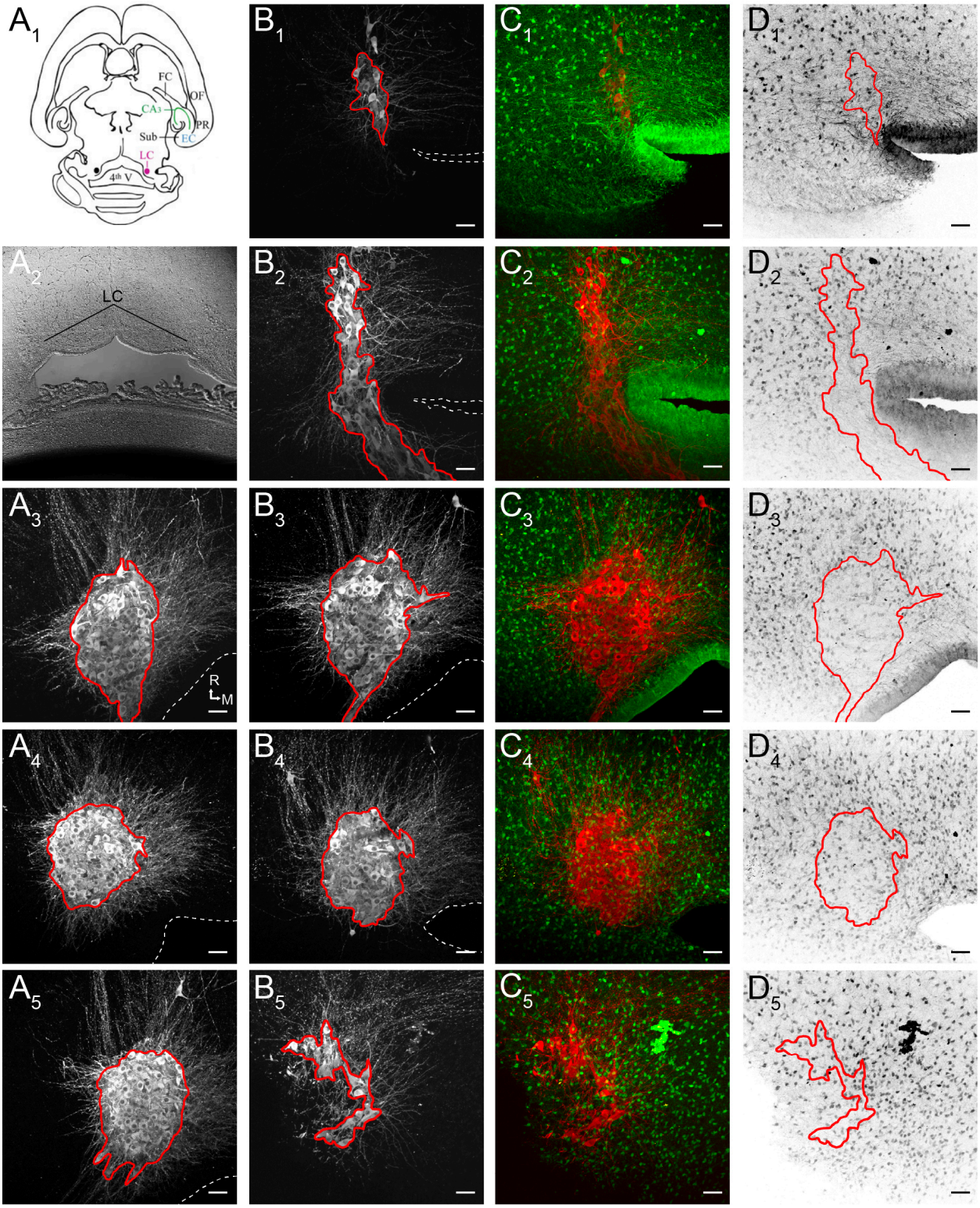

Fig. 3-1: Anatomy of the neonatal rat locus coeruleus (LC). A_1, schema of a horizontal brain slice at a depth typically used by our group for electrophysiological recording and cytosolic Ca^{2+} (Ca_i) imaging of the LC, which is a cluster of cells next to the lateral edge of the 4th ventricle (4th V). **A_2**, transmitted light image of a 60 µm thick chemically fixed horizontal brain slice at the same depth from a P3 rat to be used for double immuno-histochemical staining with the markers tyrosine hydroxylase (TH, red) and S100β (green). Based on the shape of the 4th V (white dashed lines in **A** and **B**), a slice at this depth is expected to contain the largest horizontal LC neuron soma area extension. **A_3–A_5**, summated 60 µm thin z-stack fluorescence images of TH-stained neurons at the approximate depth used for recording and imaging in 3 LC preparations from 2 rats. **B**, summated 60 µm z stack fluorescence images of TH-stained neurons from a separate preparation organized by dorsoventral depth. **B_1** and **B_2** show dorsal LC aspects, **B_3** is from the LC center, whereas **B_4** and **B_5** show ventral aspects. **C**, shows the same images as **B** with both TH-stained neuron (in red) and S100β-stained astrocyte (in green) fluorescence channels. **D**, shows the same image set again with only astrocyte fluorescence channel that has been inverted such that they appear as dark spots against a light background. Red outlines indicate the border of the LC soma area. R, rostral; M, medial. Rostral-caudal and medial-lateral axes in **A_3** the same in **A_4–D_5**. Scale bars all 50 µm.

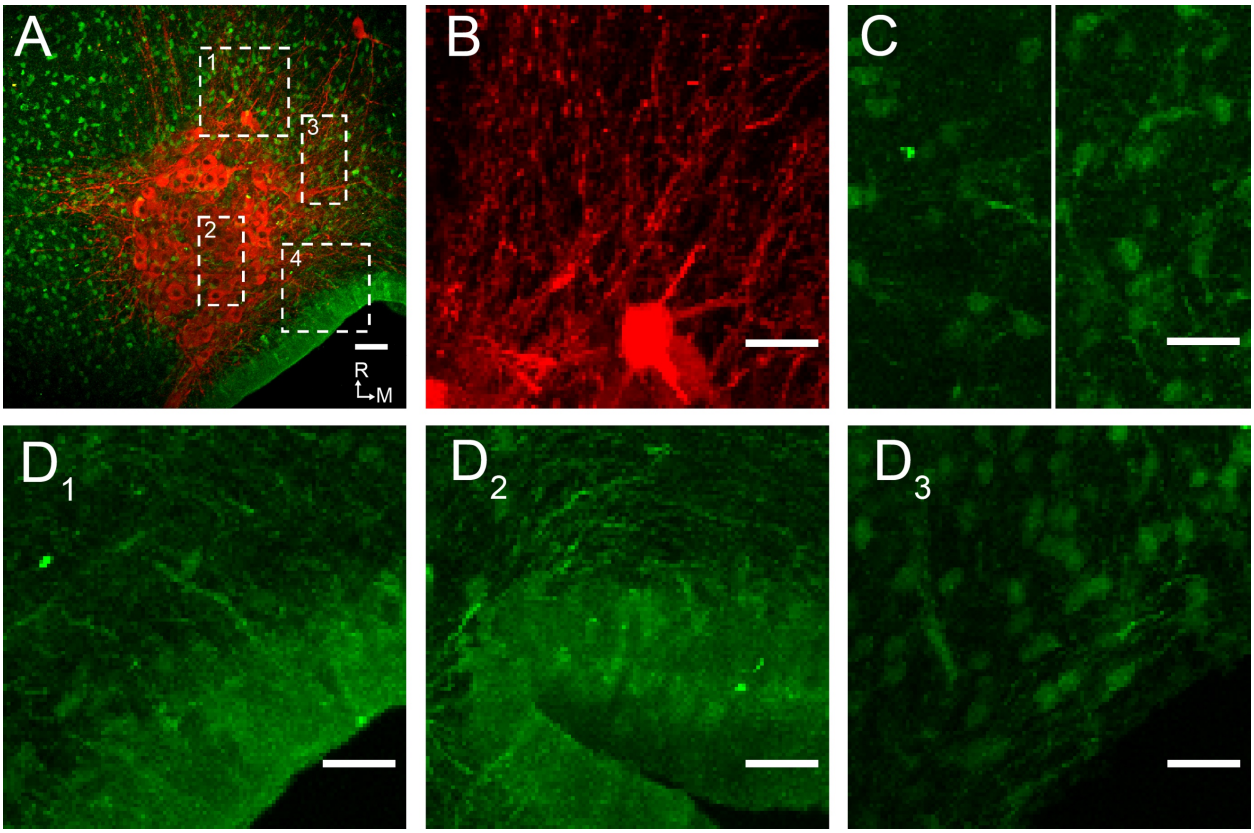

Fig. 3-2: Anatomical features of the neonatal rat LC and surrounding areas at the dorsoventral nucleus centre. A, same image as in **Fig. 3-1C**. Dashed boxes (1–4) indicate areas shown in **B**–**D**. **B**, shows only the red fluorescence channel for the area outlined by box 1 in **A**, indicating dense, TH-positive fibers emerging from the LC soma area to comprise the pericoerulear region. **C**, shows only the green fluorescence channel for the areas outlined by boxes 2 (left) and 3 (right) in **A**, indicating a difference in astrocyte somata density in the LC neuron soma area (left) compared to the pericoerulear region (right). **D_1**, shows box 4 from **A** indicating that at this depth, there is a thick layer of ependymal cells (possibly tanycytes) at the edge of the 4th V which appear to make connections with neighboring astrocytes (or vice versa). **D_2**, shows the edge of the ventricle in a more dorsal slice, where these cells are also present, while **D_3** shows the 4th V bottom edge from a ventral slice where they are not. R, rostral; M, medial. Rostral-caudal and medial-lateral axes in **A** the same in **B**–**D**. Scale bar in **A** 50 µm, all others 25 µm.

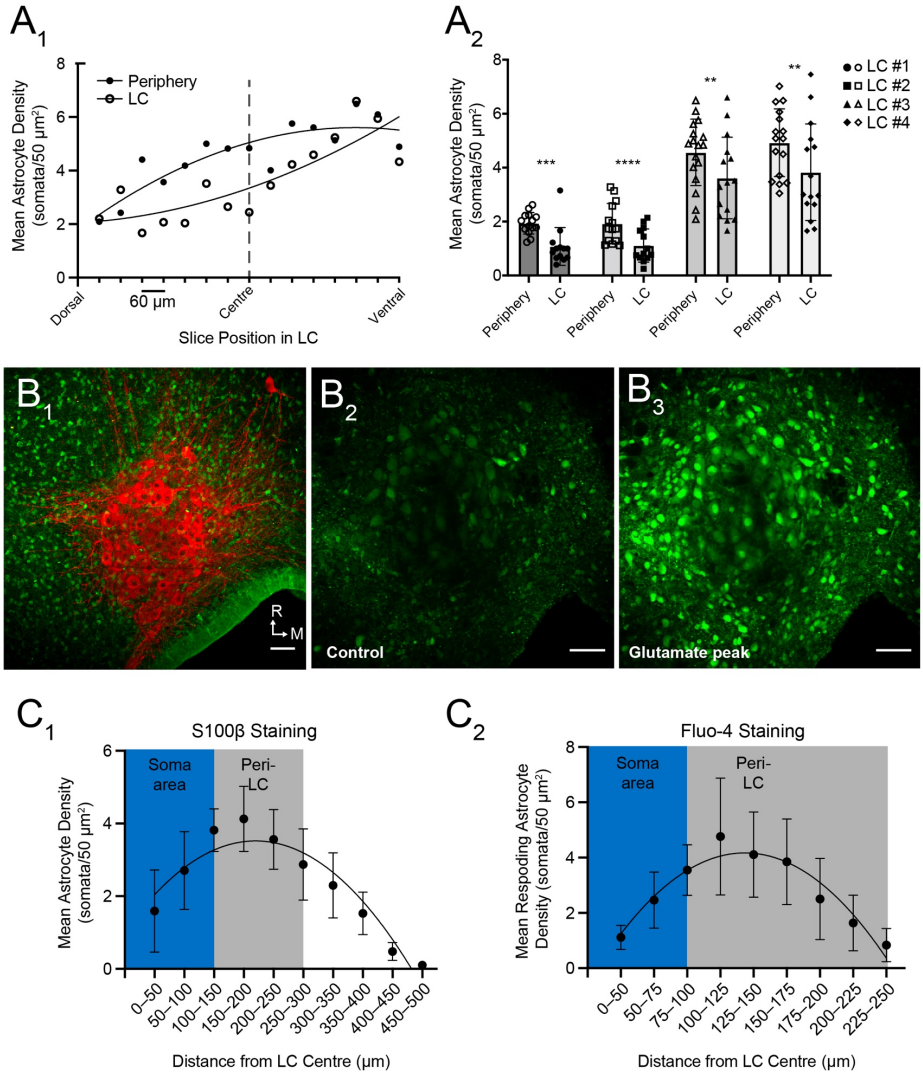

Fig. 3-3: Three-dimensional distribution of LC astrocytes. A1, trends for astrocyte somata density in the dorsoventral plane. Astrocyte somata density values for the LC neuron soma area and periphery in serial 60 µm thin z-stack horizontal slices taken from the dorsal to ventral edge of one TH+S100β-labelled LC indicates that, around the centre of the nucleus, astrocyte density is greater in the periphery compared to within the LC, while density in both regions increases towards the ventral pole. **A2**, despite variation in the dorsoventral axis, averaging astrocyte density across slices from all depths reveals significantly higher density in the periphery compared to the LC neuron soma area in all 4 TH+S100β labelled preparations from 2 animals. **B1**, same slice as in **Figs. 3-1B3,3-2B** highlighting this time the scarcity of astrocyte cell bodies (green) within the neuron soma area (red) at this level. **B2**, 400 µm thick living slice from a similar depth that has been bulk-loaded with the Ca^{2+} sensitive green-fluorescent dye Fluo-4-AM via pressure-injection. Image depicts the slice under baseline conditions in standard superfusate during which neurons are visible and identifiable due to their large soma size, whereas fewer smaller cells, presumably astrocytes, are also apparent. **B3**, peak response of the same slice to 1 mM glutamate applied for

30 s. Both neurons and presumptive astrocytes respond with a large increase in fluorescence intensity (FI), revealing many astrocytes in the periphery and more within the neuron soma area. **C_1**, in the horizontal plane, S100β-labelled astrocyte somata are most densely packed in the outer rim of the LC and proximal pericoerulear area. Values represent average density vs. distance from a reference point placed in the soma area centre in 4 slices from 2 animals at an approximate depth used for Ca_i imaging. Average LC neuron soma area diameter was ~300 µm, while the pericoerulear region extended ~150 µm in some directions. Note that the 4^{th} V is ~250 µm from the centre of the LC at this depth, contributing to the reduction in astrocyte density beyond this distance. **C_2**, shows that a similar trend is observed for glutamate-responding Fluo-4 loaded astrocytes in 6 slices from 6 animals. Average LC neuron soma area diameter was ~200 µm in these slices. As the pericoerulear region cannot be visualized with Fluo-4 staining, it was assumed to extend to the same distance as in TH+S100β-labelled slices. The reduction in astrocyte density at greater distances in this case is likely attributable to poor dye-loading distal from the single focal injection site. All trendlines depict quadratic nonlinear fits. Error bars represent SD. Significant values (**P < 0.01, ***P < 0.001, ****P < 0.0001). R, rostral; M, medial. Rostral-caudal and medial-lateral axes in **B_1** the same in **B_2** and **B_3** Scale bars are all 50 µm.

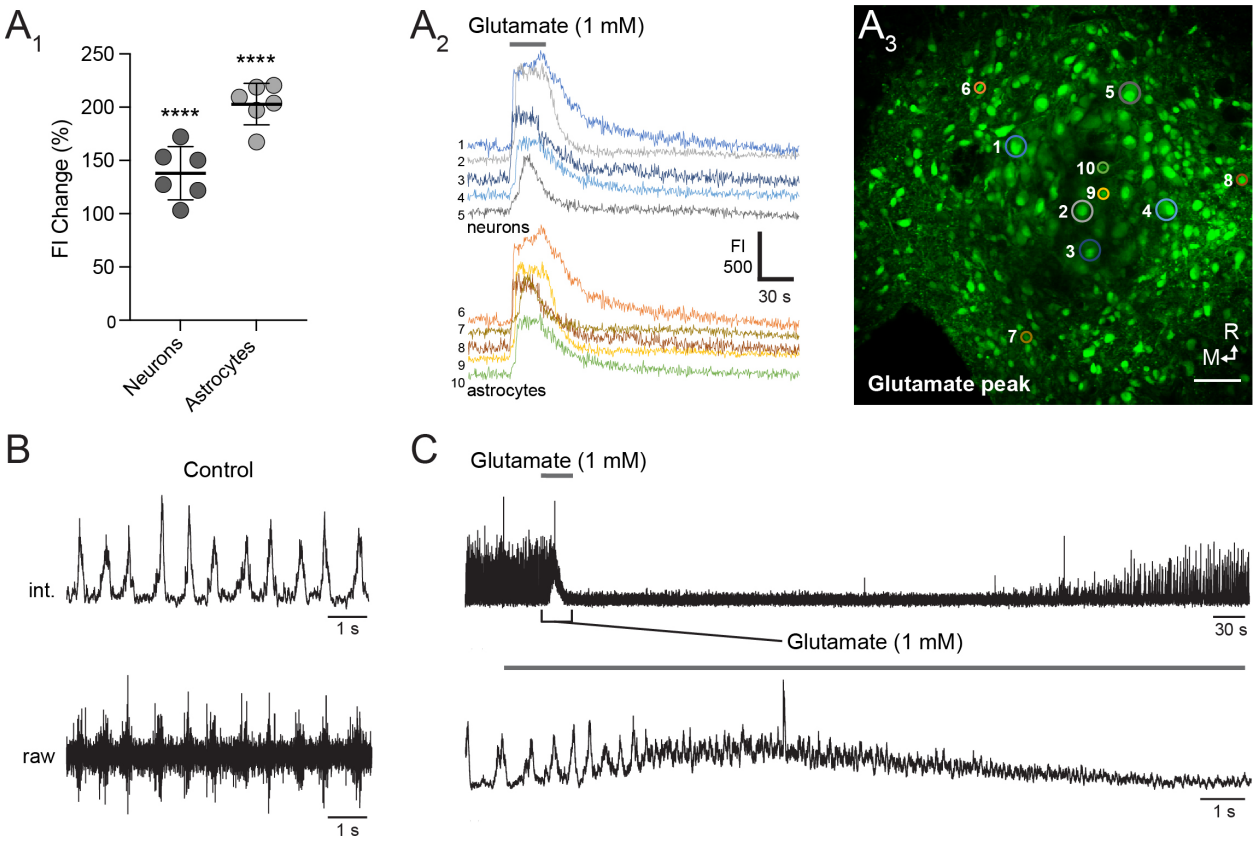

Fig. 3-4: Glutamate-evoked excitation in the neonatal LC. **A_1**, in 400 µm thick slices bulk loaded with Fluo-4-AM, 30 s application of 1mM glutamate increased fluorescence intensity (FI) by an average of 138.04 ± 24.99% in responding neurons vs. a 201.28 ± 19.78% increase in responding astrocytes (n = 6). **A_2**, shows FI changes during glutamate application in regions of interest (ROIs) drawn around 5 neurons and 5 astrocytes indicated by numbered, coloured circles in **A_3**. **B**, LFP recording from the LC neuron soma area in a different slice shows that, in control superfusate, a rhythmic signal at ~ 1 Hz can be recorded. A characteristic LFP bell-shape is observed in the integrated (int.) signal compared to the differentially amplified and band-pass filtered raw signal. **C_2**, when 1 mM glutamate was applied, a burst of tonic activity briefly occurs in the LFP signal before rhythm is blocked. Lines indicate means ± SD, significance was determined with repeated measures one-way ANOVA with Dunnett's multiple comparisons test. Significant values (****P < 0.0001). R, rostral; M, medial. Scale bar for **A_3** 50 µm.

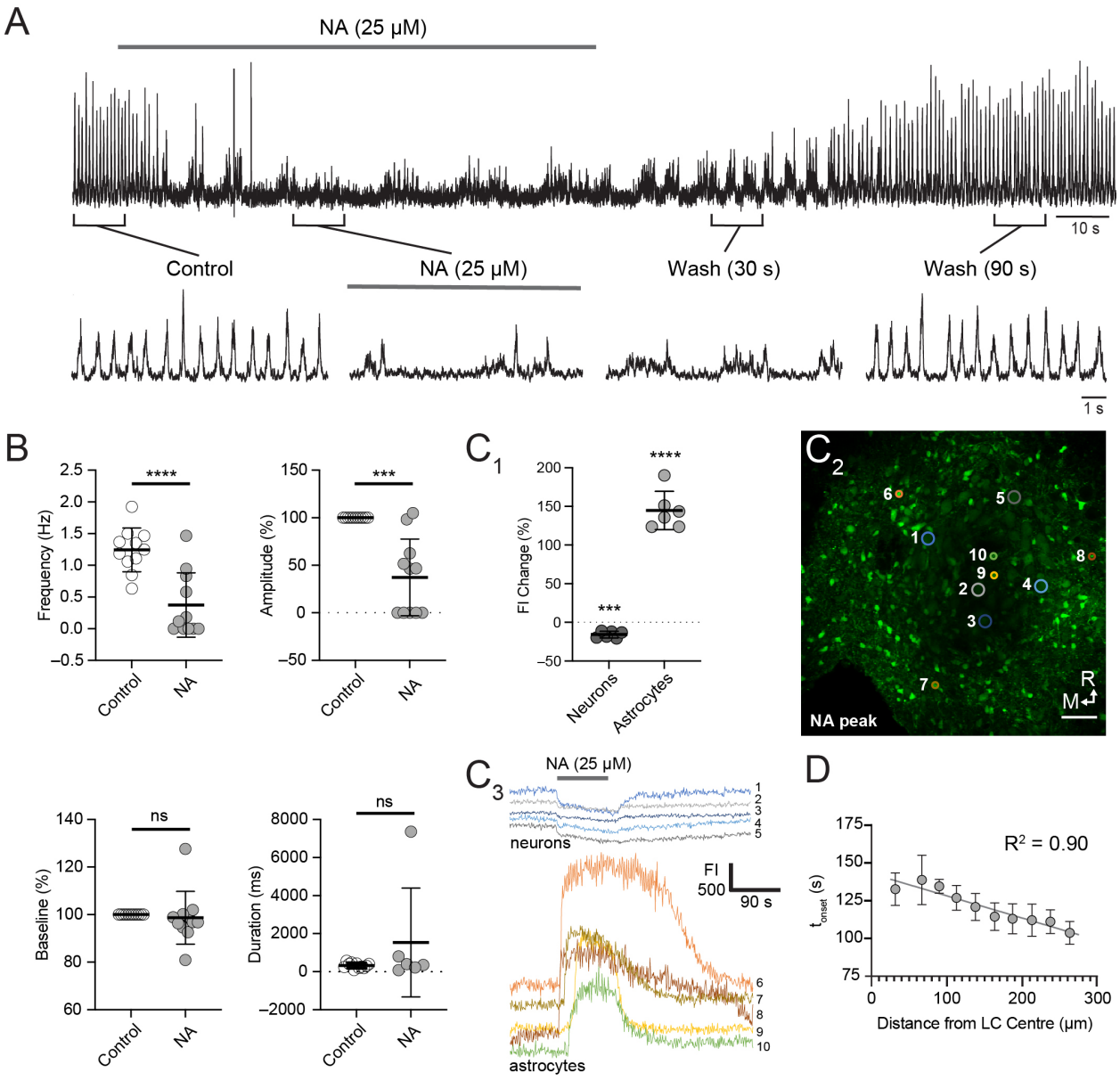

Fig. 3-5: Noradrenaline (NA) depresses LC network activity and evokes an astrocytic 'concentric' Ca_i wave. A_1, during 25 µM NA, LFP-related network activity was blocked in 5 of 11 slices whereas in the remaining 6 it was transformed, as shown here. During this transformation, the typically 1 Hz bell-shaped LFP signal changed to slowed, multipeak events which persisted into early washout. **B**, in 11 slices LFP frequency decreased during NA from 1.24 ± 0.34 Hz to 0.37 ± 0.51 Hz, amplitude decreased to 37.30 ± 40.31% of control. In the 6 slices where the rhythm was transformed, single event duration showed a trend for increasing (324.84 ± 145.51 ms to 1536.84 ± 286.40 ms) but this was not significant. Baseline of the integrated signal was not affected. **C_1**, Ca_i imaging revealed that, in 6 slices Ca_i decreased in responding neurons by 15.80 ± 4.33% but increased by 141.79 ± 23.89% in responding astrocytes which can be seen in an image of the peak NA response in one slice shown in **C_2**. Coloured numbered circles represent ROIs that

have been placed around 5 neurons and 5 astrocytes, while **C_3** shows the FI changes in these cells over time. **D**, shows the average time of onset of FI increase (t_{onset}) in all astrocytes from 6 slices plotted against their distance from the centre of the LC neuron soma area. Correlation analysis yielded a significant R^2 value ($P<0.0001$), indicating that astrocytes located further from the LC centre respond first after which a wave propagates in these cells towards the center of the nucleus. Lines indicate means ± SD, significance was determined with repeated measures one-way ANOVA with Dunnett's multiple comparisons test. Significant values (ns, non-significant, *P < 0.05, **P < 0.01, ***P < 0.001, ****P < 0.0001). Correlation was calculated using Pearson correlation coefficient. R, rostral; M, medial. Scale bar for **C_2** 50 µm.

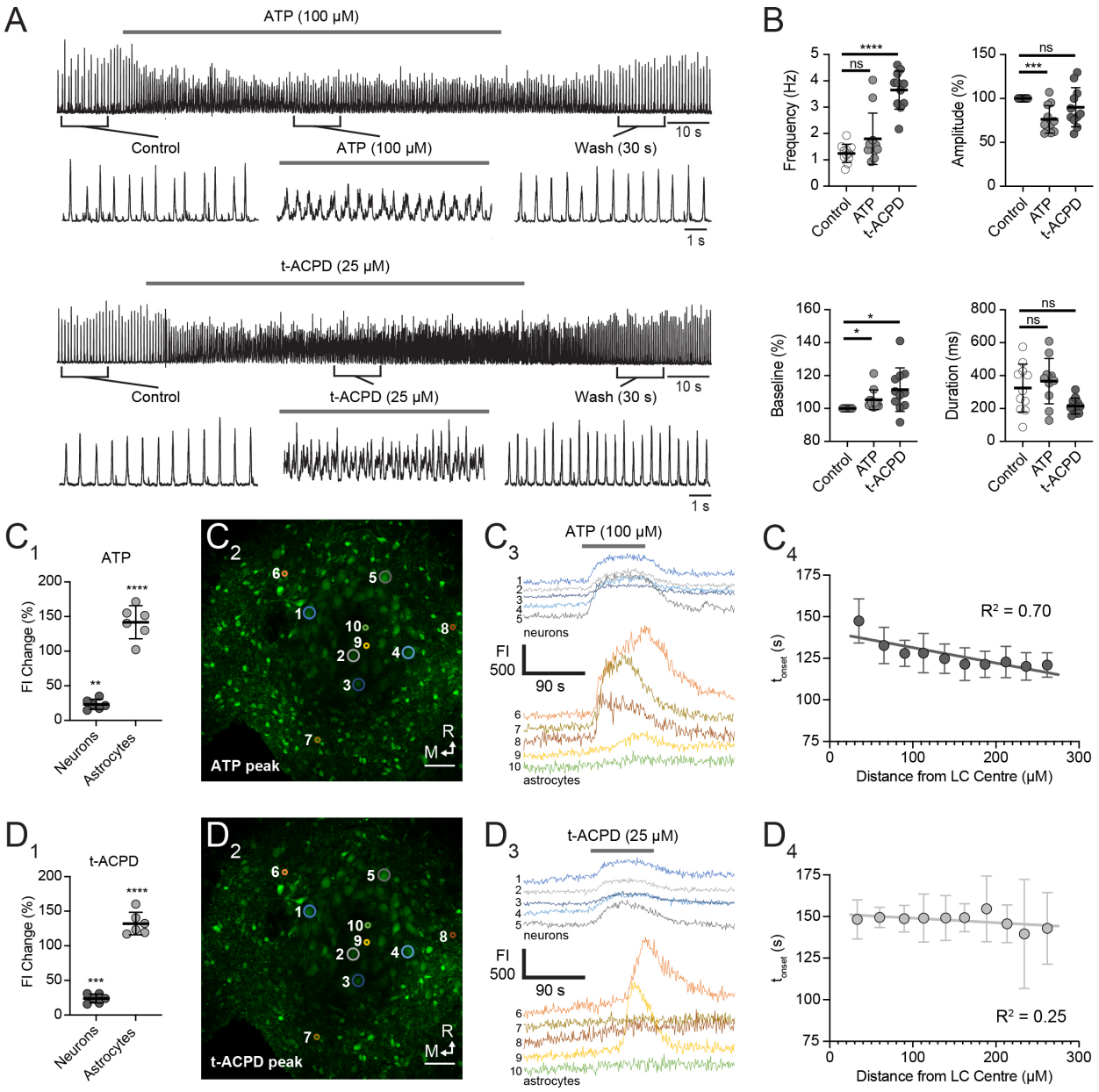

Fig. 3-6: Adenosine triphosphate (ATP) and trans-1-Amino, 3-dicarboxycyclopentane (t-ACPD) have moderately excitatory effects on LC network activity and differ in their ability to evoke concentric astrocyte Ca_i wave. A, both ATP and t-ACPD alter the rhythmic LC LFP pattern. **B**, in 11 slices, 100 µM ATP (90 s) reduced LFP amplitude to 76.14 ± 15.68% of control and increased baseline of the integrated signal to 105.28 ± 6.04% of control, but did not affect rate or single event duration. 25 µM t-ACPD (90 s) accelerated LFP rate in the same slices from 1.25 ± 0.34 Hz to 3.65 ± 0.73 Hz and increased signal baseline to 111.5 ± 13.23% of control but did not affect single event duration or amplitude. **C_1**, Ca_i imaging determined that, in 6 slices, ATP increased FI by 23.24 ± 7.35% and 132.15 ± 16.30% in responding neurons and astrocytes, respectively, which can be seen in the fluorescence image of the ATP-evoked Ca_i peak in one slice

shown in **C2**. **C3**, corresponding FI traces for coloured ROIs shown in **C2** that have been drawn around 5 neurons and 5 astrocytes reveal that Ca_i increased in all of these neurons but only 3 astrocytes. **C4**, in ATP-responding astrocytes, a correlation was found between average t_{onset} and distance from the LC neuron soma area centre ($P = 0.0024$, $n = 6$ slices), indicating that this modulator also evoked concentric Ca_i waves. **D1**, for t-ACPD, FI increased in responding neurons by 23.95 ± 6.46% and in responding astrocytes by 144.65 ± 24.78%. **D2**, shows the peak response to t-ACPD in the same slice as **C2**, with **D3** showing FI traces for ROIs drawn around the same 5 neurons and 5 astrocytes indicating that all 5 neurons again responded to t-ACPD while only 2 of 5 astrocytes responded. **D4**, t-ACPD did not elicit concentric waves and therefore did not yield a significant correlation between t_{onset} and distance from LC centre ($P = 0.1379$, $n = 6$ slices). Lines indicate means ± SD, significance was determined with repeated measures one-way ANOVA with Dunnett's multiple comparisons test. Significant values (ns, non-significant, *$P < 0.05$, **$P < 0.01$, ***$P < 0.001$, ****$P < 0.0001$). Correlation was calculated using Pearson correlation coefficient. R, rostral; M, medial. Scale bars in **C2, D2** 50 μm.

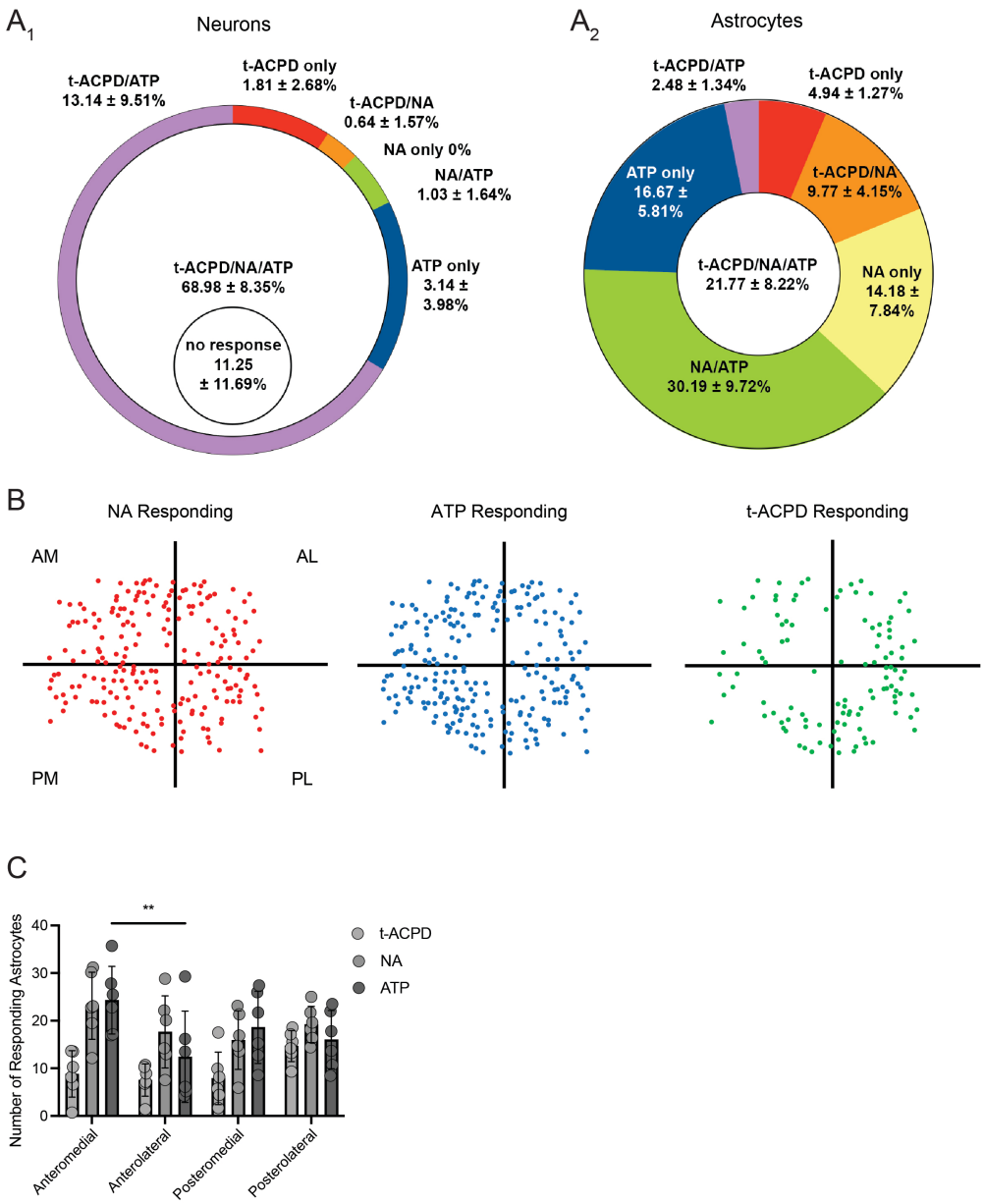

Fig. 3-7: Neonatal LC neurons and astrocytes show modular organization in their responses to NA, ATP, and t-ACPD. **A_1**, donut chart showing mean proportions of subpopulations of glutamate responding neurons from 6 slices based on whether they also respond to NA, ATP, t-ACPD, or a combination of the three. **A_2**, shows the same for astrocytes. **B**, shows the locations of responding astrocytes to NA, ATP, and t-ACPD in one of these slices. Points represent the coordinate of the somata of each responding astrocyte relative to the LC centre, located at the axis intersection. **C**, average number of responding astrocytes found anteromedial, anterolateral, posteromedial, or posterolateral to the LC in 6 slices shows that significantly more astrocytes responded to ATP in the anteromedial versus anterolateral quadrant. No other significant spatial organization of responding astrocytes was observed. AM, anteromedial; AL, anterolateral; PM, posteromedial, PL, posterolateral. Lines indicate means ± SD, significance was determined with two-way ANOVA with Tukey's multiple comparisons test. Significant values (**P < 0.01)

CHAPTER 4

Discussion

This thesis deals with two main questions: first, do neurons and astrocytes in the neonatal rat LC show a particular anatomical distribution in line with its proposed modular organization, and second, does autocrine NA action evoke a novel type of activity that potentially supports the capability of this small nucleus to control multiple brain functions already shortly after birth? As a major anatomical finding, LC astrocyte somata are most densely packed in the pericoerulear region and have an overall lower number and density within the inner LC neuron soma area. The major functional finding is that NA (and ATP) can evoke a novel type of glial Ca_i wave that progresses from presumptive astrocytes peripheral to the LC toward those in its center. In the Discussion, these phenomena, and other findings in this thesis, like potentially distinct neuromodulator receptor profiles on individual LC cells or Ca_i responses in 4th V border cells, are put into the context of previous findings from our group and others.

4.1. Three-dimensional Distribution of LC Neurons and Astrocytes

The basic shape and extension of the area comprising newborn rat LC neurons, as derived from immunohistochemical TH-staining in the present study, is very similar to that described previously in newborn (Ishimatsu and Williams, 1996; Ballantyne et al., 2004; Kantor et al., 2012; Rawal et al., 2019) and adult rats (Amaral and Sinnamon, 1977; Loughlin et al., 1986; Barnes and Pompeiano, 1991). As mentioned previously, TH is an established marker for identifying LC neurons **(2.4.)** and is not expressed in surrounding interneurons or glia (Aston-Jones, 2004). In this project, staining for this marker found that LC neuron somata approach the 4th V from both the dorsal and the ventral LC pole and partly enwrap it, particularly at the level around the central LC aspect where they come within <100 µm of a multilayer of ependymal cells. This results in a roughly spindle-shaped neuronal somata distribution column in the dorsoventral axis. This column

is surrounded by the pericoerulear dendritic area which extends >150 µm in some directions, is most prominent in the anteriomedial direction, and thins out towards both dorsoventral poles. In the pericoerulear region, afferent axons releasing diverse neurotransmitters terminate from remote brain circuits such as the central amygdala, periaqueductal gray, prefrontal cortex, lateral hypothalamus, and dorsal raphe (Ennis et al., 1991; Van Bockstaele et al., 1996; Aston-Jones and Waterhouse, 2016). Moreover, proximal axon collaterals from LC neurons release NA here to affect neighboring cells for autocrine control (Shimizu and Imamoto, 1970; Aghajanian et al., 1977; Cedarbaum and Aghajanian, 1978; Maeda et al., 1991; Benarroch, 2009). Consequently, dendritic trees forming the pericoerulear region are the major site for synaptic integration in LC neurons as is also the case for dendritic regions of neurons in other brain circuits (Gulledge et al., 2005; Hu et al., 2007; Scott et al., 2010). Also like in other brain circuits, pericoerulear synaptic transmission may take place at tripartite synapses formed by pre- and postsynaptic aspects of neurons along with an astrocytic process (Araque et al., 1999; Perea and Araque, 2005; Allen and Barres, 2009; Araque and Navarrete, 2010). Accordingly, a high volume of tripartite synaptic contacts made in the pericoerulear area could underlie our finding that this is also the location where astrocyte somata are most densely packed **(Fig. 3-3C)**. The LC may therefore be similar to the visual cortex or hippocampus, where astrocyte distribution is variable and specialized for the neuronal interactions they participate in (Ogata and Kosaka, 2002; Tsai et al., 2012; Lopez-Hidalgo et al., 2016).

Despite a low density of astrocyte somata deep within the LC neuron soma area, putative neuron-astrocyte interactions could also be prominent here. This is because astrocytes typically possess star-like processes that can extend by >200 µm with >20 branch points in some parts of the

brainstem, which would thereby allow them to make contacts throughout the core of the nucleus (SheikhBahaei et al., 2018). Our protocol (Rawal et al., 2019) stained for the marker S100β, however, which is mainly localized to the astrocyte soma, and only weakly labels processes (Wu et al., 2005). Immunostaining with GFAP antibody is often better suited for labelling astrocyte processes (Oberheim et al., 2008; SheikhBahaei et al., 2018) but this was unsuccessful in our hands, possibly due to comparatively lower expression of this protein in astrocytes from young (compared to mature) brains combined with the low prevalence of GFAP+ astrocytes in the brainstem where the LC is located (Yoshida et al., 1996; Taft et al., 2005; Wu et al., 2005) **(2.4.)**. Moreover, staining for the marker S100β was not selective for astrocyte somata in our slices as a multilayer of presumptive ependymal cells at the boundary of the 4th V was also labelled, as has been reported previously (Steiner et al., 2007). The presence of S100β in these cells indicates that they may share an origin with astrocytes during fetal brain development, and that the ependyma in this area of the 4th V is not highly specialized, in contrast with ependymal cells in other brain regions such as the subcommissural organ (Didier et al., 1986; Vives et al., 2003).

In addition to the limitations of the immunohistochemical staining here, live-cell staining with Fluo-4 indiscriminately labelled the somata of neurons as well as surrounding/interspersed smaller cells which showed a very similar distribution and density to S100β-positive cells. As discussed below, however, these anatomical features combined with the responses of these small cells to applied neuromodulators implicates their identity as astrocytes and not interneurons, microglia, or other glial cells like oligodendrocytes.

4.2. Discrimination of LC Neurons versus Astrocytes with Population Ca_i Imaging

Partly because of its location deep within the brain and its small dimension, only one live-cell Ca^{2+} imaging study has been performed on the LC in vivo (Chen et al., 2021), and none have been done in a neonatal animal. Our group was the first to use Ca_i population imaging in the LC of acutely isolated brain slices obtained from newborn rats (Kantor et al., 2012). In that study and our related work on other spontaneously active neonatal brain circuits, like those in the hippocampal CA_3 area, cortex (Kantor et al., 2012) or inspiratory center (Ballanyi and Ruangkittisakul, 2009) LC cells were loaded with the membrane-permeant fluorescent Ca^{2+} dye Fluo-4-AM by pressure-injection, as was also done for this thesis project. This loading method, in concert with our multiphoton imaging approach using an Olympus MPE system, enables monitoring of Ca_i dynamics of LC neurons and astrocytes at an acquisition rate of 1.1 Hz for images of the entire LC plus ~100 µm of tissue surrounding the LC for >5 h without occurrence of photobleaching or cytotoxicity.

In a previous report from our group (Kantor et al., 2012), newborn rat LC neurons could not be discriminated from neighboring astrocytes using different loading protocols of the red fluorescent dye sulforhodamine-101 as was done in other brain areas like the hippocampus (Nimmerjahn et al., 2004; Kafitz et al., 2008) as both cell types were stained equally. Still, several observations while using our Fluo-4 loading protocol indicate whether Ca_i signals are imaged in LC neurons or glial cells, most likely astrocytes. First, most neurons have a soma size ≥20 µm in contrast to a soma size of ~10 µm for astrocytes. Second, most neurons are visible in control superfusate. This is likely a result of greater persistent fluorescence emission due to ongoing Ca^{2+} influx through predominantly L-type voltage-gated Ca^{2+} channels during STOs and related spiking likely leading

to relatively high somatic Ca_i baseline (Imber and Putnam, 2012; Sanchez-Padilla et al., 2014; Matschke et al., 2015). This is compounded with their not very negative 'resting' V_m, typically close to or less negative than –50 mV, which might cause 'tonic' activation of these channels. A similar relatively high Ca_i baseline has, for example, also been revealed by our group by the effects of drug- or current injection-evoked changes in spike rates for dorsal vagal neurons in juvenile rat brain slices (Ballanyi and Kulik, 1998). As in our previous reports (Kantor et al., 2012; Rawal et al., 2019), neurons studied in this thesis project also did not show baseline phase-locked rhythmic Ca_i oscillations in their somata during spiking. While it is possible that this is a result of Ca_i transients close to the plasma membrane being quickly depressed by endogenous cytosolic Ca^{2+} buffers, intrinsic buffering in LC neurons is low when compared to other cells such as Purkinje neurons (Fierro and Llano, 1996; Sanchez-Padilla et al., 2014). In line with this, rhythmic Ca_i rises in the thin dendrites of LC neurons resulting from single spikes at a rate of often >1 Hz have been recorded in adult mouse slices in which cells were loaded via diffusion from the patch electrode with a low concentration of membrane-impermeant Fluo-4 during whole-cell recording (Sanchez-Padilla et al., 2014). Consequently, slow binding/unbinding kinetics of Fluo-4 also do not seem to be the reason that fast Ca_i rises in the somata of newborn rat LC neurons were not resolved in our studies. This lack of temporal resolution may instead be a product of the 'population' imaging approach used in which a single plane was scanned in a raster-like fashion at a rate of 1.1 frames/s, meaning that the acquisition rate for single cells is identical to the rate for the entire frame (Göbel and Helmchen, 2007). Therefore, Ca_i transients in individual cells lasting $\leq$1 s are likely not visible unless they are precisely in 'phase' with the scanning period.

In some slices from our previous studies, raising superfusate K^+ from physiological 3 mM to 7, and particularly 9 mM, transformed the rhythmic bell-shaped LFP signals into slower, prolonged multipeak events that were associated with phase-locked rhythmic Ca_i oscillations **(Fig. 1-10)** (Kantor et al., 2012; Rancic et al., 2018; Waselenchuk and Ballanyi, 2022). In other slices, raised K^+ moderately increased the rate of the normal LFP rhythm and this likely led to a slight rise of Ca_i baseline (Rancic et al., 2018). In contrast, a separate study showed that blockade of spiking with TTX decreased neuronal Ca_i baseline modestly (Rawal et al., 2019). Importantly, in any of these studies, neither raised K^+ nor TTX had an effect on Ca_i baseline in presumptive astrocytes. This conflicts with the finding that, like neurons, astrocytes can both express L-type Ca^{2+} channels (Cheli et al., 2016; Zamora et al., 2020) and release Ca^{2+} from intracellular stores (Carmignoto et al., 1998; Verkhratsky and Parpura, 2014; Bazargani and Attwell, 2016), suggesting that the two cell types might exhibit very similar activity-related Ca_i changes. However, it is hypothesized that voltage-gated Ca^{2+} channels mediate intrinsic Ca_i changes in astrocytes (i.e., fluctuations in the absence of neuronal input), while Ca_i changes due to activity of afferent inputs occur primarily due to release from the endoplasmic reticulum (Fiacco and McCarthy, 2006). Based on this, it could be concluded that neither TTX application nor raising of extracellular K^+ to 7 or 9 mM cause (voltage-gated) intrinsically mediated Ca_i changes or afferent activity related Ca_i changes in LC astrocytes. Nonetheless, these results indicate that a moderate change in spike rate of LC neurons alters their somatic Ca_i baseline without effect on Ca_i in neighboring astrocytes. As stated in the Introduction **(1.4)**, this can be used as an indirect measure to estimate whether neuromodulator effects are excitatory or inhibitory on LC neurons as discussed below.

Whereas no spontaneous phase-locked rhythmic Ca_i rises were detected in neurons in 3 mM K^+-containing superfusate, our previous reports found that non-synchronous Ca_i rises randomly occurred in ~20% of presumptive astrocytes (Kantor et al., 2012; Rawal et al., 2019). In the Ca_i imaging experiments for this thesis project, though, only ~1% of astrocytes were spontaneously active. However, this observation comes from Ca_i baseline recordings done for ~1 min prior to addition of any drugs to superfusate for studying of their effects, and greater numbers of astrocytes presumably show these 'sparks' during longer recordings. Nevertheless, the bath-application approach for exposing slices to modulators revealed that NA and ATP evoked a concentric Ca_i wave exclusively in the small (glial) cells. Identification of these small cells as astrocytes is supported by the good agreement of density and distribution in the central horizontal plane of Fluo-4-stained small cells with cells of similar soma size that were S100β-positive, as mentioned. While ATP as well as t-ACPD and glutamate also elevated the Ca_i baseline in larger cells representing LC neurons, NA caused a steady Ca_i decrease in neurons as opposed to the wave-like Ca_i rise in astrocytes. For these reasons, besides raising K^+, applying NA may be an appropriate tool to discriminate LC neurons from astrocytes in future 'population' imaging studies. Another interesting approach would be to investigate whether this holds true for other neuromodulators such as 5-HT, substance-P or dopamine.

4.3. LFP Recording as a Tool for Studying LC vs. Pericoerulear Activity

For a better understanding of the responses, this thesis project compared effects of NA, ATP, t-ACPD, and glutamate on Ca_i to those on the LFP recorded within the LC neuron soma area (typically in the contralateral slice aspect during imaging experiments). Overall, the LC rhythm here was very similar in 11 slices regarding LFP rate (1.24 ± 0.34 Hz) and single event duration

(324.84 ± 145.51 ms) compared to those in previous studies from our group as reviewed recently by us (Waselenchuk and Ballanyi, 2022).

Regarding the origin of the LFP signal, it was dealt with in detail in the Introduction **(1.2.1)** that the LC in rodents is spontaneously active in acutely isolated in vitro preparations including horizontal slices from newborn rats. In such slices, generated with the aim to cut roughly through the centre of the LC in the dorsoventral axis where there is a large number of neurons, our group found a robust rhythmic LFP comprising summated phase-locked single spikes that are elicited at the peak of Ca^{2+}-dependent STOs presumably generated by intrinsic conductances (Kantor et al., 2012; Rancic et al., 2018; Waselenchuk and Ballanyi, 2022). In most brain slices, afferent axons can still spontaneously release neurotransmitter and therefore modulate intrinsic neuronal activity (Ballanyi, 1999; Ballanyi and Ruangkittisakul, 2009). Accordingly, spontaneous neurotransmitter release in the pericoerulear area may evoke EPSPs and/or IPSPs randomly in LC neurons and therefore change the time point at which the synchronous STOs reach the spike threshold. In fact, our group has discussed that this scenario may explain, at least partly, the jitter of single neuron spiking referred to the LFP peak (Rancic et al., 2018; Waselenchuk and Ballanyi, 2022). 'Classical' synaptic processes mediated, e.g., by iGluRs, $GABA_A$Rs, GlyRs, NARs, or µRs do not seem to be important for the generation, rate, or shape of LFP events as indicated by a lack of effect of specific antagonists for these receptors (Rancic et al., 2018; Rawal et al., 2019, 2022; Waselenchuk and Ballanyi, 2022) **(1.2.2., 1.2.3., 1.2.4.)**. In addition to synaptic integration or modulation, electrical coupling seems to be strong in the pericoerulear area. This is suggested by a study in which an enhanced rhythmic and synchronous LFP was recorded with sharp microelectrodes in the neuron soma LC region in solution containing 10 mM tetraethylammonium

chloride and 1 mM $BaCl_2$ to enhance excitability (Ishimatsu and Williams, 1996). The authors further reported that this LFP was reduced or abolished when the pericoerulear dendritic regions were removed by sectioning the slice rostral and caudal to the cell body region, implicating that this region is critical to synchronization of activity (Ishimatsu and Williams, 1996).

Based on the latter considerations, one would expect that a robust LFP can also be recorded in the pericoerulear area of horizontal newborn rat slices kept in superfusate with close-to-physiological ion content. However, at least in horizontal slices cut close to the dorsoventral LC center, the anatomical LFP distribution appears restricted to the area of neuronal somata as shown by our group (Rancic et al., 2018). Consequently, using our recording method, no LFP is detectable >50 µm outside the neuron soma area except in two small regions rostral and caudal to the 4^{th} V. This prevented LFP recording from being an effective tool for delineating activity changes specifically in the pericoerulear area.

Possibly, the inability to detect a measurable LFP in the pericoerulear area using suction electrodes is related to intrinsic characteristics of the signal. The LFP signal reported here represents phase-locked spiking in 3-10 LC neurons. We previously found that when suction electrodes with a tip diameter <20 µm were positioned close to the slice surface between the densely packed neuron cell bodies, the LFP was not or barely detectable without applying modest suction (Rancic et al., 2018). Moreover, no extracellular signal was seen in that study when recording with an unbroken patch electrode with a tip diameter of ~2 µm positioned between neuron somata. In contrast, extracellular spikes with an amplitude of several millivolts were recorded when an unbroken patch electrode was slightly pushed against the soma of a single neuron for a 'loose patch' recording

(Hille, 1984). Within the pericoerulear area, though, the amplitude of intracellularly recorded spikes from single neurons may be slightly smaller than at their origin, which is likely close to the soma at the axon hillock. However, given the high density of neuronal processes and their relatively small distances from their soma, one would expect spikes from multiple cells to be detectable at reasonable amplitude in the pericoerulear area. Yet, for unknown reasons, perhaps related to the geometry of this area and/or its current source/sink/density properties (Buzsáki et al., 2012; Einevoll et al., 2013), electrical signals do not summate to generate a detectable LFP. As noted above, visualization of neuronal Fluo-4 staining was also restricted to the somata of LC neurons. Consequently, neuromodulator effects could similarly not be analysed with Ca_i population imaging in the main area of synaptic integration within the LC.

4.4. Mechanisms of Drug Effects on LC Neurons and Astrocytes

In summary of the drug effects on cytosolic Ca^{2+}, glutamate, ATP and t-ACPD raised Ca_i baseline in both neurons and astrocytes, whereas NA caused Ca_i baseline increase in astrocytes, but lowered it in neurons. On LC neurons, NA principally acts excitatory via α_1R and inhibitory via α_2R (Young and Kuhar, 1980; De Sarro et al., 1987; Benarroch, 2009; Szabadi, 2013). Concerning excitatory effects, it was found that α_1R agonists depolarize LC neurons in rat slices to accelerate tonic firing, whereas α_2R agonists evoke a hyperpolarization to depress it (Williams et al., 1985, 1991; Aghajanian and Wang, 1987; Williams and Marshall, 1987). Bath-application of NA was used here to mimic a global increase within the LC. A similar uniform NA increase may occur under the influence of cocaine which blocks the reuptake of (spontaneously released) NA (Pitts and Marwah, 1986; Surprenant and Williams, 1987; Williams and Marshall, 1987; Benarroch, 2009). In that regard, it was found in LC neurons of adult rat slices that bath-applied cocaine causes

a decrease in the firing rate and evokes the occurrence of slow spike doublets or bursts and that these effects are blocked by α_2R antagonists (Williams and Marshall, 1987). The same group also showed that α_2R agonists like clonidine hyperpolarize LC neurons and inhibit their spiking (Williams et al., 1985). Preliminary findings from our group indicate that low clonidine doses slightly slow the LFP in the LC of newborn rat slices with the occurrence of multipeak LFP events lasting several seconds whereas higher doses block the rhythm and lower the Ca_i baseline **(Fig. 1-8)** (Waselenchuk and Ballanyi, 2022). Here, NA had a depressing effect on the LFP and the majority of LC neurons showed a decrease of Ca_i baseline implying that global NA increase in the neonatal rat LC has an overall inhibitory effect on LC neurons. This indicates a stronger action of α_2Rs as opposed to α_1Rs which is in agreement with the opinion that α_1Rs play a comparatively minor role in mediation of LC neuronal activity (Marwaha and Aghajanian, 1982; Nicholas et al., 1996). Likely, this is a result of reliance on α_2Rs by these cells for tonic inhibitory control (Singewald and Philippu, 1998; Fernández-Pastor and Meana, 2002) and autoinhibition of NA release after periods of high activity (Baral et al., 2022). In contrast, astrocytes, which can principally also express both types of αRs (Gaidin et al., 2020; Wahis and Holt, 2021), show NA-evoked Ca_i increases in the LC that appear α_1R mediated. This assumption is based on preliminary findings from our group by Dr. Rawal that the selective blocker of these receptors prazosin abolishes the NA response in astrocytes without attenuating the accompanying neuronal Ca_i decrease. Preliminary experiments done as part of this thesis project and not included here also support these findings. Preferential action of NA at α_1R in LC astrocytes is in accordance with the hypothesis that NA binds this receptor to stimulate L-lactate release which acts as a gliotransmitter to facilitate neuron-astrocyte communication (Tang et al., 2014; Teschemacher and Kasparov, 2017; Mosienko et al., 2018).

Regarding effects of the mGluR agonist t-ACPD on neurons, it evoked a Ca_i baseline increase opposite to the Ca_i decrease during NA. As the clearest mechanisms, the agent accelerated LFP rate likely causing enhanced Ca^{2+} influx as was discussed above for the effect of elevated K^+. It is not clear though exactly why the agent increases the spike rate. While t-ACPD acts on mGluR and not iGluR, it binds to several mGluR subtypes (Cartmell and Schoepp, 2000; Niswender and Conn, 2010). As dealt with in these review articles, t-ACPD can depolarize neurons by activating diverse types of cation channels including voltage-gated Ca^{2+} channels. In addition, it can promote Ca^{2+} release from the endoplasmic reticulum via second-messenger signalling (Nakamura et al., 2000). These mechanisms can also work in concert, such that mGluR-activated inositol triphosphate (IP_3) acts together with Ca^{2+} entering the cell due to voltage-gated channels to open IP_3Rs on the endoplasmic reticulum that allow intracellular Ca^{2+} release, as has been found in hippocampal CA_3 neurons (Nakamura et al., 2000). Likely, the same mechanism is occurring in LC neurons. Although the t-ACPD evoked Ca_i rise was greater in magnitude in astrocytes, it was presumably due solely to release from endoplasmic reticulum stores in these cells as it has been reported that they do not show Ca_i rises upon depolarization when intracellular stores are first emptied with cyclopiazonic acid, despite also possessing voltage gated Ca^{2+} channels (Carmignoto et al., 1998). Newer studies using IP_3R gene knockout techniques are in support of this, however it should be noted that they further unravelled that this is exclusive to Ca^{2+} transients in astrocyte somata, whereas signaling is different in processes (Kanemaru et al., 2014; Srinivasan et al., 2015; Bazargani and Attwell, 2016). As this project only looked at Ca_i changes in astrocyte somata, though, it is reasonable to confer that observed mGluR-evoked Ca_i transients were primarily a result of IP_3R activation.

Similar to t-ACPD, ATP elicited a Ca_i rise in astrocytes that was more prominent than that in neurons. The modest neuronal Ca_i increase is partly explained by the finding that ATP showed only a trend for decreasing LFP amplitude without significantly increasing frequency and thus may not be sufficient to enhance Ca^{2+} influx via spike-activated channels. In contrast to t-ACPD, ATP can act on both ionotropic and metabotropic purinergic receptors that coupled to different types of ion channels and signaling pathways (Burnstock, 2006; Verkhratsky and Krishtal, 2009). Accordingly, extensive pharmacological/genetic analyses would be necessary to figure out the exact nature of mGluR and purinergic receptors in the neonatal LC. In any case, the new findings presented here show that subgroups of these receptors are active in the neonatal LC and that their activation can affect its network rhythm and Ca_i dynamics.

4.5. Concentric Ca_i Wave in Astrocytes

A major novel functional result of this thesis project was that neonatal LC astrocytes can propagate concentric Ca_i waves. This is the first report in which an astrocyte network becomes active in the periphery of a small brain nucleus and subsequently transmits this activity towards it. Astrocytic Ca_i waves were first detected in hippocampal cultures (Cornell-Bell et al., 1990) and subsequently have also been observed in other cultured brain circuits (Nedergaard, 1994). Originally, it was suspected that this phenomenon is an experimental artifact related to a change in the original circuit connectivity caused by the particular culture conditions. However, this glial network property has also been demonstrated in acutely isolated slices, e.g, in the cortex (Haas et al., 2006) and other brain structures (Basarsky et al., 1998; Newman, 2001). More recently, Ca_i waves have also been found in vivo, for example in the hippocampus (Kuga et al., 2011) and cortex (Hirase et al., 2004). Regarding mechanism, these waves are initiated intracellularly usually when activity at a GPCR

leads to activation of IP_3Rs and subsequent Ca^{2+} release from the endoplasmic reticulum (Scemes and Giaume, 2006). They are then transmitted intercellularly by either gap junction coupling (Charles et al., 1991; Finkbeiner, 1992; Blomstrand et al., 1999) or using extracellular pathways involving release of signalling molecules such as ATP (Hassinger et al., 1996; Guthrie et al., 1999).

In LC astrocytes, NA, ATP, t-ACPD and glutamate likely cause Ca^{2+} release partially via the same second-messenger pathway and it was previously shown that these astrocytes are connected via gap junctions (Van Bockstaele et al., 2004). Moreover, it was shown that connexin-32 gap junctions also connect LC astrocytes with neurons who are themselves connected primarily via connexin-36 gap junctions, particularly in newborns (Ishimatsu and Williams, 1996; Alvarez-Maubecin et al., 2000; Ballantyne et al., 2004; Van Bockstaele et al., 2004), although these claims are controversial (Rash et al., 2007). Despite gap junction coupling seeming pivotal for spreading of Ca_i waves in the LC astrocyte network, proposed coupling between LC astrocytes and neurons is not sufficient to also elicit a major Ca_i rise in neuronal somata. It is however possible that Ca_i increases during the concentric wave in subregions of pericoerulear processes. Regardless, the propagation of Ca_i waves in LC astrocytes may be a critical aspect of heterocellular communication. One potentially relevant function of this in the neonatal LC involves control of synaptic activity whereby neuronal activity evokes an astrocyte wave response leading to gliotransmitter release and subsequent modulation of further neuronal activity (Fellin and Carmignoto, 2004; Volterra and Meldolesi, 2005; Scemes and Giaume, 2006). This aligns with the finding in cultured LC neurons and astrocytes from neonatal rats that the two cell types communicate, perhaps as a feedback mechanism, by release of L-lactate as a gliotransmitter (Tang et al., 2014). Whether or not the wave phenomenon is an important aspect of this, though, remains

unclear. Nonetheless, the concentric wave connects activity in a three-dimensional network outside the pericoerulear region and the core of the LC. It is unknown why astrocytes surrounding the LC respond earlier to the bath-applied LC which approaches the slice as a bolus that mainly proceeds in one direction. It also remains to be determined whether NA release within the LC core would elicit a concentric Ca_i wave propagating to the periphery.

4.6. Modular Responses of LC Neurons and Astrocytes to Neuromodulators

As reviewed recently (Totah et al., 2019), it was assumed for many decades that the LC comprises a relatively simple neural network that releases NA in an often synchronous and pulse-like fashion into its target brain areas, analogous to a rhythmic heartbeat transporting nutrients and oxygen to the organs. Conversely, as outlined in detail in the Introduction **(1.1.3.)** (Waselenchuk and Ballanyi, 2022), evidence has been steadily increasing for several years that the (adult) LC has a modular organization. In brief, this means that in distinct subregions of the LC: (*i*) afferent axons from certain brain regions terminate, (*ii*) neurons have specific soma/dendrite morphology, have discrete electrophysiological properties, project to particular target areas and/or release from their axon terminals/varicosities a specific type of co-transmitter like galanin (Swanson, 1976; Loughlin et al., 1986; Holets et al., 1988; Chamba et al., 1991; Schwarz and Luo, 2015; Schwarz et al., 2015; Totah et al., 2018). In addition, it was recently shown that somatodendritic α_2R-mediated responses of certain LC neurons vary based on their projection targets (Wagner-Altendorf et al., 2019).

As also outlined in the Introduction **(1.2.1., 1.2.5.)** (Waselenchuk and Ballanyi, 2022), there is evidence that modular organization is already present in the neonatal LC. This is suggested by the

finding that, e.g., neurons respond differently to current injection such that they can be classified as pacemaker, burster, or irregular, or that neurons respond differently to electrical stimulation with either a return to Ca_i baseline or an undershoot. This thesis provides another piece of evidence for a modular neonatal LC organization. Neuronal and astrocytic responses to NA, ATP and t-ACPD were not uniform. In fact, some cells responded exclusively to one or two of these agents. This suggests that neuron and astrocytes express receptors for these modulators in a different fashion, and contrasts with our previous finding that all neurons responded similarly to AMPAR activation with CNQX which did not change Ca_i levels in astrocytes (Rawal et al., 2019).

4.7. Future Directions

As a summary of directions discussed in the Introduction **(1.3.6)** (Waselenchuk and Ballanyi, 2022) focal injection of drugs (as opposed to bath application) can be used along with LFP, cellular, or multi-electrode recording, imaging of cellular signalling factors, and PCR to reveal different subpopulations of neurons based on responses to modulators. New slice models can also be used in which connectivity is retained between the LC and remote brain areas. Lastly, it was suggested that LFP or multi-electrode array recordings can be combined with monitoring single neuron V_m for the purpose of modeling oscillations. Further propositions are now discussed below. As noted, opto and chemogenetic approaches have also emerged as powerful tools that often deduce significant results in the study of neural networks, but are still challenging to apply to neonatal models due to the requirement for in utero manipulations (Bitzenhofer et al., 2017). They are therefore not proposed here.

Anatomically, the organization of LC astrocyte somata has been characterized using antibodies for S100β. A logical next step is to unravel the organization of their processes, as this is likely where functional interactions occur. As astrocyte immunostaining for the marker S100β does not label processes well **(4.1)**, and GFAP antibodies did not effectively label processes or somata in our hands, additional markers should be tested. For example, vimentin is useful for analyzing astrocyte morphology, but has limited use due to its primary expression in developing brains (Pixley and de Vellis, 1984). In contrast, this may make it particularly useful in our neonatal model. Visualization of astrocyte processes would also allow one to identify variation between pericoerulear astrocytes and those located within the LC neuron soma area, e.g., based on process length and extent of branching, as has been done for astrocytes in different regions of the inspiratory centre (SheikhBahaei et al., 2018). Findings other brainstem regions also showed that astrocytes here can violate the principle of 'tiling' (Grosche et al., 2002; Halassa et al., 2007; Lopez-Hidalgo et al., 2016; SheikhBahaei et al., 2018) and instead overlap their domains, which should also be explored in the LC. Moreover, analysis of proteome expression in LC versus pericoerulear astrocytes processes using mass spectrometry may reveal differences in synaptic machinery underlying communication at these two sites (Dieterich and Kreutz, 2016; Sapkota et al., 2020). Lastly, identification of astrocyte process morphology near the 4th V would be interesting as it is reported here that they appear to contact ependymal cells. Connexins are heavily expressed in the 4th V ependyma (Rash et al., 2007), and it is unknown whether there could also be functional heterocellular coupling between ependymal cells and astrocytes.

Further analysis of the concentric wave phenomenon would also provide new insights on astrocytes in this network. In part, this could be done using pharmacology. Our preliminary

findings that α_1R antagonists block the wave should first be consolidated. This is especially important as it was shown in the hippocampus that activation of the α_2R-coupled $Gi_{/o}$ signaling pathway similarly causes Ca_i rises in astrocytes (Durkee et al., 2019). As ATP also evokes this wave response, the specific purinergic receptors involved can be elucidated. It is also noted **(4.5)** that waves can be propagated either by gap junctions or using extracellular communication for non-coupled astrocytes (Hassinger et al., 1996; Guthrie et al., 1999). ATP is heavily implicated as the messenger underlying extracellular communication in Ca_i waves (Hassinger et al., 1996; Guthrie et al., 1999), so application of purinergic receptor blockers together with NA may determine whether ATP activity is necessary for these waves to occur in the LC.

The nature of the observed neuronal responses to modulators can also be examined in more depth. Multi-photon imaging techniques using high frequency scan rates in a small area have been used measure fast Ca_i fluctuations in dendrites of hippocampal (Sabatini and Svoboda, 2000) and LC neurons (Sanchez-Padilla et al., 2014). This same approach can be applied to dendrites of LC neurons in the pericoerulear area to compare responses here with those measured in the somata, as there may be different Ca_i changes compartmentalized to certain aspects of these cells. It was also found here that Ca_i responses to the modulators tested only occur in a subset of neuronal somata. Combining imaging with whole-cell recording can be done to reveal whether these cells are not responding (indicating lack of receptor expression) or whether they rather show too small of a change in activity for it to be reflected as a fluorescence change using our imaging protocol. In the Introduction **(1.3.3)**, modularity in terms of intrinsic conductances of these neurons is also shown. Mapping the classification of a neuronal response to current injection on to its Ca_i response to, e.g., autocrine NA activity may also be interesting

Lastly, it needs to be determined how these findings involve brain structures surrounding the LC. For example, it is well studied that GABAergic neurons located in the pericoerulear region can act inhibitory on LC neurons (Aston-Jones et al., 2004; Jin et al., 2016; Breton-Provencher and Sur, 2019). These synaptic contacts play a role in regulating phasic activity of the LC and have thus been implicated in control of wakefulness and arousal (Breton-Provencher and Sur, 2019; Kuo et al., 2020). Glutamatergic, neuropeptide-S-expressing, and cholinergic neurons have also been identified in this region, but their connection to LC-mediated behaviour is unknown (Breton-Provencher et al., 2021). A set of FoxP2 brainstem neurons termed the pre-LC are additionally located immediately rostral to the LC and can intermingle with LC neurons or be found within the pericoerulear region (Shin et al., 2011; Gasparini et al., 2021) and the function of these neurons is similarly not well understood. However, as these neurons can all be situated in regions with high degrees of synaptic integration between LC neurons and astrocytes, their role in LC signalling and activity regulation should be considered.

Together, the presented results highlight structural and functional complexity in the neonatal LC and might lead to future studies on, e.g., the underlying mechanisms and the relationship between their dysfunction and various pathologies. As one example, a correlation has been found between occurrence of sudden infant death syndrome and loss of noradrenergic activity of the LC due to maternal smoking during gestation (Lavezzi et al., 2005). Smoking during gestation might disrupt an aspect of noradrenergic activity in the LC observed here, implicating possible clinical relevance of these findings.

References

Aghajanian GK, Cedarbaum JM, Wang RY (1977) Evidence for norepinephrine-mediated collateral inhibition of locus coeruleus neurons. Brain Res 136:570–577.

Aghajanian GK, Wang Y-Y (1987) Common α_2- and opiate effector mechanisms in the locus coeruleus: intracellular studies in brain slices. Neuropharmacology 26:793–799.

Ahmadi-Soleimani SM, Azizi H, Gompf HS, Semnanian S (2017) Role of orexin type-1 receptors in paragiganto-coerulear modulation of opioid withdrawal and tolerance: A site specific focus. Neuropharmacology 126:25–37.

Ahmadi-Soleimani SM, Azizi H, Mirnajafi-Zadeh J, Semnanian S (2015) Orexin type 1 receptor antagonism in rat locus coeruleus prevents the analgesic effect of intra-LC met-enkephalin microinjection. Pharmacol Biochem Behav 136:102–106.

Ahmadi-Soleimani SM, Ghaemi-Jandabi M, Azizi H, Semnanian S (2014) Orexin type 1 receptor antagonism in Lateral Paragigantocellularis nucleus attenuates naloxone precipitated morphine withdrawal symptoms in rats. Neurosci Lett 558:62–66.

Allen NJ, Barres BA (2009) Glia — more than just brain glue. Nature 457:675–677.

Alreja M, Aghajanian GK (1991) Pacemaker activity of locus coeruleus neurons: whole-cell recordings in brain slices show dependence on cAMP and protein kinase A. Brain Res 556:339–343.

Alvarez VA, Chow CC, Van Bockstaele EJ, Williams JT (2002) Frequency-dependent synchrony in locus ceruleus: Role of electrotonic coupling. PNAS 99:4032–4036.

Alvarez-Maubecin V, García-Hernández F, Williams JT, Bockstaele EJV (2000) Functional Coupling between Neurons and Glia. J Neurosci 20:4091–4098.

Amaral DG, Sinnamon HM (1977) The locus coeruleus: neurobiology of a central noradrenergic nucleus. Prog Neurobiol 9:147–196.

Andrade R, Aghajanian GK (1984) Locus coeruleus activity in vitro: intrinsic regulation by a calcium-dependent potassium conductance but not alpha 2-adrenoceptors. J Neurosci 4:161–170.

Araque A, Navarrete M (2010) Glial cells in neuronal network function. Philos Trans R Soc Lond B Biol Sci 365:2375–2381.

Araque A, Parpura V, Sanzgiri RP, Haydon PG (1999) Tripartite synapses: glia, the unacknowledged partner. Trends in Neurosci 22:208–215.

Aston-Jones G, Zhu Y, Card JP (2004) Numerous GABAergic Afferents to Locus Ceruleus in the Pericerulear Dendritic Zone: Possible Interneuronal Pool. J Neurosci 24:2313–2321.

Aston-Jones G, Shipley MT, Chouvet G, Ennis M, van Bockstaele E, Pieribone V, Shiekhattar R, Akaoka H, Drolet G, Astier B, Charléty P, Valentino RJ, Williams JT (1991) Chapter 4 - Afferent regulation of locus coeruleus neurons: anatomy, physiology and pharmacology. In: Progress in Brain Research (Barnes CD, Pompeiano O, eds), pp 47–75 Neurobiology of the Locus Coeruleus. Elsevier.

Aston-Jones G, Waterhouse B (2016) Locus coeruleus: From global projection system to adaptive regulation of behavior. Brain Res 1645:75–78.

Avramiea A-E, Masood A, Mansvelder HD, Linkenkaer-Hansen K (2022) Long-range amplitude coupling is optimized for brain networks that function at criticality. J Neurosci JN-RM-1095-21.

Ballantyne D, Andrzejewski M, Mückenhoff K, Scheid P (2004) Rhythms, synchrony and electrical coupling in the Locus coeruleus. Resp Physiol Neurobiol 143:199–214.

Ballanyi K (1999) In Vitro Preparations. In: Modern Techniques in Neuroscience Research (Windhorst U, Johansson H, eds), pp 307–326. Berlin, Heidelberg: Springer.

Ballanyi K, Eschenko O (2022) Anesthesia-related LC neuron bursting in adult rats in vivo. *in preparation*

Ballanyi K, Kulik A (1998) Intracellular Ca^{2+} during metabolic activation of KATP channels in spontaneously active dorsal vagal neurons in medullary slices. Euro J Neurosci 10:2574–2585.

Ballanyi K, Ruangkittisakul A (2009) Structure–function analysis of rhythmogenic inspiratory pre-Bötzinger complex networks in “calibrated” newborn rat brainstem slices. Resp Physiol Neurobiol 168:158–178.

Baral S, Hosseini H, More K, Fabrin TMC, Braun J, Prigge M (2022) Spike-Dependent Dynamic Partitioning of the Locus Coeruleus Network through Noradrenergic Volume Release in a Simulation of Nucleus Core. Brain Sci 12:728.

Barnes CD, Pompeiano O (1991) Neurobiology of the Locus Coeruleus. Elsevier.

Bartos M, Vida I, Jonas P (2007) Synaptic mechanisms of synchronized gamma oscillations in inhibitory interneuron networks. Nat Rev Neurosci 8:45–56.

Basarsky TA, Duffy SN, Andrew RD, MacVicar BA (1998) Imaging Spreading Depression and Associated Intracellular Calcium Waves in Brain Slices. J Neurosci 18:7189–7199.

Bazargani N, Attwell D (2016) Astrocyte calcium signaling: the third wave. Nat Neurosci 19:182–189.

Benarroch EE (2009) The locus ceruleus norepinephrine system: Functional organization and potential clinical significance. Neurology 73:1699–1704.

Berridge CW, Waterhouse BD (2003) The locus coeruleus–noradrenergic system: modulation of behavioral state and state-dependent cognitive processes. Brain Res Rev 42:33–84.

Bitzenhofer SH, Ahlbeck J, Hanganu-Opatz IL (2017) Methodological Approach for Optogenetic Manipulation of Neonatal Neuronal Networks. Front Cell Neurosci 11

Blomstrand F, Åberg ND, Eriksson PS, Hansson E, Rönnbäck L (1999) Extent of intercellular calcium wave propagation is related to gap junction permeability and level of connexin-43 expression in astrocytes in primary cultures from four brain regions. Neuroscience 92:255–265.

Bracci E, Ballerini L, Nistri A (1996) Localization of Rhythmogenic Networks Responsible for Spontaneous Bursts Induced by Strychnine and Bicuculline in the Rat Isolated Spinal Cord. J Neurosci 16:7063–7076.

Breton-Provencher V, Drummond GT, Sur M (2021) Locus Coeruleus Norepinephrine in Learned Behavior: Anatomical Modularity and Spatiotemporal Integration in Targets. Frontiers in Neural Circuits 15

Breton-Provencher V, Sur M (2019) Active control of arousal by a locus coeruleus GABAergic circuit. Nat Neurosci 22:218–228.

Brockhaus J, Ballanyi K (1998) Synaptic inhibition in the isolated respiratory network of neonatal rats. Eur J Neurosci 10:3823–3839.

Brofiga M, Pisano M, Raiteri R, Massobrio P (2021) On the road to the brain-on-a-chip: a review on strategies, methods, and applications. J Neural Eng 18:041005.

Burnstock G (2006) Historical review: ATP as a neurotransmitter. Trends Pharm Sci 27:166–176.

Buzsáki G, Anastassiou CA, Koch C (2012) The origin of extracellular fields and currents — EEG, ECoG, LFP and spikes. Nat Rev Neurosci 13:407–420.

Carmignoto G, Pasti L, Pozzan T (1998) On the Role of Voltage-Dependent Calcium Channels in Calcium Signaling of Astrocytes *In Situ*. J Neurosci 18:4637–4645.

Carrillo-Reid L, Yang W, Kang Miller J, Peterka DS, Yuste R (2017) Imaging and Optically Manipulating Neuronal Ensembles. Ann Rev Biophys 46:271–293.

Carter ME, Yizhar O, Chikahisa S, Nguyen H, Adamantidis A, Nishino S, Deisseroth K, de Lecea L (2010) Tuning arousal with optogenetic modulation of locus coeruleus neurons. Nat Neurosci 13:1526–1533.

Cartmell J, Schoepp DD (2000) Regulation of Neurotransmitter Release by Metabotropic Glutamate Receptors. J Neurochem 75:889–907.

Cedarbaum JM, Aghajanian GK (1978) Activation of locus coeruleus neurons by peripheral stimuli: Modulation by a collateral inhibitory mechanism. Life Sci 23:1383–1392.

Chamba G, Weissmann D, Rousset C, Renaud B, Pujol JF (1991) Distribution of alpha-1 and alpha-2 binding sites in the rat locus coeruleus. Brain Res Bulletin 26:185–193.

Chandler DJ, Gao W-J, Waterhouse BD (2014) Heterogeneous organization of the locus coeruleus projections to prefrontal and motor cortices. PNAS 111:6816–6821.

Chandler DJ, Jensen P, McCall JG, Pickering AE, Schwarz LA, Totah NK (2019) Redefining Noradrenergic Neuromodulation of Behavior: Impacts of a Modular Locus Coeruleus Architecture. J Neurosci 39:8239–8249.

Charles AC, Merrill JE, Dirksen ER, Sandersont MJ (1991) Intercellular signaling in glial cells: Calcium waves and oscillations in response to mechanical stimulation and glutamate. Neuron 6:983–992.

Cheli VT, Santiago González DA, Smith J, Spreuer V, Murphy GG, Paez PM (2016) L-type voltage-operated calcium channels contribute to astrocyte activation In vitro. Glia 64:1396–1415.

Chen H, Xu D, Zhang Y, Yan Y, Liu J, Liu C, Shen W, Yu T, Liu J (2021) Neurons in the Locus Coeruleus Modulate the Hedonic Effects of Sub-Anesthetic Dose of Propofol. Front Neurosci 15

Christi MJ, Jelinek HF (1993) Dye-coupling among neurons of the rat locus coeruleus during postnatal development. Neuroscience 56:129–137.

Christie M, Williams J, North R (1989) Electrical coupling synchronizes subthreshold activity in locus coeruleus neurons in vitro from neonatal rats. J Neurosci 9:3584–3589.

Christie MJ (1997) Generators of synchronous activity of the locus coeruleus during development. Sem Cell Dev Biol 8:29–34.

Cornell-Bell AH, Finkbeiner SM, Cooper MS, Smith SJ (1990) Glutamate Induces Calcium Waves in Cultured Astrocytes: Long-Range Glial Signaling. Science 247:470–473.

Crunelli V, Lőrincz ML, Connelly WM, David F, Hughes SW, Lambert RC, Leresche N, Errington AC (2018) Dual function of thalamic low-vigilance state oscillations: rhythm-regulation and plasticity. Nat Rev Neurosci 19:107–118.

De Sarro G b., Ascioti C, Froio F, Libri V, Nisticò G (1987) Evidence that locus coeruleus is the site where clonidine and drugs acting at α_1- and α_2-adrenoceptors affect sleep and arousal mechanisms. Brit J Pharmacol 90:675–685.

Del Bigio MR (2010) Ependymal cells: biology and pathology. Acta Neuropathol 119:55–73.

Delaville C, De Deurwaerdère P, Benazzouz A (2011) Noradrenaline and Parkinson's Disease. Front Syst Neurosci 5:31.

Devor A, Yarom Y (2002) Electrotonic Coupling in the Inferior Olivary Nucleus Revealed by Simultaneous Double Patch Recordings. J Neurophysiol 87:3048–3058.

Didier M, Harandi M, Aguera M, Bancel B, Tardy M, Fages C, Calas A, Stagaard M, Milgard K, Belin MF (1986) Differential immunocytochemical staining for glial fibrillary acidic (GFA) protein, S-100 protein and glutamine synthetase in the rat subcommissural organ, nonspecialized ventricular ependyma and adjacent neuropil. Cell Tissue Res 245

Dieterich DC, Kreutz MR (2016) Proteomics of the Synapse – A Quantitative Approach to Neuronal Plasticity. Mol Cell Proteom 15:368–381.

Durkee CA, Covelo A, Lines J, Kofuji P, Aguilar J, Araque A (2019) $G_{i/o}$ protein-coupled receptors inhibit neurons but activate astrocytes and stimulate gliotransmission. Glia 67:1076–1093.

Einevoll GT, Kayser C, Logothetis NK, Panzeri S (2013) Modelling and analysis of local field potentials for studying the function of cortical circuits. Nat Rev Neurosci 14:770–785.

Ennis M, Behbehani M, Shipley MT, van Bockstaele EJ, Aston-Jones G (1991) Projections from the periaqueductal gray to the rostromedial pericoerulear region and nucleus locus coeruleus: Anatomic and physiologic studies. J Comp Neurol 306:480–494.

Eschenko O, Magri C, Panzeri S, Sara SJ (2012) Noradrenergic Neurons of the Locus Coeruleus Are Phase Locked to Cortical Up-Down States during Sleep. Cereb Cortex 22:426–435.

Feldman JL, Smith JC (1989) Cellular Mechanisms Underlying Modulation of Breathing Pattern in Mammalsa. Ann NY Acad Sci 563:114–130.

Fellin T, Carmignoto G (2004) Neurone-to-astrocyte signalling in the brain represents a distinct multifunctional unit. J Physiol 559:3–15.

Felten DL, Harrigan P, Burnett BT, Cummings JP (1981) Fourth ventricular tanycytes: A possible relationship with monoaminergic nuclei. Brain Res Bulletin 6:427–436.

Feng C-Y, Wiggins LM, von Bartheld CS (2011) The Locus Ceruleus Responds to Signaling Molecules Obtained from the CSF by Transfer through Tanycytes. J Neurosci 31:9147–9158.

Fernández-Pastor B, Meana JJ (2002) In vivo tonic modulation of the noradrenaline release in the rat cortex by locus coeruleus somatodendritic α_2-adrenoceptors. Eur J Pharmacol 442:225–229.

Fiacco TA, McCarthy KD (2006) Astrocyte calcium elevations: Properties, propagation, and effects on brain signaling. Glia 54:676–690.

Fierro L, Llano I (1996) High endogenous calcium buffering in Purkinje cells from rat cerebellar slices. J Physiol 496:617–625.

Finkbeiner S (1992) Calcium waves in astrocytes-filling in the gaps. Neuron 8:1101–1108.

Foote SL, Bloom FE, Aston-Jones G (1983) Nucleus locus ceruleus: new evidence of anatomical and physiological specificity. Physiol Rev 63:844–914.

Funk GD, Smith JC, Feldman JL (1993) Generation and transmission of respiratory oscillations in medullary slices: role of excitatory amino acids. J Neurophysiol 70:1497–1515.

Gaidin SG, Zinchenko VP, Sergeev AI, Teplov IY, Mal'tseva VN, Kosenkov AM (2020) Activation of alpha-2 adrenergic receptors stimulates GABA release by astrocytes. Glia 68:1114–1130.

Garaschuk O, Linn J, Eilers J, Konnerth A (2000) Large-scale oscillatory calcium waves in the immature cortex. Nat Neurosci 3:452–459.

Gasparini S, Resch JM, Gore AM, Peltekian L, Geerling JC (2021) Pre-locus coeruleus neurons in rat and mouse. Amer J of Physiol-Reg, Int Comp Physiol 320:R342–R361.

Göbel W, Helmchen F (2007) In Vivo Calcium Imaging of Neural Network Function. Physiology 22:358–365.

Gonzalez OJA, Aerde KI van, Elburg RAJ van, Poil S-S, Mansvelder HD, Linkenkaer-Hansen K, Pelt J van, Ooyen A van (2012) External Drive to Inhibitory Cells Induces Alternating Episodes of High- and Low-Amplitude Oscillations. PLOS Comp. Biol. 8:e1002666.

Greger IH, Watson JF, Cull-Candy SG (2017) Structural and Functional Architecture of AMPA-Type Glutamate Receptors and Their Auxiliary Proteins. Neuron 94:713–730.

Grosche J, Kettenmann H, Reichenbach A (2002) Bergmann glial cells form distinct morphological structures to interact with cerebellar neurons. J Neurosci Res.68:138–149.

Gulledge AT, Kampa BM, Stuart GJ (2005) Synaptic integration in dendritic trees. J Neurobiol 64:75–90.

Guthrie PB, Knappenberger J, Segal M, Bennett MVL, Charles AC, Kater SB (1999) ATP Released from Astrocytes Mediates Glial Calcium Waves. J Neurosci 19:520–528.

Haas B, Schipke CG, Peters O, Söhl G, Willecke K, Kettenmann H (2006) Activity-dependent ATP-waves in the Mouse Neocortex are Independent from Astrocytic Calcium Waves. Cereb Cortex 16:237–246.

Halassa MM, Fellin T, Takano H, Dong J-H, Haydon PG (2007) Synaptic Islands Defined by the Territory of a Single Astrocyte. J Neurosci 27:6473–6477.

Halassa MM, Haydon PG (2010) Integrated Brain Circuits: Astrocytic Networks Modulate Neuronal Activity and Behavior. Ann Rev Physiol 72:335–355.

Hassinger TD, Guthrie PB, Atkinson PB, Bennett MVL, Kater SB (1996) An extracellular signaling component in propagation of astrocytic calcium waves. PNAS 93:13268–13273.

Hille B (1984) Ionic Channels of Excitable Membranes, 3rd ed. Sinauer Associates.

Hirase H, Qian L, Barthó P, Buzsáki G (2004) Calcium Dynamics of Cortical Astrocytic Networks In Vivo. PLOS Biol 2:e96.

Holets VR, Hökfelt T, Rökaeus Å, Terenius L, Goldstein M (1988) Locus coeruleus neurons in the rat containing neuropeptide Y, tyrosine hydroxylase or galanin and their efferent projections to the spinal cord, cerebral cortex and hypothalamus. Neuroscience 24:893–906.

Hu H, Vervaeke K, Storm JF (2007) M-Channels (Kv7/KCNQ Channels) That Regulate Synaptic Integration, Excitability, and Spike Pattern of CA1 Pyramidal Cells Are Located in the Perisomatic Region. J Neurosci 27:1853–1867.

Imber AN, Putnam RW (2012) Postnatal development and activation of L-type Ca^{2+} currents in locus ceruleus neurons: implications for a role for Ca^{2+} in central chemosensitivity. J of Applied Physiol 112:1715–1726.

Ishimatsu M, Williams JT (1996) Synchronous Activity in Locus Coeruleus Results from Dendritic Interactions in Pericoerulear Regions. J Neurosci 16:5196–5204.

Ivanov A, Aston-Jones G (1995) Extranuclear dendrites of locus coeruleus neurons: activation by glutamate and modulation of activity by alpha adrenoceptors. J Neurophysiol 74:2427–2436.

Jackson AC, Nicoll RA (2011) Stargazin (TARP -2) Is Required for Compartment-Specific AMPA Receptor Trafficking and Synaptic Plasticity in Cerebellar Stellate Cells. J Neurosci 31:3939–3952.

Janczewski WA, Tashima A, Hsu P, Cui Y, Feldman JL (2013) Role of Inhibition in Respiratory Pattern Generation. J Neurosci 33:5454–5465.

Jefferys JG (1994) Experimental neurobiology of epilepsies. Curr Opin Neurol 7:113–122.

Jin X, Li S, Bondy B, Zhong W, Oginsky MF, Wu Y, Johnson CM, Zhang S, Cui N, Jiang C (2016) Identification of a Group of GABAergic Neurons in the Dorsomedial Area of the Locus Coeruleus Arenkiel B, ed. PLoS ONE 11:e0146470.

Kaeidi A, Azizi H, Javan M, Soleimani SMA, Fathollahi Y, Semnanian S (2015) Direct Facilitatory Role of Paragigantocellularis Neurons in Opiate Withdrawal-Induced

Hyperactivity of Rat Locus Coeruleus Neurons: An In Vitro Study. PLoS ONE 10:e0134873.

Kafitz KW, Meier SD, Stephan J, Rose CR (2008) Developmental profile and properties of sulforhodamine 101—Labeled glial cells in acute brain slices of rat hippocampus. J. Neurosci Meth 169:84–92.

Kanemaru K, Sekiya H, Xu M, Satoh K, Kitajima N, Yoshida K, Okubo Y, Sasaki T, Moritoh S, Hasuwa H, Mimura M, Horikawa K, Matsui K, Nagai T, Iino M, Tanaka KF (2014) In Vivo Visualization of Subtle, Transient, and Local Activity of Astrocytes Using an Ultrasensitive Ca^{2+} Indicator. Cell Rep 8:311–318.

Kantor C (2012) Modulation of Spontaneous Neural Network Bursting in Newborn Rat Brain Slices by Extracellular Calcium, Methylxanthines and Opioids.

Kantor C, Panaitescu B, Kuribayashi J, Ruangkittisakul A, Jovanovic I, Leung V, Lee T-F, MacTavish D, Jhamandas JH, Cheung P-Y, Ballanyi K (2012) Spontaneous Neural Network Oscillations in Hippocampus, Cortex, and Locus Coeruleus of Newborn Rat and Piglet Brain Slices. In: Isolated Central Nervous System Circuits (Ballanyi K, ed), pp 315–356 Neuromethods. Totowa, NJ: Humana Press.

Kerekes BP, Tóth K, Kaszás A, Chiovini B, Szadai Z, Szalay G, Pálfi D, Bagó A, Spitzer K, Rózsa B, Ulbert I, Wittner L (2014) Combined two-photon imaging, electrophysiological, and anatomical investigation of the human neocortex in vitro. Neurophotonics 1:011013.

Kim WT, Rioult MG, Cornell-Bell AH (1994) Glutamate-induced calcium signaling in astrocytes. Glia 11:173–184.

Kimura F, Nakamura S (1985) Locus coeruleus neurons in the neonatal rat: Electrical activity and responses to sensory stimulation. Dev Brain Res 23:301–305.

Kuga N, Sasaki T, Takahara Y, Matsuki N, Ikegaya Y (2011) Large-Scale Calcium Waves Traveling through Astrocytic Networks In Vivo. J Neurosci 31:2607–2614.

Kuo C, Hsieh J, Tsai H, Kuo Y, Yau H, Chen C, Chen R, Yang H, Min M (2020) Inhibitory interneurons regulate phasic activity of noradrenergic neurons in the mouse locus coeruleus and functional implications. J Physiol 598:4003–4029.

Latorre R, Aguirre C, Rabinovich M, Varona P (2013) Transient dynamics and rhythm coordination of inferior olive spatio-temporal patterns. Front Neural Circ 7

Lavezzi AM, Ottaviani G, Mingrone R, Matturri L (2005) Analysis of the human locus coeruleus in perinatal and infant sudden unexplained deaths. Possible role of the cigarette smoking in the development of this nucleus. Developmental Brain Research 154:71–80.

Lauder JM, Bloom FE (1974) Ontogeny of monoamine neurons in the locus coeruleus, raphe nuclei and substantia nigra of the rat. I. Cell differentiation. J Comp Neurol 155:469–481.

Li Y, Hickey L, Perrins R, Werlen E, Patel AA, Hirschberg S, Jones MW, Salinas S, Kremer EJ, Pickering AE (2016) Retrograde optogenetic characterization of the pontospinal module of the locus coeruleus with a canine adenoviral vector. Brain Res 1641:274–290.

Lieske SP, Thoby-Brisson M, Telgkamp P, Ramirez JM (2000) Reconfiguration of the neural network controlling multiple breathing patterns: eupnea, sighs and gasps. Nat Neurosci 3:600–607.

Lopez-Hidalgo M, Hoover W, Schummers J (2016) Spatial organization of astrocytes in ferret visual cortex. J Compar Neurol 524.

Loughlin SE, Foote SL, Bloom FE (1986) Efferent projections of nucleus locus coeruleus: Topographic organization of cells of origin demonstrated by three-dimensional reconstruction. Neuroscience 18:291–306.

Lüthi A (2014) Sleep Spindles: Where They Come From, What They Do. Neuroscientist 20:243–256.

Maeda T, Kojima Y, Arai R, Fujimiya M, Kimura H, Kitahama K, Geffard M (1991) Monoaminergic interaction in the central nervous system: A morphological analysis in the locus coeruleus of the rat. Comparative Biochemistry and Physiology Part C: Comparative Pharmacology 98:193–202.

Magalhães KS, Spiller PF, da Silva MP, Kuntze LB, Paton JFR, Machado BH, Moraes DJA (2018) Locus Coeruleus as a vigilance centre for active inspiration and expiration in rats. Sci Rep 8:15654.

Maher MP, Matta JA, Gu S, Seierstad M, Bredt DS (2017) Getting a Handle on Neuropharmacology by Targeting Receptor-Associated Proteins. Neuron 96:989–1001.

Marshall KC, Christie MJ, Finlayson PG, Williams JT (1991) Developmental aspects of the locus coeruleus-noradrenaline system. In: Progress in Brain Research, pp 173–185. Elsevier.

Marwaha J, Aghajanian GK (1982) Relative potencies of alpha-1 and alpha-2 antagonists in the locus ceruleus, dorsal raphe and dorsal lateral geniculate nuclei: an electrophysiological study. J Pharmacol Exp Ther 222:287–293.

Matschke LA, Bertoune M, Roeper J, Snutch TP, Oertel WH, Rinné S, Decher N (2015) A concerted action of L- and T-type Ca^{2+} channels regulates locus coeruleus pacemaking. Mol Cell Neurosci 68:293–302.

Matschke LA, Rinné S, Snutch TP, Oertel WH, Dolga AM, Decher N (2018) Calcium-activated SK potassium channels are key modulators of the pacemaker frequency in locus coeruleus neurons. Mol Cell Neurosci 88:330–341.

McCall JG, Al-Hasani R, Siuda ER, Hong DY, Norris AJ, Ford CP, Bruchas MR (2015) CRH Engagement of the Locus Coeruleus Noradrenergic System Mediates Stress-Induced Anxiety. Neuron 87:605–620.

Melnychuk MC, Robertson IH, Plini ERG, Dockree PM (2021) A Bridge between the Breath and the Brain: Synchronization of Respiration, a Pupillometric Marker of the Locus Coeruleus, and an EEG Marker of Attentional Control State. Brain Sci 11:1324.

Metzger F, Kulik A, Sendtner M, Ballanyi K (2000) Contribution of Ca^{2+} -Permeable AMPA/KA Receptors to Glutamate-Induced Ca^{2+} Rise in Embryonic Lumbar Motoneurons In Situ. J Neurophysiol 83:50–59.

Mosienko V, Rasooli-Nejad S, Kishi K, De Both M, Jane D, Huentelman M, Kasparov S, Teschemacher A (2018) Putative Receptors Underpinning l-Lactate Signalling in Locus Coeruleus. Neuroglia 1:365–380.

Mrejeru A, Wei A, Ramirez JM (2011) Calcium-activated non-selective cation currents are involved in generation of tonic and bursting activity in dopamine neurons of the substantia nigra pars compacta. J Physiol 589:2497–2514.

Nakamura S, Kimura F, Sakaguchi T (1987) Postnatal development of electrical activity in the locus ceruleus. J Neurophysiol 58:510–524.

Nakamura S, Sakaguchi T (1990) Development and plasticity of the locus coeruleus: A review of recent physiological and pharmacological experimentation. Prog Neurobiol 34:505–526.

Nakamura S, Sakaguchi T, Kimura F, Aoki F (1988) The role of alpha 1-adrenoceptor-mediated collateral excitation in the regulation of the electrical activity of locus coeruleus neurons. Neuroscience 27:921–929.

Nakamura T, Nakamura K, Lasser-Ross N, Barbara J-G, Sandler VM, Ross WN (2000) Inositol 1,4,5-Trisphosphate (IP_3)-Mediated Ca^{2+} Release Evoked by Metabotropic Agonists and Backpropagating Action Potentials in Hippocampal CA1 Pyramidal Neurons. J Neurosci 20:8365–8376.

Nedergaard M (1994) Direct Signaling from Astrocytes to Neurons in Cultures of Mammalian Brain Cells. Science 263:1768–1771.

Nestler EJ, McMahon A, Sabban EL, Tallman JF, Duman RS (1990) Chronic antidepressant administration decreases the expression of tyrosine hydroxylase in the rat locus coeruleus. PNAS USA 87:7522–7526.

Neuman RS, Cherubini E, Ben-Ari Y (1989) Endogenous and network bursts induced by N-methyl-d-aspartate and magnesium free medium in the CA3 region of the hippocampal slice. Neuroscience 28:393–399.

Newman EA (2001) Propagation of Intercellular Calcium Waves in Retinal Astrocytes and Müller Cells. J Neurosci 21:2215–2223.

Newman EA, Zahs KR (1997) Calcium Waves in Retinal Glial Cells. Science 275:844–847.

Nicholas AP, Hökfely T, Pieribone VA (1996) The distribution and significance of CNS adrenoceptors examined with in situ hybridization. Trends Pharmacol Sci 17:245–255.

Nimmerjahn A, Kirchhoff F, Kerr JND, Helmchen F (2004) Sulforhodamine 101 as a specific marker of astroglia in the neocortex in vivo. Nat Methods 1:31–37.

Niswender CM, Conn PJ (2010) Metabotropic Glutamate Receptors: Physiology, Pharmacology, and Disease. Annu Rev Pharmacol Toxicol 50:295–322.

North RA, Williams JT (1985) On the potassium conductance increased by opioids in rat locus coeruleus neurones. J Physiol 364:265–280.

Oberheim NA, Tian G-F, Han X, Peng W, Takano T, Ransom B, Nedergaard M (2008) Loss of Astrocytic Domain Organization in the Epileptic Brain. J Neurosci 28:3264–3276.

Oberheim NA, Wang X, Goldman S, Nedergaard M (2006) Astrocytic complexity distinguishes the human brain. Trends Neurosci 29:547–553.

Ogata K, Kosaka T (2002) Structural and quantitative analysis of astrocytes in the mouse hippocampus. Neuroscience 113:221–233.

Olpe H-R, Steinmann MartinW, Brugger F, Pozza MarioF (1989) Excitatory amino acid receptors in rat locus coeruleus: An extracellular in vitro study. Naunyn-Schmiedeberg's Arch Pharmacol 339

Olpe H-R, Steinmann MW, Hall RG, Brugger F, Pozza MF (1988) GABAA and GABAB receptors in locus coeruleus: effects of blockers. Eur J Pharmacol 149:183–185.

Olson L, Seiger Å (1972) Early prenatal ontogeny of central monoamine neurons in the rat: Fluorescence histochemical observations. Z Anat Entwickl Gesch 137:301–316.

Oyamada Y, Ballantyne D, Mückenhoff K, Scheid P (1998) Respiration-modulated membrane potential and chemosensitivity of locus coeruleus neurones in the in vitro brainstem-spinal cord of the neonatal rat. J Physiol 513:381–398.

Panaitescu B (2012) Antagonistic modulation of spontaneous neural network activites in isolated newborn rat brainstem preparations by opioids and methylxanthines.

Panaitescu B, Ballanyi K (2022) Methylxanthine acceleration and countering of opioid depression of synchronous locus coeruleus network oscillations in newborn rat brain slices. *in preparation*

Parpura V, Basarsky TA, Liu F, Jeftinija K, Jeftinija S, Haydon PG (1994) Glutamate-mediated astrocyte–neuron signalling. Nature 369:744–747.

Patel M, Joshi B (2015) Modeling the evolving oscillatory dynamics of the rat locus coeruleus through early infancy. Brain Res 1618:181–193.

Perea G, Araque A (2005) Properties of Synaptically Evoked Astrocyte Calcium Signal Reveal Synaptic Information Processing by Astrocytes. J Neurosci 25:2192–2203.

Pires J, Nelissen R, Mansvelder HD, Meredith RM (2021) Spontaneous synchronous network activity in the neonatal development of mPFC in mice. Dev Neurobiol 81:207–225.

Pitts DK, Marwah J (1986) Effects of cocaine on the electrical activity of single noradrenergic neurons from locus coeruleus. Life Sci 38:1229–1234.

Pixley SKR, de Vellis J (1984) Transition between immature radial glia and mature astrocytes studied with a monoclonal antibody to vimentin. Dev Brain Res 15:201–209.

Poe GR, Foote S, Eschenko O, Johansen JP, Bouret S, Aston-Jones G, Harley CW, Manahan-Vaughan D, Weinshenker D, Valentino R, Berridge C, Chandler DJ, Waterhouse B, Sara SJ (2020) Locus coeruleus: a new look at the blue spot. Nat Rev Neurosci 21:644–659.

Poil S-S, Jansen R, van Aerde K, Timmerman J, Brussaard AB, Mansvelder HD, Linkenkaer-Hansen K (2011) Fast network oscillations in vitro exhibit a slow decay of temporal auto-correlations. Eur J Neurosci 34:394–403.

Posłuszny A (2014) The contribution of electrical synapses to field potential oscillations in the hippocampal formation. Front Neural Circ 8

Rajani V, Zhang Y, Jalubula V, Rancic V, SheikhBahaei S, Zwicker JD, Pagliardini S, Dickson CT, Ballanyi K, Kasparov S, Gourine AV, Funk GD (2018) Release of ATP by pre-Bötzinger complex astrocytes contributes to the hypoxic ventilatory response via a Ca^{2+}-dependent P2Y1 receptor mechanism. J Physiol 596:3245–3269.

Rancic V, Gosgnach S (2021) Recent Insights into the Rhythmogenic Core of the Locomotor CPG. Int J Mol Sci 22:1394.

Rancic V, Rawal B, Panaitescu B, Ruangkittisakul A, Ballanyi K (2018) Suction electrode recording in locus coeruleus of newborn rat brain slices reveals network bursting comprising summated non-synchronous spiking. Neurosci Lett 671:103–107.

Rash JE, Olson CO, Davidson KGV, Yasumura T, Kamasawa N, Nagy JI (2007) Identification of connexin36 in gap junctions between neurons in rodent locus coeruleus. Neuroscience 147:938–956.

Rawal B (2019) The neonatal locus coeruleus is a differentiated and complex neurodmodulatory system as revealed by local field potential analysis.

Rawal B, Ballanyi K (2022) AMPA receptor-evoked transformation of locus coeruleus network bursting in newborn rat slices into faster and more regular spindle-shaped oscillations. *in preparation*

Rawal B, Rancic V, Ballanyi K (2019) TARP mediation of accelerated and more regular locus coeruleus network bursting in neonatal rat brain slices. Neuropharmacol. 148:169–177.

Rawal B, Rancic V, Ballanyi K (2022) NMDA Enhances and Glutamate Attenuates Synchrony of Spontaneous Phase-Locked Locus Coeruleus Network Rhythm in Newborn Rat Brain Slices. Brain Sci 12:651.

Ruangkittisakul A, Ballanyi K (2010) Methylxanthine reversal of opioid-evoked inspiratory depression via phosphodiesterase-4 blockade. Resp Physiol Neurobiol 172:94–105.

Ruangkittisakul A, Okada Y, Oku Y, Koshiya N, Ballanyi K (2009) Fluorescence imaging of active respiratory networks. Resp Physiol Neurobiol168:26–38.

Ruangkittisakul A, Sharopov S, Kantor C, Kuribayashi J, Mildenberger E, Luhmann HJ, Kilb W, Ballanyi K (2015) Methylxanthine-evoked perturbation of spontaneous and evoked activities in isolated newborn rat hippocampal networks. Neuroscience 301:106–120.

Sabatini BL, Svoboda K (2000) Analysis of calcium channels in single spines using optical fluctuation analysis. Nature 408:589–593.

Sakaguchi T, Nakamura S (1987) Some in vivo electrophysiological properties of locus coeruleus neurones in fetal rats. Exp Brain Res 68

Sanchez-Padilla J, Guzman JN, Ilijic E, Kondapalli J, Galtieri DJ, Yang B, Schieber S, Oertel W, Wokosin D, Schumacker PT, Surmeier DJ (2014) Mitochondrial oxidant stress in locus coeruleus is regulated by activity and nitric oxide synthase. Nat Neurosci 17:832–840.

Sapkota D, Kater MSJ, Sakers K, Nygaard KR, Liu Y, Lake AM, Khazanchi R, Khankan RR, Smit AB, Maloney SE, Verheijen MHG, Zhang Y, Dougherty JD (2020) Activity dependent translation in astrocytes dynamically alters the proteome of the perisynaptic astrocyte process. Neuroscience.

Scemes E, Giaume C (2006) Astrocyte calcium waves: What they are and what they do. Glia 54:716–725.

Schwarz LA, Luo L (2015) Organization of the Locus Coeruleus-Norepinephrine System. Curr Biol 25:R1051–R1056.

Schwarz LA, Miyamichi K, Gao XJ, Beier KT, Weissbourd B, DeLoach KE, Ren J, Ibanes S, Malenka RC, Kremer EJ, Luo L (2015) Viral-genetic tracing of the input–output organization of a central noradrenaline circuit. Nature 524:88–92.

Scott LL, Mathews PJ, Golding NL (2010) Perisomatic Voltage-Gated Sodium Channels Actively Maintain Linear Synaptic Integration in Principal Neurons of the Medial Superior Olive. J Neurosci 30:2039–2050.

Segal DS, Kuczenski R (1974) Tyrosine hydroxylase activity: Regional and subcellular distribution in brain. Brain Res 68:261–266.

Shao XM, Feldman JL (1997) Respiratory Rhythm Generation and Synaptic Inhibition of Expiratory Neurons in Pre-Bötzinger Complex: Differential Roles of Glycinergic and GABAergic Neural Transmission. J Neurophysiol 77:1853–1860.

Sharifullina E, Ostroumov K, Grandolfo M, Nistri A (2008) N-methyl-d-aspartate triggers neonatal rat hypoglossal motoneurons in vitro to express rhythmic bursting with unusual Mg^{2+} sensitivity. Neuroscience 154:804–820.

SheikhBahaei S, Morris B, Collina J, Anjum S, Znati S, Gamarra J, Zhang R, Gourine AV, Smith JC (2018) Morphometric analysis of astrocytes in brainstem respiratory regions. J Compar Neurol 526:2032–2047.

Shimizu N, Imamoto K (1970) Fine Structure of the Locus Coeruleus in the Rat. Archivum histologicum japonicum 31:229–246.

Shin J-W, Geerling JC, Stein MK, Miller RL, Loewy AD (2011) FoxP2 brainstem neurons project to sodium appetite regulatory sites. J Chem Neuroanat 42:1–23.

Singewald N, Philippu A (1998) Release of neurotransmitters in the locus coeruleus. Prog Neurobiol 56:237–267.

Sipilä ST, Kaila K (2008) GABAergic Control of CA3-driven Network Events in the Developing Hippocampus. In: Inhibitory Regulation of Excitatory Neurotransmission (Darlison MG, ed), pp 99–121. Berlin, Heidelberg: Springer Berlin Heidelberg.

Srinivasan R, Huang BS, Venugopal S, Johnston AD, Chai H, Zeng H, Golshani P, Khakh BS (2015) Ca^{2+} signaling in astrocytes from Ip3r2−/− mice in brain slices and during startle responses in vivo. Nat Neurosci 18:708–717.

Steiner J, Bernstein H-G, Bielau H, Berndt A, Brisch R, Mawrin C, Keilhoff G, Bogerts B (2007) Evidence for a wide extra-astrocytic distribution of S100B in human brain. BMC Neurosci 8:2.

Stosiek C, Garaschuk O, Holthoff K, Konnerth A (2003) In vivo two-photon calcium imaging of neuronal networks. PNAS 100:7319–7324.

Sucher NJ, Deitcher DL (1995) PCR and patch-clamp analysis of single neurons. Neuron 14:1095–1100.

Sullivan D, Mizuseki K, Sorgi A, Buzsaki G (2014) Comparison of Sleep Spindles and Theta Oscillations in the Hippocampus. J Neurosci 34:662–674.

Sun W, McConnell E, Pare J-F, Xu Q, Chen M, Peng W, Lovatt D, Han X, Smith Y, Nedergaard M (2013) Glutamate-Dependent Neuroglial Calcium Signaling Differs Between Young and Adult Brain. Science 339:197–200.

Surprenant A, Williams JT (1987) Inhibitory synaptic potentials recorded from mammalian neurones prolonged by blockade of noradrenaline uptake. J Physiol 382:87–103.

Swanson LW (1976) The locus coeruleus: A cytoarchitectonic, golgi and immunohistochemical study in the albino rat. Brain Res 110:39–56.

Szabadi E (2013) Functional neuroanatomy of the central noradrenergic system. J Psychopharmacol 27:659–693.

Taccola G, Olivieri D, D'Angelo G, Blackburn P, Secchia L, Ballanyi K (2012) A1 adenosine receptor modulation of chemically and electrically evoked lumbar locomotor network activity in isolated newborn rat spinal cords. Neuroscience 222:191–204.

Taft JR, Vertes RP, Perry GW (2005) Distribution of GFAP+ Astrocytes in Adult and Neonatal Rat Brain. Int J Neurosci 115:1333–1343.

Takahashi A, Camacho P, Lechleiter JD, Herman B (1999) Measurement of Intracellular Calcium. Physiol Rev 79:1089–1125.

Tang F, Lane S, Korsak A, Paton JFR, Gourine AV, Kasparov S, Teschemacher AG (2014) Lactate-mediated glia-neuronal signalling in the mammalian brain. Nat Commun 5:3284.

Teschemacher AG, Kasparov S (2017) Chapter 8 - Dialogue Between Astrocytes and Noradrenergic Neurons Via l-Lactate. In: Noradrenergic Signaling and Astroglia (Vardjan N, Zorec R, eds), pp 167–182. Academic Press.

Totah NK, Logothetis NK, Eschenko O (2021) Synchronous spiking associated with prefrontal high γ oscillations evokes a 5-Hz rhythmic modulation of spiking in locus coeruleus. J Neurophysiol 125:1191–1201.

Totah NK, Neves RM, Panzeri S, Logothetis NK, Eschenko O (2018) The Locus Coeruleus Is a Complex and Differentiated Neuromodulatory System. Neuron 99:1055-1068.e6.

Totah NKB, Logothetis NK, Eschenko O (2019) Noradrenergic ensemble-based modulation of cognition over multiple timescales. Brain Res 1709:50–66.

Traynelis SF, Wollmuth LP, McBain CJ, Menniti FS, Vance KM, Ogden KK, Hansen KB, Yuan H, Myers SJ, Dingledine R (2010) Glutamate Receptor Ion Channels: Structure, Regulation, and Function Sibley D, ed. Pharmacol Rev 62:405–496.

Tsai H-H, Li H, Fuentealba LC, Molofsky AV, Taveira-Marques R, Zhuang H, Tenney A, Murnen AT, Fancy SPJ, Merkle F, Kessaris N, Alvarez-Buylla A, Richardson WD, Rowitch DH (2012) Regional Astrocyte Allocation Regulates CNS Synaptogenesis and Repair. Science 337:358–362.

Tsintsadze V, Minlebaev M, Suchkov D, Cunningham M, Khazipov R (2015) Ontogeny of Kainate-Induced Gamma Oscillations in the Rat CA3 Hippocampus in vitro. Front Cell Neurosci 9

Turecek J, Yuen GS, Han VZ, Zeng X-H, Bayer KU, Welsh JP (2014) NMDA Receptor Activation Strengthens Weak Electrical Coupling in Mammalian Brain. Neuron 81:1375–1388.

Uematsu A, Tan BZ, Ycu EA, Cuevas JS, Koivumaa J, Junyent F, Kremer EJ, Witten IB, Deisseroth K, Johansen JP (2017) Modular organization of the brainstem noradrenaline system coordinates opposing learning states. Nat Neurosci 20:1602–1611.

Van Bockstaele E j., Chan J, Pickel V m. (1996) Input from central nucleus of the amygdala efferents to pericoerulear dendrites, some of which contain tyrosine hydroxylase immunoreactivity. J Neurosci Res 45:289–302.

Van Bockstaele EJ, Garcia-Hernandez F, Fox K, Alvarez VA, Williams JT (2004) Expression of connexins during development and following manipulation of afferent input in the rat locus coeruleus. Neurochem Int 45:421–428.

van Drongelen W, Koch H, Elsen FP, Lee HC, Mrejeru A, Doren E, Marcuccilli CJ, Hereld M, Stevens RL, Ramirez J-M (2006) Role of Persistent Sodium Current in Bursting Activity of Mouse Neocortical Networks In Vitro. J Neurophysiol 96:2564–2577.

Verkhratsky A, Krishtal O (2009) Adenosine Triphosphate (ATP) as a Neurotransmitter. In: Encyclopedia of Neuroscience, pp 115–123. Elsevier.

Verkhratsky A, Parpura V (2014) Store-operated calcium entry in neuroglia. Neurosci Bulletin 30:125–133.

Vives V, Alonso G, Solal AC, Joubert D, Legraverend C (2003) Visualization of S100B-positive neurons and glia in the central nervous system of EGFP transgenic mice. J Comp Neurol 457:404–419.

Volterra A, Meldolesi J (2005) Astrocytes, from brain glue to communication elements: the revolution continues. Nat Rev Neurosci 6:626–640.

Wagner-Altendorf TA, Fischer B, Roeper J (2019) Axonal projection-specific differences in somatodendritic α2 autoreceptor function in locus coeruleus neurons. Eur J Neurosci 50:3772–3785.

Wahis J, Holt MG (2021) Astrocytes, Noradrenaline, α_1-Adrenoreceptors, and Neuromodulation: Evidence and Unanswered Questions. Front Cell Neurosci 15

Waselenchuk Q, Ballanyi K (2022) Autocrine Neuromodulation and Network Activity Patterns in the Locus Coeruleus of Newborn Rat Slices. Brain Sci 12:437.

Waselenchuk Q, Rawal B, Ballanyi K (2022) Activity-related changes of discharge patterns and cytosolic calcium in the locus coeruleus of newborn rat slices. *in preparation*

Williams JT, Bobker DH, Harris GC (1991) Chapter 11 - Synaptic potentials in locus coeruleus neurons in brain slices. In: Progress in Brain Research (Barnes CD, Pompeiano O, eds), pp 167–172 Neurobiology of the Locus Coeruleus. Elsevier.

Williams JT, Henderson G, North RA (1985) Characterization of α_2-adrenoceptors which increase potassium conductance in rat locus coeruleus neurones. Neuroscience 14:95–101.

Williams JT, Marshall KC (1987) Membrane properties and adrenergic responses in locus coeruleus neurons of young rats. J Neurosci 7:3687–3694.

Williams JT, North RA, Shefner SA, Nishi S, Egan TM (1984) Membrane properties of rat locus coeruleus neurones. Neuroscience 13:137–156.

Wu Y, Zhang A-Q, Yew DT (2005) Age related changes of various markers of astrocytes in senescence-accelerated mice hippocampus. Neurochem Int 46:565–574.

Yamaguchi H, Hopf FW, Li S-B, de Lecea L (2018) In vivo cell type-specific CRISPR knockdown of dopamine beta hydroxylase reduces locus coeruleus evoked wakefulness. Nat Commun 9:5211.

Yoshida T, Goldsmith SK, Morgan TE, Stone DJ, Finch CE (1996) Transcription supports age-related increases of GFAP gene expression in the male rat brain. Neurosci Lett 215:107–110.

Young WS, Kuhar MJ (1980) Noradrenergic alpha 1 and alpha 2 receptors: light microscopic autoradiographic localization. PNAS USA 77:1696–1700.

Yuste R, Konnerth A, Masters BR (2006) Imaging in Neuroscience and Development, A Laboratory Manual. J Biomed Optics 11:019902.

Zamalloa T, Bailey CP, Pineda J (2009) Glutamate-induced post-activation inhibition of locus coeruleus neurons is mediated by AMPA/kainate receptors and sodium-dependent potassium currents. Brit J Pharmacol 156:649–661.

Zamora NN, Cheli VT, Santiago González DA, Wan R, Paez PM (2020) Deletion of Voltage-Gated Calcium Channels in Astrocytes during Demyelination Reduces Brain Inflammation and Promotes Myelin Regeneration in Mice. J Neurosci 40:3332–3347.

Zhou Y, Danbolt NC (2014) Glutamate as a neurotransmitter in the healthy brain. J Neural Transm 121:799–817.

Zhu H, Zhou W (2005) Excitatory amino acid receptors are involved in morphine-induced synchronous oscillatory discharges in the locus coeruleus of rats. Eur J Pharmacol 528:73–78.

Zhu Z-T, Munhall A, Shen K-Z, Johnson SW (2004) Calcium-dependent subthreshold oscillations determine bursting activity induced by N-methyl-d-aspartate in rat subthalamic neurons in vitro. Eur J Neurosci 19:1296–1304.